

Air Force Institute of Technology

AFIT Scholar

Theses and Dissertations

Student Graduate Works

3-9-2009

Estimation of Weapon Yield from Inversion of Dose Rate Contours

Buckley E. O'Day III

Follow this and additional works at: <https://scholar.afit.edu/etd>



Part of the [Nuclear Commons](#)

Recommended Citation

O'Day, Buckley E. III, "Estimation of Weapon Yield from Inversion of Dose Rate Contours" (2009). *Theses and Dissertations*. 2454.

<https://scholar.afit.edu/etd/2454>

This Thesis is brought to you for free and open access by the Student Graduate Works at AFIT Scholar. It has been accepted for inclusion in Theses and Dissertations by an authorized administrator of AFIT Scholar. For more information, please contact richard.mansfield@afit.edu.



**ESTIMATION OF WEAPON YIELD FROM INVERSION OF DOSE RATE
CONTOURS**

THESIS

Buckley E. O'Day III, Major, USA

AFIT/GNE/ENP/09-M05

**DEPARTMENT OF THE AIR FORCE
AIR UNIVERSITY**

AIR FORCE INSTITUTE OF TECHNOLOGY

Wright-Patterson Air Force Base, Ohio

APPROVED FOR PUBLIC RELEASE; DISTRIBUTION UNLIMITED

The views expressed in this thesis are those of the author and do not reflect the official policy or position of the United States Air Force, Department of Defense, or the United States Government.

AFIT/GNE/ENP/09-M05

ESTIMATION OF WEAPON YIELD FROM INVERSION OF DOSE RATE
CONTOURS

THESIS

Presented to the Faculty

Department of Engineering Physics

Graduate School of Engineering and Management

Air Force Institute of Technology

Air University

Air Education and Training Command

In Partial Fulfillment of the Requirements for the
Degree of Master of Science (Nuclear Engineering)

Buckley E. O'Day III, BS, MIM

Major, USA

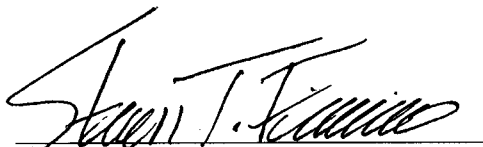
March 2009

APPROVED FOR PUBLIC RELEASE; DISTRIBUTION UNLIMITED

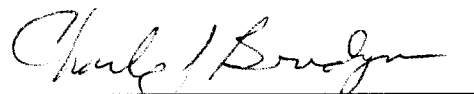
ESTIMATION OF WEAPON YIELD FROM INVERSION OF DOSE RATE
CONTOURS

Buckley E. O'Day III, BS, MIM
Major, USA

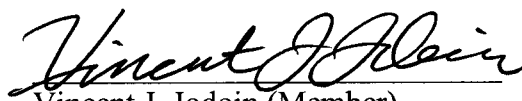
Approved:


Steven T. Fiorino (Chairman)

26 Feb 09
Date


Charles J. Bridgman (Member)

Feb 25, 2009
Date


Vincent J. Jodoin (Member)

Feb 25, 2009
Date

Abstract

This research examines the relationship between weapon yield and dose rate contours. Specifically, uncertainty in yield estimation from inversion of dose rate contours is studied. The Hazard Prediction and Assessment Capability (HPAC) and a simple FORTRAN95 based Fallout Deposition Code (FDC) are used to recreate dose rate contours from atomic tests. Recreated dose rate contours are compared to historical patterns found in the Defense Nuclear Agency's (DNA) DNA 1251-1-EX Compilation of Local Fallout Data From Test Detonations 1945-1962 Extracted from DASA 1251 using both a visual comparison and a spatial Figure of Merit (FOM) developed from the Measure of Effectiveness (MOE) and the Normalized Absolute Difference (NAD) techniques. The best-fit yield and yield estimates associated with 10%, 25%, and 50% error in FOM are determined. Results are used to determine uncertainty in yield estimation from inversion of dose rate contour plots. This research provides a method to estimate weapon yield to within a factor of 2 of the actual yield. This research also determined that the use of wind speed data from ground zero in combination with wind speeds from high resolution mesoscale reanalysis weather data allows the most accurate recreation of historic dose rate contours.

Acknowledgements

I would like to thank my advisor, LtCol Steven T. Fiorino, for his advice and encouragement. I would also like to thank Dr. Charles J. Bridgman and Dr. Vincent J. Jodoin for their expertise and assistance. I was fortunate to have been able to complete this work under the supervision of an atmospheric transport specialist and two of the premier nuclear fallout experts. I was even more fortunate in that all three members of my committee made the process associated with developing and effectively communicating this work a great learning experience. A special thank you goes to Capt Ty E. Miller. He served as someone whom I could discuss concepts and ideas with, as well as primary proof reader for my work.

I would like to thank my family for their love and support. I am deeply grateful to have a wife and children who selflessly endured a distracted, and sometimes grumpy, husband and father, for long enough to allow me to complete this thesis. I would like to thank my father for inspiring me to lifelong learning and reminding me of Occam's razor.

Table of Contents

	Page
Abstract.....	iv
<i>List of Figures</i>	ix
<i>List of Tables</i>	xii
I. Introduction	1
Background.....	2
Motivation.....	4
Scope.....	6
Problem Statement.....	6
II. Literature Review.....	7
Historical Context and Previous Research.....	7
Production of Radioactive Material	8
Cloud Rise.....	9
Cloud Stabilization Height.....	10
Characteristics of the Stabilized Cloud.....	13
Stabilized Cloud Top	15
Debris Entrainment and Fallout Particle Size	17
Fallout Particle Formation	17
Fallout Particle Size Distributions	18
Local and Delayed Fallout.....	21
Particle Fall Dynamics.....	22
Particle Transport.....	23
Concentration Dilution During Transport.....	24
Time Rate of Change of Activity.....	25
DNA-EX	27
Reanalysis Weather Data	29
Comparison of Observations and Predictions.....	31
Measure of Effectiveness.....	32
Normalized Absolute Difference	34
Figure of Merit.....	35
Yield Estimates and Error in FOM	37
MOE-NAD Isoline Graph.....	38
MOE-NAD Isoline Behavior for Low Yields.....	39
Capped and Uncapped Cloud Tops and Vertical Distribution of Activity	40
MOE-NAD Isoline Behavior for Capped and Uncapped Cloud Tops	41

	Page
III. Approach.....	43
Program Development	44
Program Selection.....	44
Fallout Deposition Code Concept Development	44
Fallout Deposition Code Assumptions	46
Fallout Deposition Code Structure.....	46
Code Highlights	47
Program Validation.....	52
Numerical Correctness and Precision	52
Qualitative Behavior	52
Modeling Test Cases.....	53
Optimization and Comments	57
Additional Codes	58
IV. Results and Analysis.....	59
Preliminary Results.....	59
Operation TUMBLER SNAPPER—George	65
Operation TEAPOT—ESS	70
Operation TEAPOT—Zucchini	76
Operation PLUMBBOB—Priscilla	80
Operation PLUMBBOB—Smoky	84
Operation SUNBEAM—Johnie Boy.....	88
Capped and Uncapped Yield Estimation Results	93
Validity of Weather Data	94
Sources of Error	96
V. Conclusions and Recommendations	98
Conclusions.....	98
Recommendations for Future Work.....	99
<i>Appendix A: FOM Comparison</i>	<i>101</i>
<i>Appendix B: Visual Comparisons of Historic Yields</i>	<i>102</i>
<i>Appendix C: Dose Rate Contour Changes As a Function of Yield.....</i>	<i>106</i>
<i>Appendix D: George FOM</i>	<i>111</i>

	Page
<i>Appendix E: ESS FOM</i>	112
<i>Appendix F: Zucchini FOM</i>	114
<i>Appendix G: Priscilla FOM</i>	115
<i>Appendix H: Smoky FOM</i>	116
<i>Appendix I: Johnie Boy FOM</i>	117
<i>Appendix J: HPAC Parameters</i>	118
<i>Appendix K: Statistical Analysis</i>	119
<i>Appendix L: Glossary</i>	120
Bibliography	122

List of Figures

Figure	Page
1. Toroidal Circulation Within A Radioactive Cloud.....	9
2. Group Center Stabilization Height Versus Particle Size	11
3. Conners' Particle Group Top and Bottom Versus Particle Size for 28kT Yield.....	12
4. Comparison of Hopkins' and Conners' Particle Group Stabilization Height Fits	13
5. Vertical Thickness of Particle Group Versus Particle Size	15
6. Top, Center, and Bottom Stabilization Heights Versus Particle Size Group.....	16
7. Nuclear Fireball Particle Dynamics	18
8. Way-Wigner Decay Law	26
9. DNA-EX Dose Rate Contour for George And Reanalysis Weather Grid	31
10. Areal Components for MOE Comparison	32
11. Key Characteristics of 2-D MOE Space	33
12. NAD Isolines in 2D MOE Space	35
13. Relationship of Dose Rate Contour Behavior and MOE-NAD Graph Placement	39
14. Activity Distribution of Initial Stabilized Cloud	41
15. Problem Solving Approach.....	43
16. Fallout Deposition Code Framework.....	47
17. 16-Point Spatial and Temporal Kriging.....	50
18. Test Case Dose Rate Contours.....	54
19. Normalized Vertical Distribution of Activity for 19.357 micron Particle Group.....	55
20. Dose Rate Contour for 19.357 micron Particle Group	56

Figure	Page
21. Effective Dispersion at Deposition for 19.357 micron Particle Group.....	56
22. Spatial Relationship of Dose Rate Contour Area, Weather Grid, and AOI.....	57
23. Zucchini FDC, DNA-EX, and HPAC Dose Rate Contours at 28KT	62
24. Zucchini 15, 22, 28, 40, and 60KT Yield HPAC Dose Rate Contours	63
25. Zucchini 15, 22, 28, 40, and 60KT Yield FDC Dose Rate Contours	64
26. George Digitized DNA-EX Contour Plot.....	65
27. George Terrain.....	66
28. George Error in FOM and Best-fit Yield Dose Rate Contours.....	67
29. George MOE-NAD Isolines	69
30. ESS Digitized DNA-EX Contour Plot.....	70
31. ESS Terrain.....	71
32. ESS MOE-NAD Isolines	72
33. ESS (No Cap) 5KT Yield Dose Rate Contours	74
34. ESS (No Cap) 7.5KT Yield Dose Rate Contours	74
35. ESS (No Cap) 10KT Yield Dose Rate Contours	75
36. Zucchini DNA-EX Contour Plot	76
37. Zucchini Terrain.....	77
38. Zucchini Error in FOM and Best-fit Yield Dose Rate Contours	78
39. Zucchini MOE-NAD Isolines	79
40. Priscilla DNA-EX Contour Plot.....	80
41. Priscilla Terrain.....	81
42. Priscilla Error in FOM and Best-fit Yield Dose Rate Contours	82

Figure	Page
43. Priscilla MOE-NAD Isolines	83
44. Smoky Digitized DNA-EX Contour Plot	84
45. Smoky Terrain	85
46. Smoky Error in FOM and Best-fit Yield Dose Rate Contours	86
47. Smoky MOE-NAD Isolines	87
48. Johnie Boy Digitized DNA-EX Contour Plot.....	88
49. Johnie Boy Terrain.....	89
50. Johnie Boy Error in FOM and Best-fit Yield Dose Rate Contours	90
51. Operation SUNBEAM—Johnie Boy MOE-NAD Isolines	92
52. Best-fit and Error in FOM MOE-NAD Isolines	95

List of Tables

Table	Page
1. DNA-EX Tests Studied.....	27
2. Ground Zero Wind Data Availability	28
3. High Resolution Mesoscale Reanalysis Weather Grids.....	30
4. DNA-EX and FDC Cloud Top Heights	60
5. HPAC and FDC Preliminary Results.....	61
6. Capped and Uncapped Cloud Height Yield Predictions.....	93

ESTIMATION OF WEAPON YIELD FROM INVERSION OF DOSE RATE
CONTOURS

I. Introduction

The purpose of this thesis is to determine the uncertainty associated with yield estimation from inversion of dose rate contours. The Hazard Prediction and Assessment Capability (HPAC) program and a simple Fallout Deposition Code (FDC) model employing 4-dimensional high resolution mesoscale reanalysis weather data are used to recreate dose rate contours from six selected atomic tests. HPAC and FDC contour plots for observed yields are compared visually and numerically against DNA-EX 1251-1-EX: Compilation of Local Fallout Data From Test Detonations 1945-1962 Extracted From DASA-1251 (DNA-EX) dose rate contours. The FDC more effectively recreated historic DNA-EX dose rate contours and is used for subsequent analysis. The FDC is used to create dose rate contours for a range of yields bracketing the actual weapon yield. Dose rate contours are inverted to estimate the best-fit weapon yield and yield estimates associated with 10%, 25%, and 50% allowable error in the FOM. The uncertainty in yield estimation from inversion of dose rate contours is studied. This thesis assumes readers have a basic understanding of nuclear weapon effects and meteorology.

Background

Since the terrorist attacks of September 11, 2001, the United States has been actively engaged in the War on Terror both abroad and at home. Our National Strategy for Combating Terrorism acknowledges “we are at war and that protecting and defending the Homeland, the American people, and their livelihoods remains our first and most solemn obligation” [1:1]. One critical step toward reaching this obligation, evident in our success in the War on Terror, has been our natural ability to analyze information and make decisions rapidly. There is no doubt that if a domestic nuclear event (DNE) occurred, the President of the United States’ first order would likely be to save as many lives as possible. His next order would be to find out who is responsible. To answer such a question would require knowledge of the weapon itself.

The scientific processes used to determine information about the weapon fall under the category of nuclear forensics. In the post-9/11 scientific community, the science of nuclear forensics has been pushed to the forefront. One of the major goals of this movement has been to develop ways of taking information readily available after a nuclear attack and using it to determine the composition and yield of the detonated weapon.

Given the possibility of a DNE, the United States Government has many active programs involving nuclear forensics. One of the key government agencies involved in the fight, the Defense Threat Reduction Agency (DTRA), has the mission of “safeguard[ing] America and its allies from Weapons of Mass Destruction by providing capabilities to reduce, eliminate, and counter the threat, and to mitigate its effects” [2]. DTRA provides training, seminars, reach-back capability, and computer-modeling tools

to allow Federal agencies and State and local governments to practice and improve their consequence management capabilities.

DTRA provides the HPAC suite of programs to serve as the primary “predictive software tool that allows the Warfighter and First Responder to generate decision-based information to facilitate enhanced situational awareness with the goal of protecting military and civilian populations from intentional or incidental Chemical, Biological, Radiological, and Nuclear (CBRN) threats” [3]. This suite of programs was designed to allow leaders to make more informed decisions in a timely manner.

As HPAC is frequently the consequence management planning tool of choice for governmental and selected civil agencies, significant efforts have been made to use this software suite as a predictive tool. Several researchers at AFIT have attempted to verify HPAC, and to improve its capabilities, in their research [4, 10, 11]. The most recent of these researchers, Jones, determined that HPAC fails to effectively reproduce nuclear test fallout patterns due to its neglect of lower-altitude wind effects on fallout [4].

Although HPAC has not effectively recreated historic dose rate contours to date, it still provides decision-makers with valuable information early in their decision cycle. For instance, HPAC provides a fair qualitative estimate of the size of an area that must be evacuated and insights into the number of displaced personnel. Although it may not allow decision-makers to quickly determine where to focus their consequence management resources in a single high risk area, it certainly allows them to gain insights into the types and quantities of assets that may be required.

DELFIIC is an effective tool to model phenomena seen in weapons tests [5]. Norment determined that the DELFIIC Cloud Rise Module (CRM) produced cloud top

and cloud bottom heights that generally agree with historical test data [6:1]. He noted that the CRM over-predicted cloud bases for very low yield detonations.

Since the development of a code like DELFIC was not reasonable within research time constraints, this research uses a modeling approach that capitalizes on DELFIC capabilities. Specifically, since past researchers such as Jodoin and Hopkins have demonstrated its effectiveness in modeling cloud rise, I have opted to create an initial stabilized cloud using empirical fits based on DELFIC data and to use a simple modified wafer tossing program to transport and deposit fallout from this cloud.

Motivation

Several students in the Air Force Institute of Technology's Nuclear Engineering program are currently considering various methods to determine weapon composition and/or yield. Current topics of research include measurement of isotopic ratios, nuclear thermal pulse-induced chemical changes in common structures (such as car paint), and yield-dependent time and spatial dose relationships. The end-goal of these endeavors is to develop a method to quickly estimate nuclear yield.

In the late 1970s, DELFIC was validated as a fallout modeling code using visual comparison, comparison of hotline lengths and azimuths, and the Rowland-Thompson Figure of Merit (FM) to compare five tests with yields from 0.5KT to 3.38 MT [7:60-71]. H+1 dose rate contours of 30 r/hr or higher were considered. In the validation process, DELFIC performed best for the low yield shots. The mean absolute percentage error for contour area was 61% for all contours, or 42% for all but the highest dose rate contour. For the lowest dose rate contour, the average dose rate contour area predicted was 75.7%

of that observed. The range of predicted to observed areas was from 47.4% to 163%. The predicted hotline lengths were closer to the observed values, and had a mean absolute percent error of only 26%. No statistics were computed for errors in azimuth direction of fallout but the low dose rate contours deviated by up to 53 degrees.

Although DELFIC was validated against these detonations for high dose rates, it was not validated against lower dose rates that would be present at a significant distance from ground zero. The areas used for comparison were only a small fraction of the DNA-EX dose rate contour areas. For instance, the smallest validated dose rate contour (50 r/hr) area for Johnie Boy (0.5KT) was 1.271 km². In contrast, the total DNA-EX contour area for the smallest recorded dose rate of 0.01 r/hr was 2,614 km².

No transport model in existence has reproduced historic nuclear test dose rate contours better than DELFIC. However, even DELFIC has not reproduced dose rate contours comparable to those found in the DNA-EX, and has not been validated for fallout prediction for lower dose rates. The inability of existing codes to reasonably match the DNA-EX contours calls into question the validity of using these codes to model fallout from a nuclear event.

For a fallout code to be useful in a yield-prediction capacity, it must be accurate, have short run times, and provide a reasonable estimate of yield. This research demonstrates that such a code can be developed. This research focuses on development of a simple model to estimate dose rate contours representing fallout deposition after a nuclear event. Since most experts propose a terrorist-built nuclear weapon upper-yield bound of approximately 15KT [8:2], this research will focus on yield estimation for events of less than 50KT. Given the difficulties associated with building a medium to

large yield weapon, any weapon with a yield of more than 25-30KT would likely have originated from a knowing or unknowing State sponsor. Such a determination would focus further nuclear forensics efforts to determine the weapon point of origin.

Scope

The intent of this research is two-fold. First, a FORTRAN program using simple approximations to first principles is developed to more accurately recreate the DNA-EX dose rate contours than those predicted by HPAC 4.04.11. Second, the feasibility of yield estimation from dose rate contour inversion is analyzed. The former objective aims to demonstrate that modest improvements to HPAC—such as effective integration of the DELFIC CRM—could greatly increase its capabilities as a modeling and/or predictive tool. The latter validates the concept of using inversion of dose rate contours to diagnose weapon yield.

Problem Statement

The primary goal of this research is to determine the error associated with estimation of weapon yield from inversion of dose rate contour plots. The enabling goal for this research is to produce fallout dose-rate contour maps that more accurately represent historical DNA-EX footprints than have been done to date.

II. Literature Review

This section provides background information critical to understanding both the historical importance and relevance of this research. A summary of recent research supporting this thesis is provided. A basic understanding of fallout and fallout deposition, a primer on fallout codes, and meteorological phenomena important to nuclear cloud transport and fallout deposition are addressed.

Historical Context and Previous Research

In the wake of 9/11, interest has piqued regarding the possibility of a domestic nuclear event and has resulted in a renewed emphasis on the need to accurately model fallout from nuclear explosions. In recent decades, computing power and atmospheric modeling capabilities have increased dramatically. As a result, complex models inclusive of more relevant physics have been developed to model atmospheric transport which could be used to model the transport and deposition of a radioactive cloud after a nuclear event.

Unfortunately, no complete data set exists to allow for easy validation and verification of modern modeling tools in a nuclear fallout modeling capacity. The type and amount of data gathered from tests varies. First, information on how, when, and where data used to construct DNA-EX dose rate contours was collected is limited. All of the US Government's 1,054 nuclear tests took place between 1945 and 1992 [9:vii-xi]. After July 1962, most nuclear tests within the US were underground, with the majority taking place at the Nevada Test Site. Some detonations from Operation PLOWSHARE,

which explored peaceful applications of nuclear explosions, were shallow-buried crater producing bursts. Second, the atmospheric data available for historic test dates is low resolution, consisting of soundings that may be taken hundreds of kilometers apart. Modern atmospheric soundings are generally taken more frequently and the total number of measurements available is much greater.

Previous researchers Chancellor [10], Pace [11], and Jones [4] used HPAC to study the same nuclear tests that are considered in this thesis. Chancellor digitized DNA-EX contours and did initial modeling with HPAC. Pace concluded that introduction of terrain resolution in a model that is greater than weather resolution introduces significant errors [11:82-83]. Jones identified that HPAC fails to properly integrate the DELFIC CRM into HPAC and therefore fails to consider the initial impact of surface and low altitudes winds [12:90]. The work of these researchers, as well as other work conducted at AFIT since the 1980s, provides the foundation on which this research is based.

Production of Radioactive Material

A nuclear detonation can create a significant amount of radioactive material. The deposition of this radioactive material, known as fallout, depends on the design and type of weapon, detonation location, and weather. These and other factors can significantly affect the amount of radioactive material produced. Fission weapons create approximately 55 grams of fission products per kiloton of weapon yield [13:401-402]. Fusion reactions do not directly create fission products. Both fission and fusion weapons create about 10^{23} neutrons that escape the device per kiloton of yield which can activate material resulting in increased radioactivity.

Cloud Rise

Since the fireball containing the radioactive material is much hotter than the surrounding atmosphere, it will rise until it reaches temperature equilibrium with the environment. During cloud rise, the fireball experiences drag from the surrounding air through which it is rising [14:28-29]. Irradiation and interaction with the air cools the outer portion of the fireball and the displacement of the fireball upward pulls cool air into the center of the fireball. This results in toroidal motion as seen in Figure 1 [14:29]. The amount of debris pulled up into the rising fireball largely depends on the weapon yield and proximity of detonation to the ground.

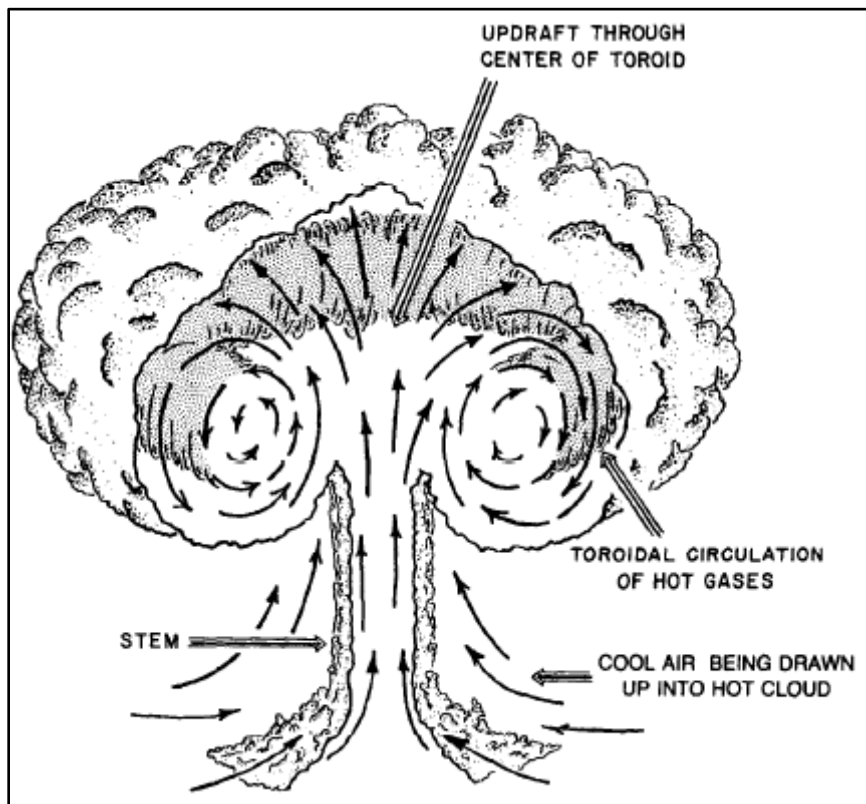


Figure 1. Toroidal Circulation Within A Radioactive Cloud From A Nuclear Explosion [14:29]

Jodoin combined vortex motion with DELFIC cloud rise to demonstrate effects on dose rate contour plots [5:113-114]. He determined that vortex behavior of the cloud allowed larger particles to remain aloft longer, and limited the amount of fallout deposition that occurred prior to cloud stabilization. Using this modification, he produced dose rate contours that were comparable to the DELFIC produced control, covering similar lateral area but having smoother, more realistic deposition of fallout. He also predicted stabilized cloud heights that more closely matched historic values.

Cloud Stabilization Height

As stated above, the cloud will continue to rise until a temperature equilibrium condition is reached between the cloud and the surrounding environment. Within the cloud, different size particles will rise to different altitudes. Upon stabilization, the particles in a group can be modeled as a normal distribution in the vertical centered at a group stabilization height, Z_c^g . Hopkins used DELFIC calculations for 30 tests of yields ranging from 1KT to 10MT to empirically determine particle stabilization heights, Z_c^g , as a function of particle radius (r_g) and yield (Y) as described in (1) [15:129].

$$Z_c^g = C_1 - C_2 r_g$$

$$\ln(C_1) = 7.889 + 0.34[\ln(Y)] + 0.001226[\ln(Y)]^2 - 0.004227[\ln(Y)]^3 + 0.000417[\ln(Y)]^4 \quad (1)$$

$$\ln(C_2) = 1.574 - 0.01197[\ln(Y)] + 0.03636[\ln(Y)]^2 - 0.0041[\ln(Y)]^3 + 0.0001965[\ln(Y)]^4$$

Figure 2 shows the particle group center stabilization heights for 15, 28, and 44KT yields using (1). Note that particle sizes larger than those shown for their respective yields have a particle group center stabilization height below ground level.

For these particle size groups, the fraction of the group's activity that is predicted below ground level is deposited at ground level.

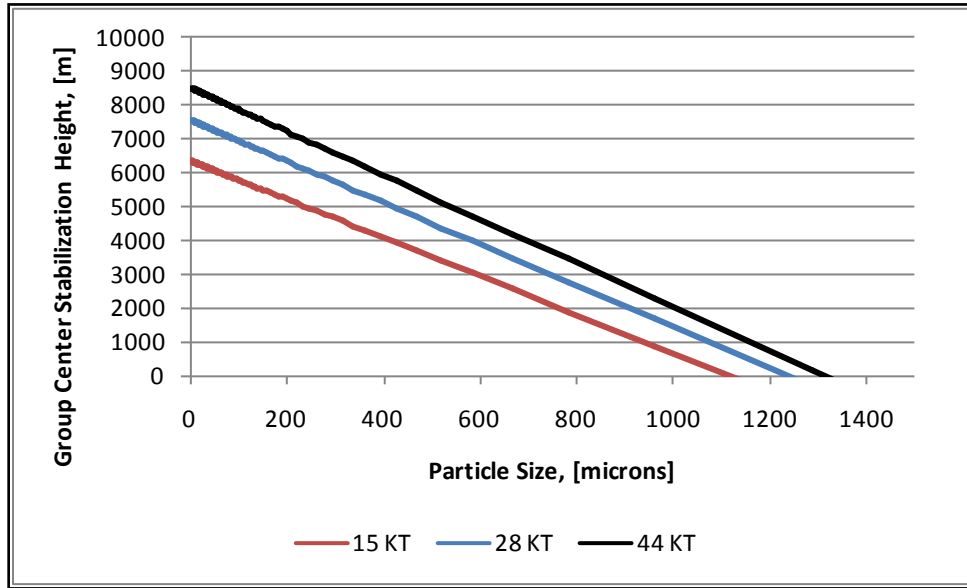


Figure 2. Group Center Stabilization Height Versus Particle Size for 15, 28, and 44KT Yields

Connors determined a yield-dependent fit for the vertical standard deviation of particle group height using a similar method [16:81-83]. He found numerical fits for the upper and lower elevations using DELFIC data, with S_T and I_T and S_B and I_B as the slope and intercept for equations describing the altitude of the top and bottom of the particle group within the visible cloud. From this, he determined a linear relationship describing the top and bottom of the particle group described by (2) and seen in Figure 3.

$$z = I + 2 \cdot (r_g) \cdot S$$

$$S_T = -e^{(1.61324 - 0.0682128 \ln(Y) + 0.0943986 \ln(Y)^2 - 0.0123826 \ln(Y)^3 + 0.000634405 \ln(Y)^4)}$$

$$I_T = e^{(8.10667 + 0.302301 \ln(Y) + 0.0191831 \ln(Y)^2 - 0.00748407 \ln(Y)^3 + 0.000518155 \ln(Y)^4)}$$

$$S_B = -e^{(1.77691 - 0.032544 \ln(Y) + 0.0679667 \ln(Y)^2 - 0.0114241 \ln(Y)^3 + 0.000590821 \ln(Y)^4)}$$

$$I_B = e^{(7.68304 + 0.372472 \ln(Y) - 0.0107429 \ln(Y)^2 - 0.0039146 \ln(Y)^3 + 0.000358551 \ln(Y)^4)}$$
(2)

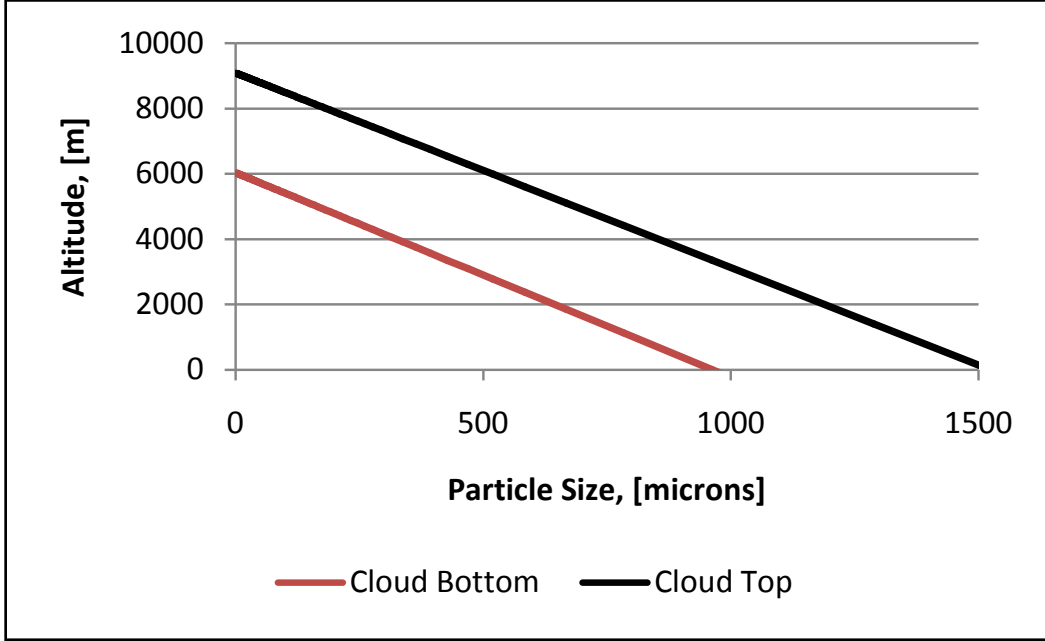


Figure 3. Conners' Particle Group Top and Bottom Versus Particle Size for 28kT Yield

From (2), the vertical thickness of a particle group, Δz_g , can be determined by (3) and the particle size group stabilization height is described by (4).

$$\Delta z_g = (I_T + 2 \cdot (r_g) \cdot S_T) - (I_B + 2 \cdot (r_g) \cdot S_B) \quad (3)$$

$$Z_{conners}^g = I_B + 2 \cdot (r_g) \cdot S_B + \frac{\Delta z_g}{2} \quad (4)$$

Figure 4 shows plot of Hopkins' (1) and Conners' (4) empirical fits for the particle size groups used in this study for a yield of 28KT. Note that Conners' equation provides lower particle group stabilization heights. Since Jodoin determined that vortex motion during cloud rise allowed larger particles to remain aloft longer, this model uses Hopkins' numerical fit to determine the initial stabilized cloud's particle group stabilization heights.

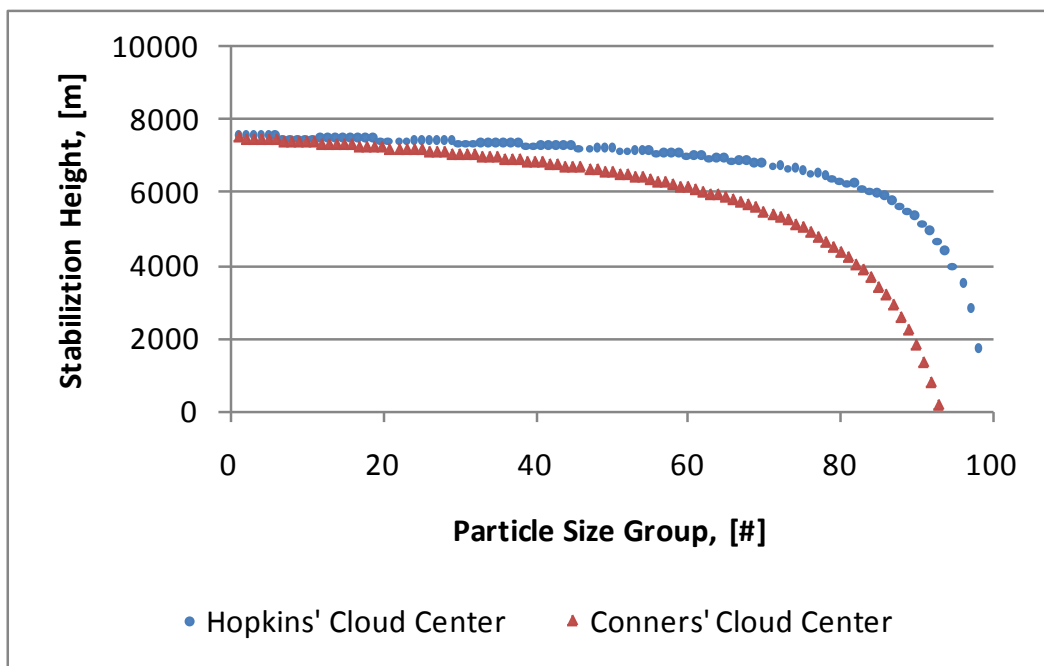


Figure 4. Comparison of Hopkins' and Conners' Particle Group Stabilization Height Numerical Fits

Characteristics of the Stabilized Cloud

As the cloud reaches its stabilization height, the particles in each equal activity particle size group will be roughly normally distributed. Bridgman denotes the

volumetric activity density of the stabilized cloud at stabilization time as (5), where σ_x , σ_y , and σ_z are the standard deviations in the three dimensions.

$$A(x, y, z, t_s) = A(t_s) \left\{ \frac{1}{\sqrt{2\pi}\sigma_x} e^{-\frac{1}{2}\left[\frac{x}{\sigma_x}\right]^2} \right\} \left\{ \frac{1}{\sqrt{2\pi}\sigma_y} e^{-\frac{1}{2}\left[\frac{y}{\sigma_y}\right]^2} \right\} \left\{ \frac{1}{\sqrt{2\pi}\sigma_z} e^{-\frac{1}{2}\left[\frac{z-z_c}{\sigma_z}\right]^2} \right\} \quad (5)$$

Pugh used a numerical fit to describe the standard deviation of the particle distribution of the cloud in the x and y directions as a function of yield, Y, in (6) [17:24].

$$\sigma_x = \sigma_y \equiv \sigma_o = 1.609e^{-\left[\frac{0.70 + \frac{1}{3}\ln\left(\frac{Y}{1000}\right) - \frac{3.25}{4.0 + \left(\ln\left(\frac{Y}{1000}\right) + 5.4\right)^2} \right]} \quad (6)$$

Pugh's assumption indicates the positive relationship between yield and horizontal spread of particles. Although Jodoin demonstrated that at the time of stabilization the activity of the cloud is distributed toroidally [5:91-93], Bridgman reports that analysis of grounded fallout patterns allow modeling of the horizontal distribution of activity as Gaussian [13:407].

The vertical spread of each particle group within the stabilized cloud depends on the particle size and yield. Connors developed an empirical fit from DELFIC data, (7), describing the distance from top to bottom for a particle group within the initialized visible radioactive cloud, where r_g is the particle group radius, s_d is the slope of the line, I_d is the line intercept, and Δz_c is the vertical thickness from top to bottom of the particle group [16:83].

$$\begin{aligned}
s_d &= 7 - e^{(1.78999 - 0.048249(\ln(Y)) + 0.0230248(\ln(Y))^2 - 0.00225965(\ln(Y))^3 + 0.000161519(\ln(Y))^4)} \\
I_d &= e^{(7.03518 + 0.158914(\ln(Y)) + 0.0837539(\ln(Y))^2 - 0.0155464(\ln(Y))^3 + 0.000862103(\ln(Y))^4)} \\
\Delta z_c &= I_d + 2r_g \cdot s_d
\end{aligned}
\tag{7}$$

Figure 5 shows the particle group vertical thickness versus particle size for a yield of 28KT.

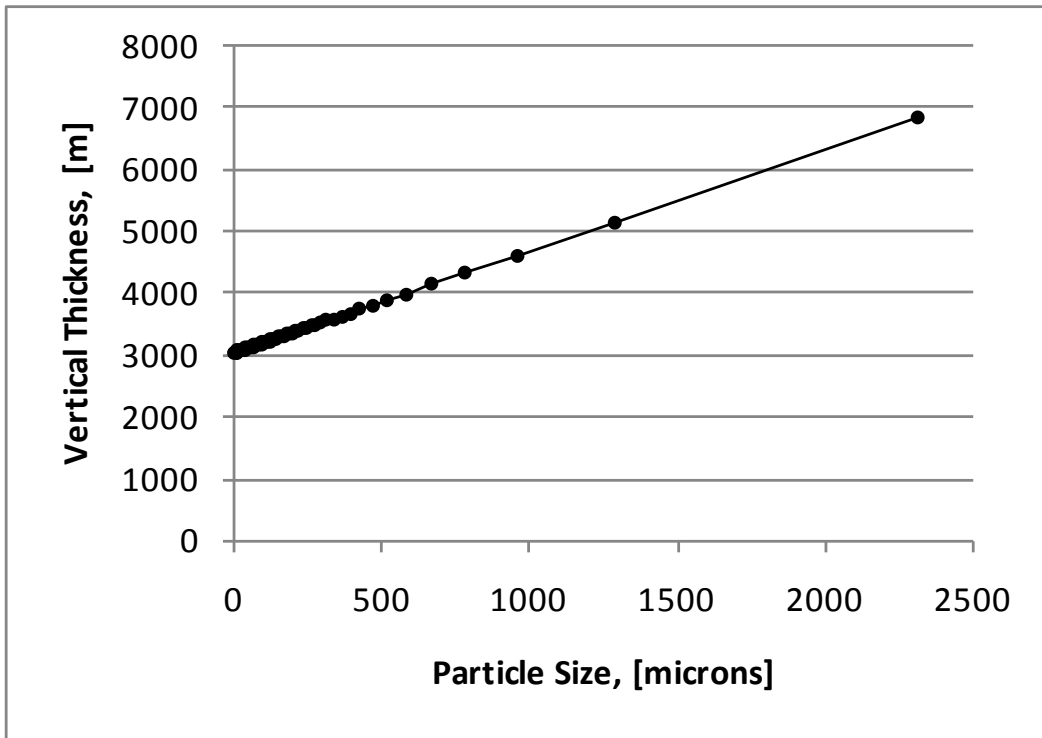


Figure 5. Vertical Thickness of Particle Group Versus Particle Size

Stabilized Cloud Top

From Hopkins' (1) and Conners' (7), the rise of the top of a particle size group, Z_{ct}^s , defined here as three standard deviations above Z_c^s , can be calculated for any

particle size group. It is important to note that the distribution of activity in a radioactive cloud is not confined to within the visible cloud. This research assumes that the vertical distribution of activity within any particle size group is Gaussian and that 68% of the group's activity will be located within one standard deviation of the particle group center. Conner's Δz_c is equal to two standard deviations (one above and one below the particle group center) and the standard deviation of a particle group in the z-direction is defined as $\sigma_z = \frac{\Delta z_c}{2}$. Therefore, the equation for the cloud top stabilization height, Z_{ct}^g , for a particle size group is (8).

$$Z_{ct}^g = Z_c^g + 3\sigma_z \quad (8)$$

Figure 6 shows the top, bottom, and center of the stabilized particle groups for a 28KT yield.

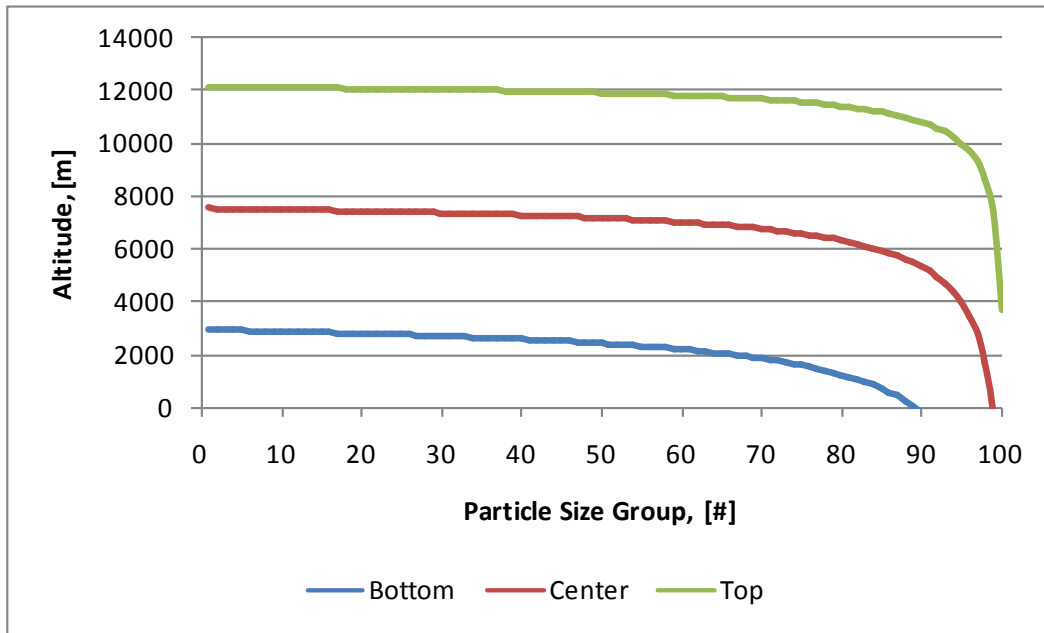


Figure 6. Top, Center, and Bottom Stabilization Heights Versus Particle Size Group

Debris Entrainment and Fallout Particle Size

The altitude at which a weapon is detonated significantly affects the extent of debris entrainment of the fireball and subsequent formation of fallout particles. In the event of an air burst, defined as a burst of sufficient height that no significant quantities of surface materials are pulled up into the fireball, the bulk of particles formed will be between 0.01 and 20 microns [14:409]. For ground or surface contact bursts, a significant amount of soil or other debris may be lifted into the air in a solid or vaporized form. The amount of soil lifted is yield dependent, with approximately 0.3 tons of dirt lifted per ton of yield [13:401-402]. The increased debris entrainment creates larger fallout particles, typically with diameters from a fraction of a micron to several millimeters [14:409].

Fallout Particle Formation

As the cloud rises and cools, the entrained material will begin to condense and will serve as a carrier for radioactive material. Bridgman describes the nuclear fireball particle dynamics as a process of refractory and subsequent volatile condensation with continued particle growth through agglomeration until cloud stabilization is reached as seen in Figure 7 [13:402-403]. He notes that the difference in condensation temperatures for refractories and volatiles leads to their volumetric and surface distributions, respectively, on fallout particles.

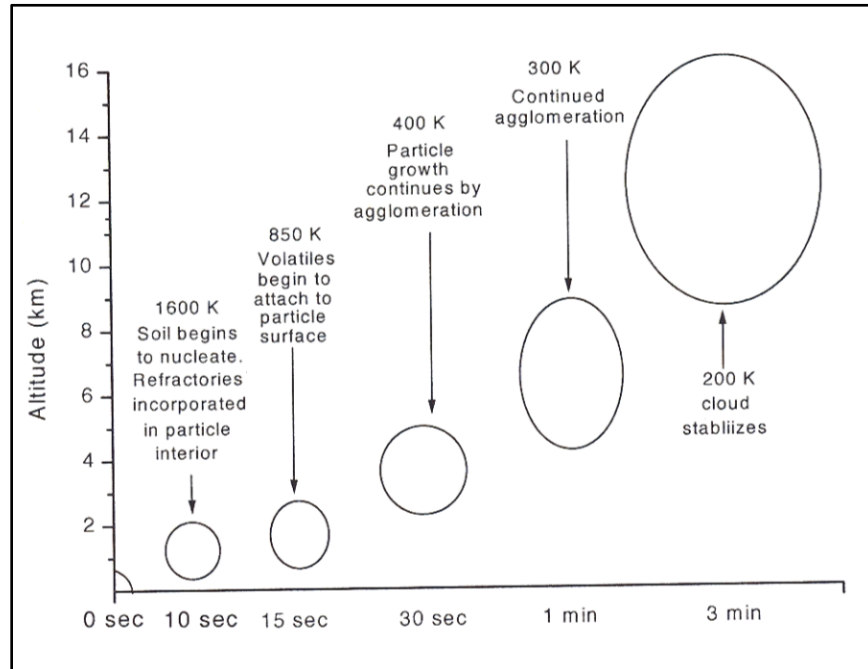


Figure 7. Nuclear Fireball Particle Dynamics [13:403]

The actual shape and size of fallout particles varies with the conditions under which they are formed. Those particles which form from condensation are largely spherical and have radioactivity uniformly distributed throughout the particle [14:409-418]. Particles that form from carrier material that was only partially vaporized or pulled up later through the updraft into the fireball are irregularly shaped with radioactive material concentrated on the surface. As the particles continue to fall, they may continue growth through agglomeration.

Fallout Particle Size Distributions

Numerous studies have been conducted to determine the fallout particle size distributions associated with atomic tests. No distribution describes the particle size

distribution for all atmospheric, surface contact, surface, shallow-buried, or deeply-buried bursts. The distribution of particle sizes varies due to the rate of temperature change in the cloud, debris loading, and condensation temperatures of entrained material.

In a study of local fallout, which included data from 16 Nevada test site events, Baker determined that the vast majority of local fallout samples (deposited within 24 hours) and early-time particles suspended in cloud samples (within several hours) demonstrated very different particle size distributions [18:16]. He noted that particles of $10\mu m$ and larger located at the tropopause (approximately 12 km) would deposit within days while particles of the $1\mu m$ range would take months to deposit from the same altitude.

Baker determined that a bimodal size particle size distribution best explained the “puzzling dichotomy between early and late time debris sedimentation” and could be used to explain cloud debris behavior for surface and air bursts [18:120-128]. He broke his distribution into large and small particles described as (9), where r is particle radius, $N(r)$ is the total population of fallout particles, $N_1(r)$ is the population of smaller-size particles which explains late time fallout behavior, and $N_2(r)$ is the population of larger-size particles that explain early time fallout behavior.

$$N(r) = N_1(r) + N_2(r) \quad (9)$$

Baker tested his distribution by applying it to 97 surface and air-burst events. He applied log-normal, log-normal plus exponential distributions, and hybrid log-normal and power law fits to fallout. He determined that a log-normal distribution, as defined by (10), best explained early and delayed fallout, where r is particle radius, r_{ml} is the median

radius for the small particle group, r_{m2} is the median radius for the larger particle group, β_1 is the logarithmic standard deviation of the small particle group, and β_2 is the logarithmic standard deviation of the larger particle group.

$$N(r) = \frac{N_1}{\sqrt{2\pi}\beta_1} e^{-\frac{1}{2}\left(\frac{\ln(r)-\ln(r_{m1})}{\beta_1}\right)^2} + \frac{N_2}{\sqrt{2\pi}\beta_2} e^{-\frac{1}{2}\left(\frac{\ln(r)-\ln(r_{m2})}{\beta_2}\right)^2} \quad (10)$$

When Baker applied his bimodal distribution, he determined a median particle radius, r_{m1} , of 0.1 microns and a logarithmic slope, β_1 , of 2 effectively described N_1 for all studied events [18:123]. His attempt to determine similar parameters for N_2 did not yield satisfactory results. Using an r_{m2} of 0.2 microns, his results for the β_2 log of slope varied from 3.4 to 6.0 for the sixteen Nevada tests. He determined the variance of his results was related to burst height. His results are supported by Davis' conclusions that the logarithmic slope varies about a mean of 4 [19].

Izrael notes that subsurface or buried bursts will have different fallout particle size distributions but the fallout pattern for a buried crater-producing detonation is similar to that of a surface burst [20:129]. However, for a crater producing burst, the radioactive cloud is split into a base surge cloud and main radioactive cloud, with each containing a fraction of the overall activity. The type, amount, and distribution of radioactive products among the two parts of the cloud depend on the materiel and type of particles forming the fallout [20:136-140]. Izrael states that much of the fallout close to ground zero will not exhibit evidence of fractionation, whereas the surge cloud will have a concentration of radionuclide with gaseous precursors.

Local and Delayed Fallout

Fallout is generally divided into two categories, early and delayed fallout. Early fallout, also known as local fallout, is defined as the fraction of fallout that occurs within 24 hours. The breakdown of total activity between local and delayed fallout varies and may be significantly affected by environmental and atmospheric conditions. In general, local fallout comes from the N_2 fraction of Baker's bi-modal distribution, which contains particles of 20 microns or larger.

The local fallout from land surface bursts generally contains 40-70% of the total activity [14:414]. The local fallout from shallow underground bursts may be slightly higher, and the particle size distribution of the radioactive cloud can change rapidly in the first few minutes after detonation [20:123-124]. Izrael notes that seconds after detonation of a 1.1KT crater-producing detonation buried at 48 meters, "the fraction of particles of diameter smaller than $0.5 \mu m$ did not exceed 1%, with 80% of the total radioactivity on particles larger than $10 \mu m$ "; however, after 18 minutes 90% of the cloud activity was held on particles of $0.5 \mu m$ or smaller. Thus, significantly more than 40-70% of the total activity was deposited locally. Izrael also noted that for more deeply buried shots in which no breaking of the surface occurs and no venting takes place, the majority of radioactive products remain buried in the terrestrial rock around the cavity created by the explosion [20:63-64]. For these types of bursts, only a small part of the radioactive isotopes of inert gases and the most volatile elements escape into the atmosphere.

Particle Fall Dynamics

Although fallout particles are not perfectly spherical, most research treats particle fall as the movement of spheres through a liquid. Bridgman uses a modification of Davies [21:259-270] and McDonald's [22:463-465] work to develop empirical functions that allow calculation of the Reynolds number (R_y) and thus the particle velocity (v) for a sphere falling through air. He defines the term Q as the product of the square of R_y and the coefficient of drag as in (11), where ρ_a is air density, g is gravity, r is particle radius, η is dynamic viscosity, and ρ_p is particle density.

$$Q = R_y^2 C_d = \frac{32\rho_a\rho_pgr^3}{3\eta^2} \quad (11)$$

Bridgman's equation (12) describes particles with a $Q < 140$ and a particle size of greater than 1 micron and (13) describes particles with $100 < Q < 4.5 \times 10^7$, allowing explicit solution for the Reynolds number.

$$R_y = \frac{Q}{24} - 2.3363 \times 10^{-4} Q^2 + 2.0154 \times 10^{-6} Q^3 - 6.9105 \times 10^{-9} Q^4 \quad (12)$$

$$\log_{10}(R_y) = -1.29536 + 0.986[\log_{10}(Q)] - 0.046677[\log_{10}(Q)]^2 + 0.0011235[\log_{10}(Q)]^3 \quad (13)$$

Davies determined the particle terminal velocity for a sphere falling in a viscous media is related to the Reynolds number by (14).

$$v = \frac{R_y \eta}{2\rho_a r} \quad (14)$$

Thus, for non-Stokesian particles, roughly those with a particle radius of larger than 10 microns, Bridgman's equations can be used to determine the Reynolds number and equation (14) can be used to determine particle fall speed. Of note in this analysis is that

particles that do not meet Bridgman's minimum requirements must be treated as Stokesian.

Particle Transport

As cloud debris and radioactive particles fall through the atmosphere, they are affected by horizontal winds as well as up- and down-drafts. Given the same wind conditions for all particles, larger particles will reach a faster terminal velocity than smaller particles. In a United States Standard Atmosphere, with generic atmosphere conditions, particles will fall faster at higher altitudes than at lower altitudes simply due to atmospheric density differences.

In theory, a single particle falling through the atmosphere could be traced from its point of stabilization (its locus following the dynamic rise due to the explosion—its start point), through a varying wind field, and to deposition. However, single particle tracking is not done in fallout deposition models because it is too computationally intensive and time consuming. In practice, transport models are used to track the movement of a distribution of suspended particles through the atmosphere. The two prevalent models that have been used to transport and deposit fallout can be categorized as disk tosser and smear codes. A transport and deposition model that is very similar to the disk tosser is a wafer tosser. The most significant difference between the two is that disks are modeled with a vertical thickness whereas wafers are not.

The DELFIC model is a disk tosser that transports discrete disks of individual particle size groups from rise to ultimate deposition. Hopkins determined the major advantage of the DELFIC model is that it can be used to transport the radioactive cloud

through actual winds [23:5]. The major disadvantages include incompatibility with modern atmospheric modeling programs and computational cost. It should be noted that the computational efficiency of modern computers has increased dramatically since the time of Hopkins' research and computational cost may no longer be as significant an issue.

Contrastingly, Smear codes take a vertical distribution of activity and "smear" it on the ground. The major advantage and disadvantage of Smear codes, respectively, are ease of use and an inability to include 4-dimensional wind fields. Hopkins developed a hybrid method that allowed use of a smear code with time-varying winds [23]. He was able to produce realistically curved "hotlines" with real winds allowing computation of dose rates near the "hotline." He also determined that transport of disks through varying winds provides no improvement over a smear code. Hopkins' later research involved the development of a transport model using variable spectral winds that effectively modeled ash deposition from the Mount St. Helen's eruption [15].

Concentration Dilution During Transport

As a plume of material is transported through the atmosphere, it undergoes some form of dilution. The simplest means of accounting for dispersion is to use a Gaussian dispersion model. This type of model assumes that random dispersive processes produce a "normal distribution" with a predictable standard deviation. Bridgman made this assumption when he developed (15) to describe the volumetric activity density at any time and location in a radioactive cloud when using a smear code.

$$A(x, y, z, t) = A(t) \left\{ \frac{1}{\sqrt{2\pi}\sigma_x(t)} e^{-\frac{1}{2} \left[\frac{x-v_x t}{\sigma_x} \right]^2} \right\} \left\{ \frac{1}{\sqrt{2\pi}\sigma_y(t)} e^{-\frac{1}{2} \left[\frac{y}{\sigma_y} \right]^2} \right\} \left\{ \sum_{g=1}^G \frac{1}{G\sqrt{2\pi}\sigma_z(t)} e^{-\frac{1}{2} \left[\frac{z-z_c^g(t)}{\sigma_z^g} \right]^2} \right\} \quad (15)$$

The standard deviations in the x and y directions, σ_x and σ_y , are calculated from (6).

Jodoin [5] determined toroidal motion of the cloud continues after stabilization and Pugh [17:31] determined an empirical relationship (16) linking yield and diffusive growth, where z_c^o is the stabilized cloud center height at the time of stabilization (defined here as $t = 0$) and T_c is an empirical growth constant.

$$T_c = 12 \frac{z_c^o}{18.28} - 2.5 \left(\frac{z_c^o}{18.28} \right)^2 \quad (16)$$

The toroidal-induced diffusive growth is described by (17), where σ_o is the stabilized cloud deviation. Note that the diffusive growth becomes constant after three hours.

$$\sigma_{diff}^2 = \frac{8\sigma_o^2 t^*}{T_c}, \text{ where} \quad (17)$$

$$t^* = t \text{ for } t \leq 3 \text{ hours}$$

$$t^* = 3 \text{ for } t > 3 \text{ hours}$$

The effective horizontal growth of the cloud during transport is related to the deviations of the rise and diffusive growth by (18).

$$\sigma_{effective}^2 = \sigma_{x,y}^2 + \sigma_{diff}^2 \quad (18)$$

Time Rate of Change of Activity

In 1948, Kathrine Way [24] and E. P. Wigner developed a theoretical treatment of radioactive decay and determined a simple approximation to describe the time

dependence of dose rate to the one hour dose rate as described by (19) [14:392] and as seen in Figure 8.

$$\dot{D}_{Gd}(t) = \dot{D}_{Gd}(1)t^{-1.2} \quad (19)$$

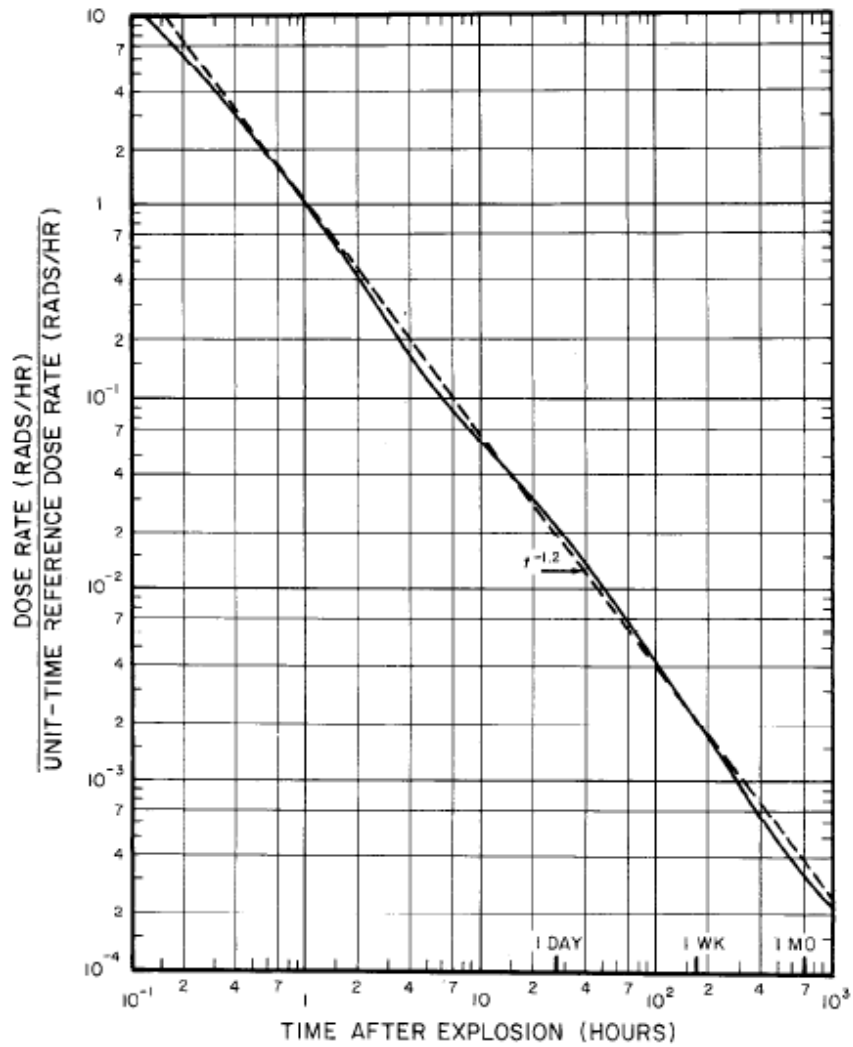


Figure 8. Way-Wigner Decay Versus A Calculation of Individual Fission Products [14:393]

Figure 8 shows that (19) does not perfectly match the decay of individual fission products but that it is behaviorally correct and provides approximate values. The Way-Wigner

decay law was used to adjust dose rates throughout this research. Equation (19) is used to convert HPAC 48-hour dose rate contours to H+1 hr dose rate contours. Although the FDC program created by the author performs all calculations using H+1 hr dose rates it can be adjusted using (19) to calculate dose rates at other times.

DNA-EX

The DNA-EX “serve[s] as an unclassified source of information and data concerning the atmospheric nuclear test program conducted by the United States prior to 1963” [25]. Table 1 lists descriptive information taken from the DNA-EX for each of the tests considered in this research. Dose rate contour plots used throughout this thesis have also been taken from the DNA-EX. Note that the DNA-EX latitude and longitude for Priscilla are incorrect [11:9] and the corrected values are listed Table 1.

Table 1. DNA-EX Tests Studied

OPERATION: Test	Date and Time (Zulu)	Location (DD.MM.SS)		Yield [KT]	HOB [ft] Cloud Top [ft]
		LAT	LON		
Tumbler Snapper: George	01JUN1952 1155	37.02.53	116.01.16	15	300 37000
Teapot: ESS	23MAR1955 2030	37.10.06	116.02.38	1	-67 12000
Teapot: Zucchini	15MAY1955 1200	37.05.41	116.01.26	28	500 40000
Plumbbob: Priscilla	24JUN1957 1330	36.47.53	115.55.44	37	700 43000
Plumbbob: Smoky	31AUG1957 1230	37.11.14	116.04.04	44	700 38000
SUNBEAM: Johnie Boy	11JUL1962 1645	37.07.21	116.19.59	0.5	-1.9 5153

It is important to note that there is little uniformity in data collection methods and techniques among tests [25:2-3]. In the case of larger yield weapons, data could not be

collected until hours, and sometimes days, after detonation. The dose rate contour plots were constructed from measurements taken at different times and locations. Dose rates were adjusted to H+1 hour quantities using the Way-Wigner approximation.

The DNA-EX includes wind data from the surface to, at a minimum, the tropopause height for each test. Data were recorded as close to detonation time as possible. Wind data is also available for select tests after detonation.

Table 2 indicates available ground-zero wind data.

Table 2. Ground Zero Wind Data Availability

OPERATION: Test	Available Winds
Tumbler Snapper: George	H-hr
Teapot: ESS	H-hr
Teapot: Zucchini	H-hr
Plumbbob: Priscilla	H+1hr H+4hr
Plumbbob: Smoky	H-hr H+3hr
SUNBEAM: Johnie Boy	H-hr H+1hr

Reanalysis Weather Data

Reanalysis weather data is created by taking known weather observations and using a weather modeling program to create a spatially and temporally refined weather grid. Hultquist provides an excellent example of the use of weather reanalysis data to analyze past events [26]. He demonstrated that weather reanalysis data could be used to recreate the conditions that likely led to the sinking of the Edmund Fitzgerald.

In a previous effort to recreate dose-rate contour plots, Pace used reanalysis weather data created using the National Weather Service's National Centers for Environmental Prediction (NCEP) T62/28 global spectral model [11:13-14]. He created reanalysis weather data for a hemisphere (180 degrees of latitude and 360 degrees of longitude) at six hour intervals into a grid of 73 x 144 points. This equates to a spatial resolution of approximately 273km x 213km. The vertical range of his reanalysis weather included 17 pressure levels up to 60 km in the atmosphere.

Jones used Pace's reanalysis weather data to create the high resolution mesoscale reanalysis weather data of interest to this thesis [12]. He used Pace's reanalysis weather data and processed it through the Colorado State University Regional Atmospheric Modeling System (RAMS) software to create a 4-dimensional high resolution weather forecast. Jones' weather grid provides high resolution mesoscale reanalysis weather data at 1-hour intervals and 11 pressure levels for over 60 hours for a spatial domain of 74 x 60 points covering 4.6 degrees latitude and 7.1 degrees longitude. This equates to a spatial resolution of approximately 7km x 10km. Table 3 shows the southwest and northeast corners of the available weather data for each test. Note that the grid points are flat-earth distances from ground zero. The origin of the grid is located at ground zero for

each test. It is important to note that Jones' reanalysis weather data did not cover the entire area for all of the DNA-EX dose rate contours.

Table 3. High Resolution Mesoscale Reanalysis Weather Grids

OPERATION: Test	Southwest Grid [km, km]	Northeast Grid [km, km]	Limiting Factor
Tumbler Snapper: George	(-285,-298)	(347,217)	Weather (217 km N)
Teapot: ESS	(-283,-311)	(349,203)	DNA-EX (200 km E)
Teapot: Zucchini	(-285,-303)	(348,212)	DNA-EX (275 km E)
Plumbbob: Priscilla	(-202,-382)	(426,133)	DNA-EX (360 km E)
Plumbbob: Smoky	(-281,-314)	(351,201)	Weather (350 km E)
SUNBEAM: Johnie Boy	(-256,-306)	(374,209)	DNA-EX (115 km N)

In the case of detonations George and Smoky, Jones' high resolution reanalysis weather cut off before the DNA-EX dose rate contours ended. In all other cases, the DNA-EX dose rate contours ended or were cut-off within the reanalysis weather grid. Figure 9 shows the spatial relationship between the DNA-EX dose rate contours and Jones' reanalysis weather data grid.

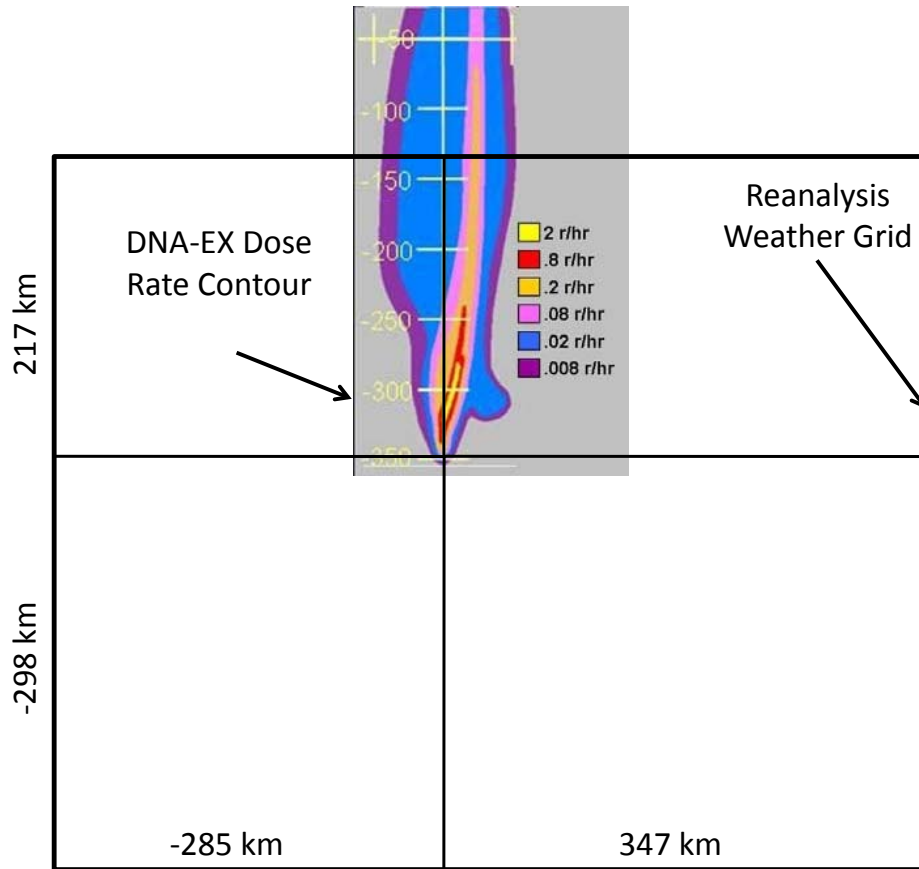


Figure 9. DNA-EX Dose Rate Contour for George And High Resolution Mesocale Reanalysis Weather Grid

Comparison of Observations and Predictions

The effectiveness of a transport and dispersion model to predict dose rate contours is measured by how well it can predict both the physical extent of contamination and how it is distributed. The Measure of Effectiveness (MOE) and Normalized Absolute Difference (NAD) techniques discussed subsequently allow such a comparison. Warner et al. provide more detailed explanations of these techniques, as well as application examples [27].

Measure of Effectiveness

The MOE provides a way of comparing the physical extent of contamination predicted in a model to that of historical data. The MOE may be used to compare modeled dose rate contour plots to those of the DNA-EX. The basic premise is to compare predictions against observations and to correct for errors in prediction [27]. The area where the model correctly predicts observed fallout is known as the area of overlap, A_{OV} . Errors in prediction fall into two categories: false positive or false negative. The area of false positive, A_{FP} , is that area for which the model predicts fallout deposition where none was observed. The area of false negative, A_{FN} , is the area where the model fails to predict fallout where it was actually observed. Figure 10 demonstrates a graphical depiction of these areas [27:59].

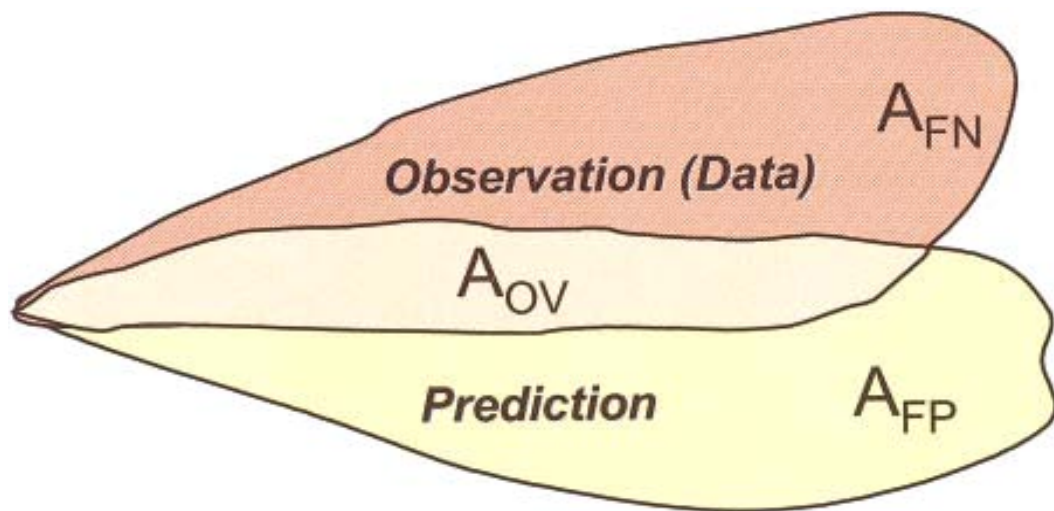


Figure 10. Areal Components for MOE Comparison [27:59]

The MOE may be expressed mathematically as (20), where A_{PR} is the area of the prediction and A_{OB} is the observed area [27:59].

$$MOE = (x, y) = \left(\frac{A_{OV}}{A_{OB}}, \frac{A_{OV}}{A_{PR}} \right) = \left(1 - \frac{A_{FN}}{A_{OB}}, 1 - \frac{A_{FP}}{A_{PR}} \right) \quad (20)$$

The effects of A_{FN} and A_{FP} on the $MOE(x,y)$ are displayed graphically in Figure 11. In this case, the line $y = x$ represents the case where the size of the fallout area predicted equals that of the actual area observed. Movement along the line $y = x$ from the point of no overlap (0,0) to that of perfect overlap (1,1) indicates an increase in the overlap between the predicted areas.

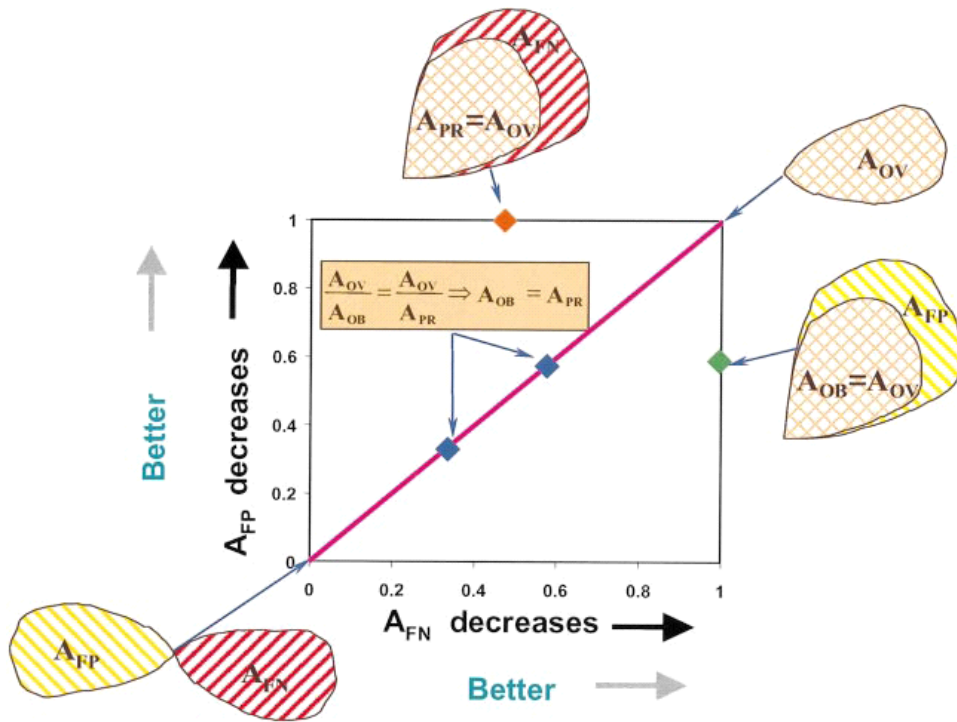


Figure 11. Key Characteristics of 2-D MOE Space [27:60]

Deviation from the line $y = x$ indicates a change to A_{FN} or A_{FP} as depicted. Any $MOE(x,1)$ indicates that the A_{OV} is completely accounted for by the A_{PR} . The size of the x -value, from 0 to 1, inversely corresponds to the A_{FN} . Likewise, any $MOE(1,y)$ indicates that the A_{PR} completely encapsulates the A_{OV} and the y -value is inversely

related to the A_{FP} . From the established relationships of the MOE components, the x and y location on the graph is defined by (21) [27:59-62].

$$\begin{aligned} x &= \frac{A_{OV}}{A_{OV} + A_{FN}} \\ y &= \frac{A_{OV}}{A_{OV} + A_{FP}} \end{aligned} \quad (21)$$

Normalized Absolute Difference

The NAD provides a way of comparing model predictions to observed values. Mathematically, the NAD (22) calculates the normalized scatter between observed and predicted concentrations. It may be expressed in terms of the A_{FP} , A_{FN} , and A_{OV} regions. NAD values range from 0 to 1, with a lower value indicating a closer match between observed and predicted values.

$$NAD = \frac{A_{FN} + A_{FP}}{A_{FN} + A_{FP} + 2A_{OV}} \quad (22)$$

Substituting (21) into (22) yields (23), mathematically relating the NAD and the MOE [27:65].

$$NAD = \frac{x + y - 2xy}{x + y} \quad (23)$$

Figure 12 shows the relationship between NAD isolines and the MOE plotted against the same axes as Figure 11. Generally, as the NAD gets smaller, the MOE demonstrates better spatial correlation between predictions and observations. From Figure 12 it is apparent that, when interpreted together, the MOE and NAD can provide quantitative information which provides insight as to how the model differs from observation. In

general, a high NAD indicates a good match. However, from the MOE, one may be able to determine where the model is failing, e.g. overestimation of A_{FN} or A_{FP} .

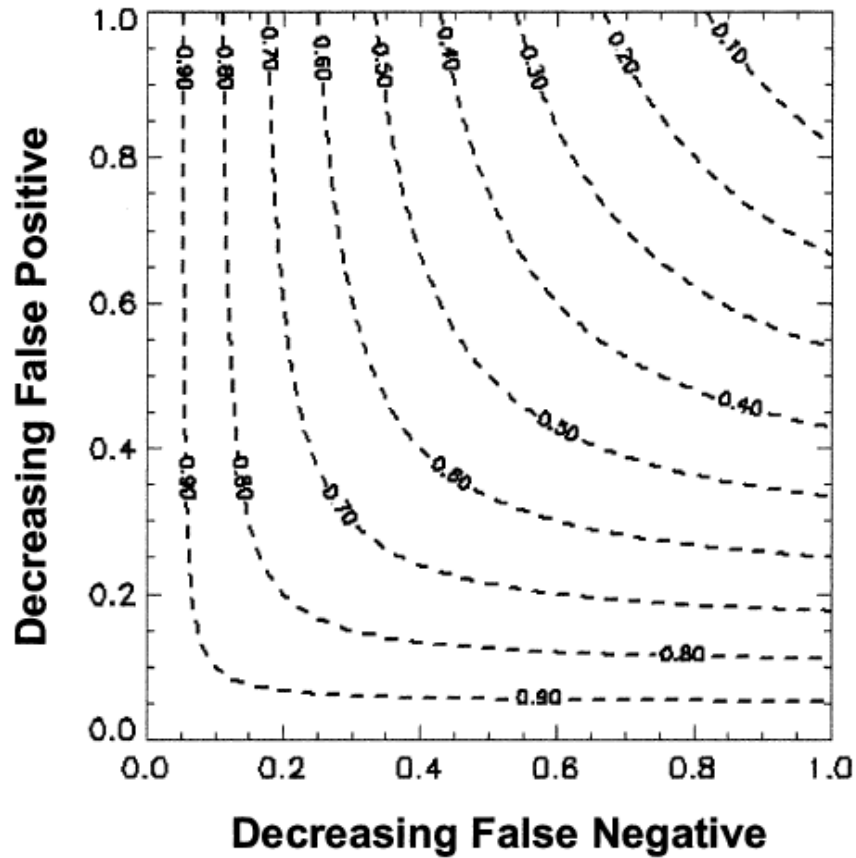


Figure 12. NAD Isolines in 2D MOE Space [27:65]

Figure of Merit

The Figure of Merit (FOM) used in this thesis capitalizes on the MOEs' ability to describe spatial deposition differences and the NAD's ability to describe concentration differences between model predicted and historic dose rate contours. The MOE_x , MOE_y , and NAD may be combined as (24).

$$FOM = \frac{NAD}{\sqrt{MOE_y \cdot MOE_x}} = \frac{\frac{A_{FN} + A_{FP}}{2 \cdot A_{OV} + A_{FN} + A_{FP}}}{\sqrt{\left(1 - \frac{A_{FP}}{A_{PR}}\right) \left(1 - \frac{A_{FN}}{A_{OB}}\right)}} \quad (24)$$

The range of FOM values includes all non-negative numbers. For a perfect prediction FOM equals zero. A FOM increase indicates a decrease in model prediction accuracy.

If an observed dose rate contour is known for a specified area of interest (AOI), one can deduce how the FOM will behave over a range of yields. In this research, the area of interest was limited to (unless further limited by the DNA-EX or reanalysis weather data grids) the area enclosed by a 200 x 200 mile square centered at ground zero. The area of observation, A_{OB} , is fixed, and the only variables that can change are A_{FN} , A_{FP} , and A_{OV} . The potential A_{OV} is limited by the A_{OB} .

The expected numerical behavior of the FOM can be deduced by considering MOE_x , MOE_y , and NAD values for a range of yields. For a yield much smaller than the actual yield, the observed dose rate contour will dwarf the predicted dose rate contour. The MOE_x value will be a very small number because the A_{FN} is very small compared to the A_{OB} . The MOE_y value will be close to one because the A_{PR} is mostly contained within the A_{OB} , limiting the A_{FP} . The NAD should approach one because the A_{OV} for the two dose rate contours is very small compared to the A_{FN} . Thus, for very small yield values, the FOM will be larger than one.

For a yield much larger than the actual yield, the predicted dose rate contour contains the observed dose rate contour. The A_{OV} has reached a value that is equal to the A_{OB} . The A_{FN} is zero so the MOE_x is forced to one. The MOE_y will approach constant

value of less than one that is equal to the ratio of the A_{OB} to the AOI. With the A_{FN} equal to zero, the NAD value will approach a constant value that is defined by (25).

$$NAD = \frac{A_{FP}}{2 \cdot A_{OV} + A_{FP}} \quad (25)$$

Thus, the FOM should approach a value defined by (26).

$$FOM = \frac{A_{FP}}{2 \cdot A_{OV} + A_{FP}} \sqrt{1 - \frac{A_{FP}}{A_{PR}}} \quad (26)$$

For a range of yields closer to the actual yield, the FOM will move to a lower value. Theoretically, given a perfect prediction, the FOM would reach a value of zero. The actual numerical value of the FOM, as well as its behavior in this yield range, will vary based on how the A_{OV} , A_{PR} , A_{FN} , and A_{FP} change.

Yield Estimates and Error in FOM

The FOM places equal emphasis on comparing the physical extent of contamination, quantified by the MOE, and the difference between the predicted and observed dose rates, as quantified by the NAD. The lowest FOM value will occur at a yield—designated as the best-fit yield—that best reproduces the DNA-EX dose rate contour. Error in FOM measurement provides a quantifiable relationship between dose rate contours and associated yields. The Error in FOM is defined by (27), where FOM_{BF} and FOM_i are the FOM for the best-fit yield and the yield being considered, respectively.

$$\text{Error in FOM} = \frac{FOM_i}{FOM_{BF}} \quad (27)$$

The behavior of the Error in FOM depends on how well the model recreates the DNA-EX dose rate contour and the sensitivity of the model to changes in yield. If a model could recreate a DNA-EX dose rate contour perfectly at the actual weapon yield, the Error in FOM measurements would depend only on model's sensitivity to yield changes. Since neither HPAC nor the FDC is a perfect model, the Error in FOM measurements will depend both on how well dose rate contours can be recreated and model sensitivity to yield changes.

MOE-NAD Isoline Graph

The relationship of a dose rate contour to the MOE_x , MOE_y , and NAD can be represented in graphical form. Figure 13 shows the relationship of various dose rate contours and their placement on a plot of MOE_x and MOE_y with NAD isolines. For observed and predicted dose rate contours with almost no overlap, but with large A_{FP} and A_{FN} areas, the NAD is large and the MOE values plot in the lower left quadrant of the chart. As the A_{FN} decreases while the A_{FP} remains large, the NAD value would move to the right along the Decreasing False Negative axis. In the case of an A_{FP} decrease with a large A_{FN} , the NAD value would move up along the Decreasing False Positive axis. An increase in overlap and equally decreasing A_{FP} and A_{FN} values demonstrates a better match of predicted and observed dose rate contours, and moves up and to the right along the line $A_{FP} = A_{FN}$.

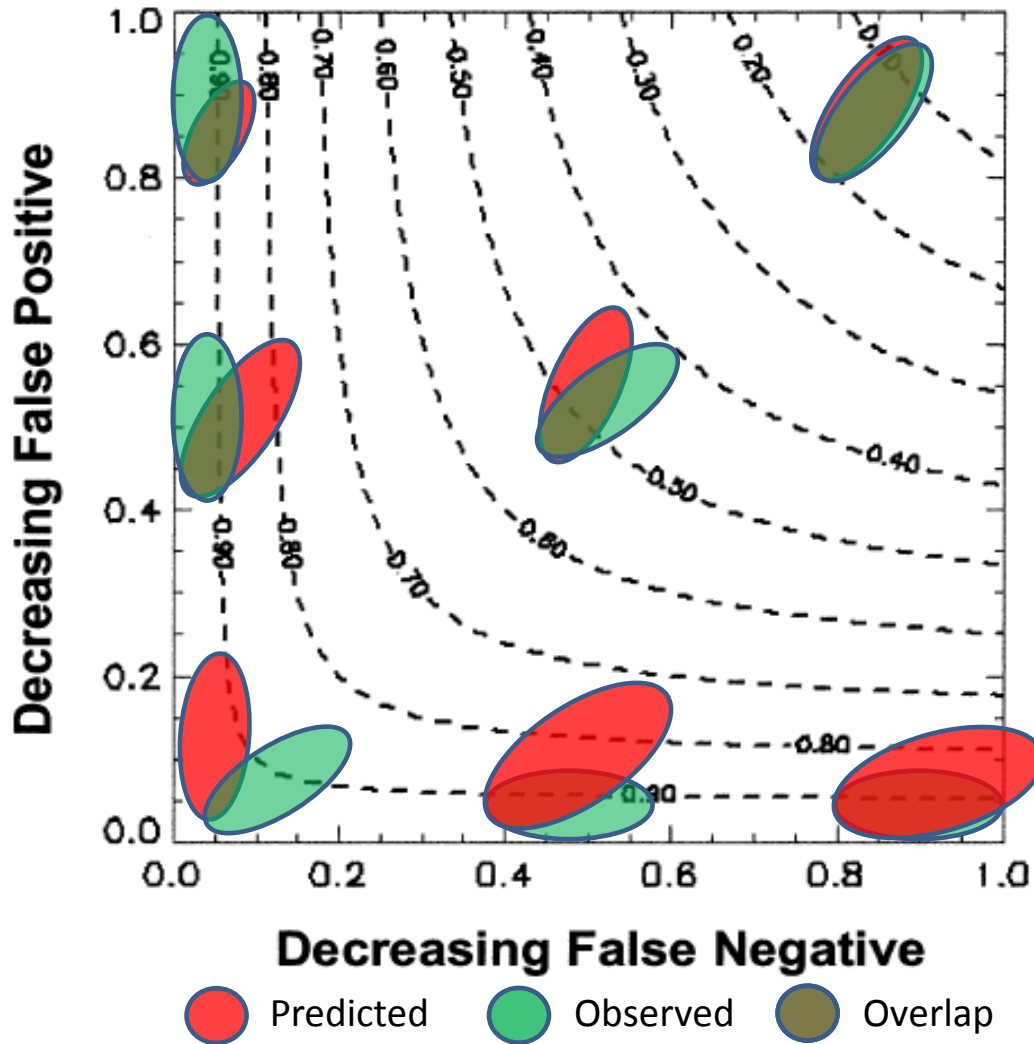


Figure 13. Relationship of Dose Rate Contour Behavior and MOE-NAD Graph Placement

MOE-NAD Isoline Behavior for Low Yields

As previously stated, the behavior of the MOE_x , MOE_y , and NAD for yields much lower and higher than the actual yield can be deduced. For yields between the low and high end yields, the behavior is less certain. If the weather and model were perfect, the FOM would approach zero at some yield. In this case neither the weather nor the model is perfect but some general observations can be noted.

For lower-end yield estimates, the predicted dose rate contours cover only a fraction of the A_{OB} so the MOE_x must be a number much smaller than one. Since the yield is much smaller than the actual yield, the bulk of the A_{PR} is contained within the A_{OB} so the MOE_y approaches one. Since the A_{OV} is small compared to the sum of the A_{FN} and A_{FP} , the NAD will approach one. Numerically, the FOM should be a relatively large number. From a graphical perspective, the small yield dose rate contour severely under-predicts the actual dose rate contour and will be located in the upper left quadrant of a MOE-NAD Isoline graph.

Capped and Uncapped Cloud Tops and Vertical Distribution of Activity

The vertical distribution of activity in a radioactive cloud after an explosion will certainly affect subsequent fallout deposition. The DNA-EX lists the observed cloud top height for all six tests studied in this thesis. The values of the DNA-EX cloud top heights are accepted as true. For a given yield, the FDC calculates the distribution of activity using (5). The activity distribution for each particle size group is calculated up to a particle-size dependent stabilization height, Z_{ct}^g , defined by (8).

Figure 14 shows an example distribution of activity for a stabilized cloud. Note that some of the activity appears as a tail near ground elevation. This is the fraction of activity from the particle size groups that had a stabilization height at or below ground level. This activity is placed at 10m above ground level and deposits at ground zero during the first time step.

For an uncapped cloud top, the initial activity distribution is accepted as shown. For capped cloud tops, the FDC forces all activity (through normalization) into the

fraction of the distribution that is below the observed cloud top height. For each particle size group, the distribution below the cloud top is normalized and the total activity from the equal activity particle size group is distributed proportionally to the normalized distribution below the observed cloud top.

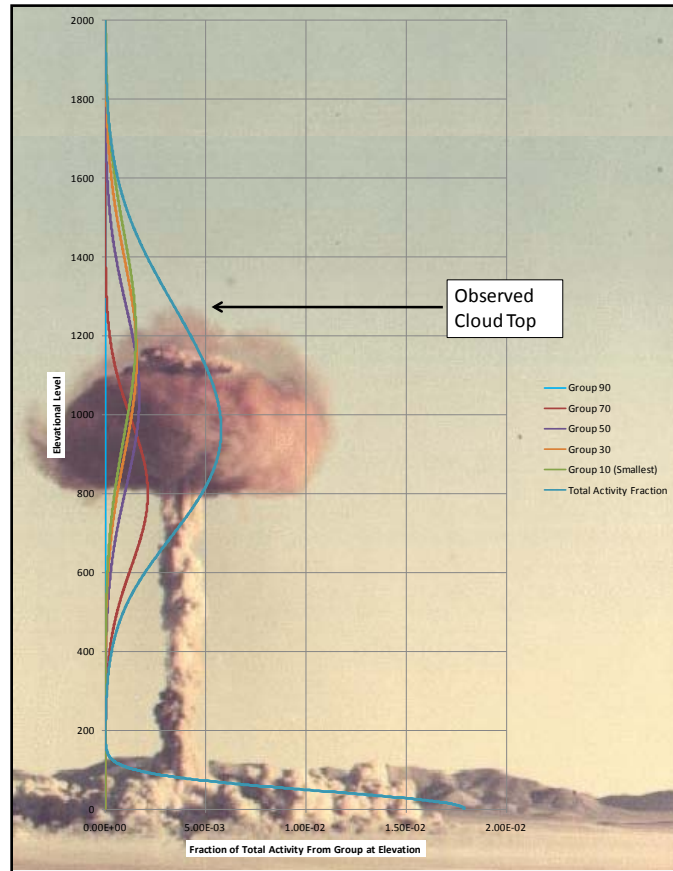


Figure 14. Activity Distribution of Initial Stabilized Cloud

MOE-NAD Isoline Behavior for Capped and Uncapped Cloud Tops

For both capped and uncapped cloud tops, the vertical distribution of activity and winds will determine what fraction of activity is deposited within the AOI. It is

important to note that for any particles that are grounded prior to the switch from ground-zero winds to reanalysis winds, the horizontal distribution of an activity wafer changes with yield but the center of deposition for the wafers do not change.

For both capped and uncapped cloud top iterations, if the cloud top height does not exceed the observed cloud top, then the specific fractions of activity that will deposit within the AOI will be very similar. The dose rate contours for capped and uncapped cases will be the same for the same yield. A plot of the MOE_x and MOE_y values for these yields on a MOE-NAD Isoline graph will overlap each other.

For capped cloud tops in which the calculated cloud top exceeds the observed cloud top, the fraction of total activity deposited will remain the same as the fraction of total activity deposited for the case where the calculated and observed cloud tops are the same. Since the deposition centers for the wafers of particles are deposited in the same location but the horizontal distributions of the activity have changed, the overall shape (but not the values) of the dose rate contours should remain similar. The MOE_x , MOE_y , and NAD will vary less with incremental changes in yield and the data points for the varying yields will begin to stack up on a MOE-NAD Isoline graph.

For uncapped cloud tops in which the calculated cloud top exceeds the observed cloud top, the fraction of total activity deposited in the AOI is reduced. A plot of the MOE_x and MOE_y values for these yields against their capped cloud top counterparts on a MOE-NAD Isoline graph may diverge as the vertical distribution of activity between the clouds becomes more disparate.

III. Approach

This section provides an overview of the methodology used to reproduce dose rate contours, compare them to historic values, and to estimate weapon yield from inversion of dose rate contours. HPAC, due to its widespread employment throughout DTRA and other organizations, was selected as the industry standard to compare to a user developed FDC. An in-depth explanation of program development and program validation are addressed. A schematic providing an overview of the problem solving approach taken is displayed in Figure 15.

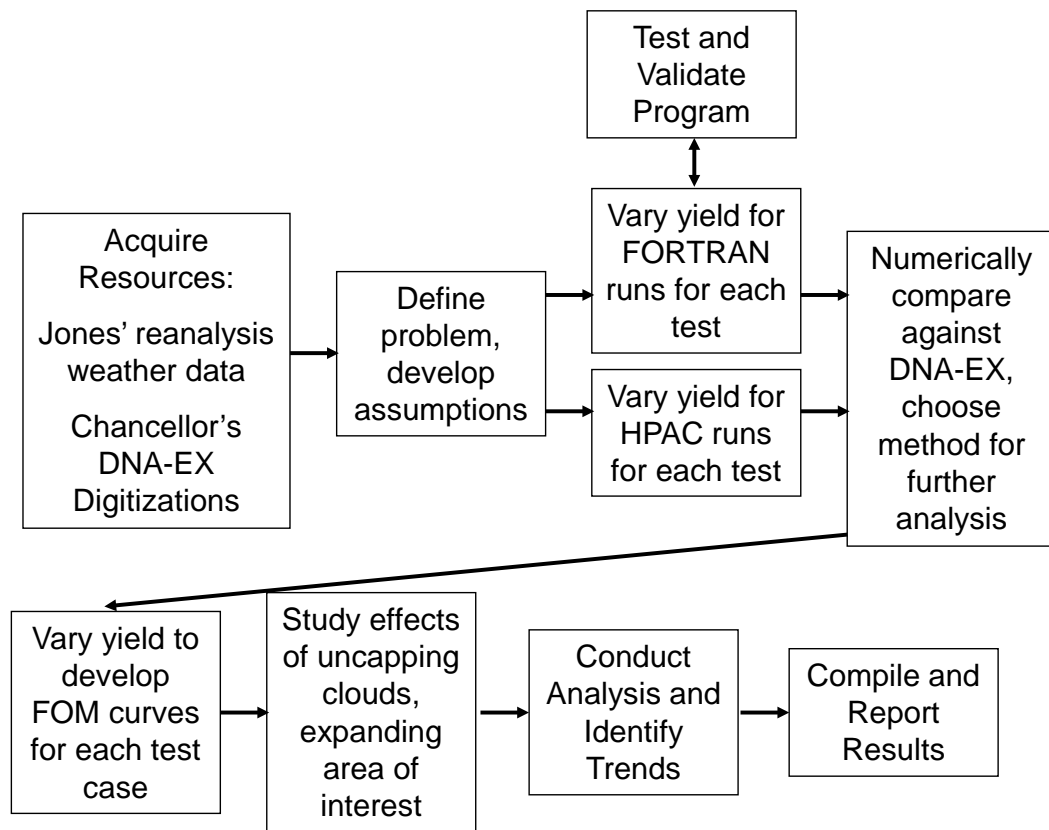


Figure 15. Problem Solving Approach

Program Development

The overall goal of the FDC program was to create a tool that efficiently and effectively models nuclear fallout. Critical to FDC validation was the ability to create fallout patterns that closely matched dose rate contours from the selected tests while minimizing computational time and complexity.

Program Selection

Different versions of smear and disk tossing programs were considered. The author developed a traditional AFIT smear program and a modified wafer-tosser program, the FDC. The smear program forced the entire height of the cloud to translate with the same velocity as activity was deposited on the ground, limiting the effects of winds at altitude. The wafer-tosser program accounted for changes to wind velocity at altitude, allowing for independent transport and deposition of each wafer. The FDC was employed for future study because it provided better results than the smear program.

Fallout Deposition Code Concept Development

The FDC was initially designed to model the movement and deposition of a single particle. At the time of stabilization, the particle would have a certain amount of activity. From its location in the cloud at the time of stabilization, it would begin to fall. The particle would quickly reach its terminal velocity and gradually slow down as the density of the atmosphere increased. The amount of time the particle would remain aloft is characterized by (28), where z_o is the initial particle height, z_{gz} is the deposition height, and v_{avg} is the average fall velocity.

$$t_d = \frac{z_o - z_{gz}}{v_{avg}} \quad (28)$$

Lateral movement during particle fall was determined by the effects of the horizontal winds, with the particle ultimately settling at some lateral distance from its initial location described by (29).

$$\begin{aligned} x_{dep} &= x_i + \int_0^{t_d} v_x(z, t) dt \\ y_{dep} &= y_i + \int_0^{t_d} v_y(z, t) dt \end{aligned} \quad (29)$$

The FDC uses linear approximations to solve equations (28) and (29), and subsequently transports all wafers for each particle group size to deposition. The activity in each slab is transported as a wafer with no vertical thickness. The activity in each wafer is equal to the fraction of activity for the associated particle group that was present in a corresponding slab of discrete thickness in the initial stabilized cloud. The fall velocity for the individual particle is treated as the mean velocity of the wafer. The distribution of particles within the wafer is modeled using a simple Gaussian distribution around the deposition center.

Fallout Deposition Code Assumptions

Several assumptions were made to ensure code simplicity and computational efficiency. The general assumptions include:

- No agglomeration during particle fall
- No vertical winds
- Baker's bi-modal distribution of activity applies
- 100 equal activity particle size groups
- Activity is volumetrically distributed
- Vertical and horizontal distribution of activity within a particle group are Gaussian

Fallout Deposition Code Structure

An overview of the code is presented in Figure 16. The main program, Fallout, is the computational backbone. In sequence, for a single test shot, the program creates equal activity size groups, calls test shot information, computes an initial stabilized cloud, and reads in wind data. By radius group, the program calculates disk translation, updates dispersion, and allocates activity to each wafer. (Although not used, the program also has the ability to determine the highest-altitude wafer that must be considered for deposition to occur based on a scenario run time.) The code then deposits activity on the ground for each wafer working from the lowest to highest wafer. The process is repeated until all deposition is complete and data is output to a file. Detailed comments are found in the code itself and are on file at AFIT. The important equations, assumptions, and features of each section of the code are conveyed in subsequent sections.

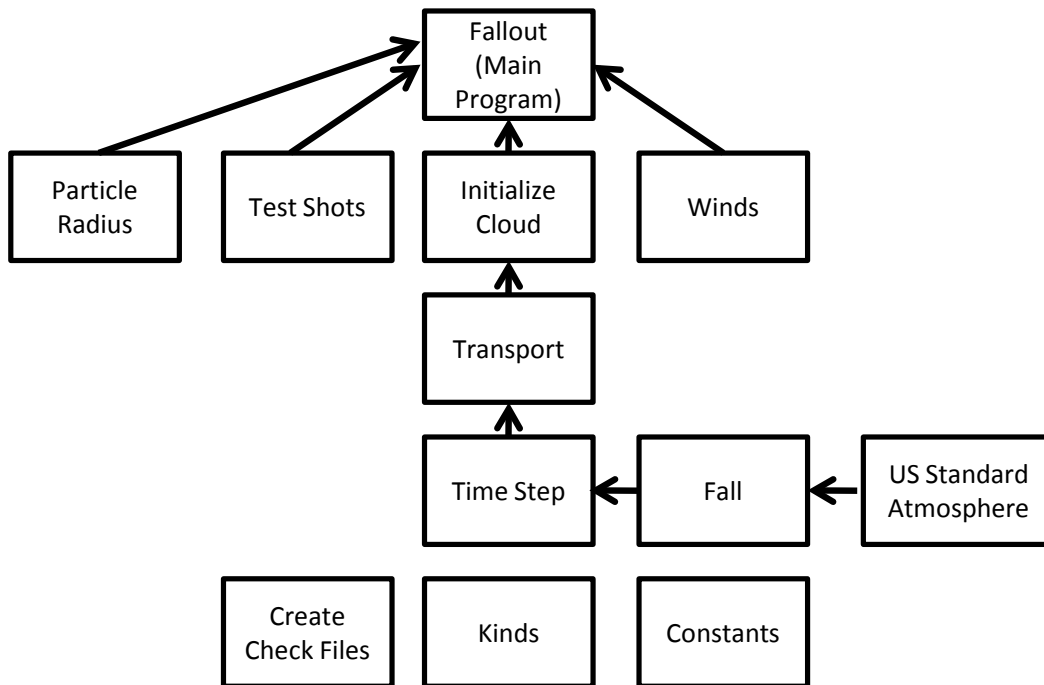


Figure 16. Fallout Deposition Code Framework

Code Highlights

The Main Program serves as the driver to the entire code. It may be modified to allow the code to conduct related tasks. From this program, the user may conduct single wind, temporal winds, or weather reanalysis trials for each detonation.

The Particle Radius module uses a modification of a program that Garcia developed to create 100 volumetrically distributed equal-activity particle size groups [28]. This subroutine creates a user-specified number of equal activity groups, assuming volumetrically distributed activity, and determines particle radii to within 10^{-6} microns. Particle radii are determined by solving the cumulative distribution function (30) at specified intervals.

$$F(x) = \int_0^x \frac{1}{\sqrt{2\pi}} e^{-\frac{1}{2}(x')^2} dx' \text{ where } x' = \frac{\ln(r) - \alpha_3}{\beta} \quad (30)$$

The computational algorithm used to approximate the solution is (31). [29:932]

$$F(x) = 1 - \frac{1}{2} \left[1 + 0.196854x + 0.115194x^2 + 0.000344x^3 + 0.019527x^4 \right]^4 \quad (31)$$

The test shots module defines the key parameters for each of the DNA-EX tests considered, as well as information controlling grid parameterization. The fallout deposition scenario spatial area, run time, height of burst, tropopause height, and cloud top height may be changed here.

The Initialize Cloud module creates the initial stabilized cloud and particle distributions necessary for transport. The Cloud Rise function computes the cloud center height based on Hopkins' empirical fit defined by (1). Particle group standard deviation in the x and y-directions are calculated Pugh's equation (6) and in the z-direction using Connors' equation (7). These deviations are used to create the horizontal and vertical distributions of activity in the initial stabilized cloud using equation (5). Toroidal growth is accounted for using Pugh's equation (16).

The Max Elevation module contains a subroutine that calculates the maximum altitude that needs to be considered based on particle size, fall time, and time of interest. Although not required for functionality, this module decreases run time by eliminating the need to perform calculations on wafers that are not deposited by the time of interest. For purposes of this study, this module was not employed because all wafers were transported to deposition or until they left the deposition grid.

The Winds module contains three separate subroutines. The single and temporal (double) wind subroutines import wind observations from known altitudes, convert to required units, and calculate x and y wind components at all elevation steps. When these subroutines are in use, there is no temporal variation of wind speeds, and the wind speeds only change from vertical movement through the wind profile.

The time-variable winds (reanalysis winds) subroutine accounts for both temporal and spatial variation of winds. The profile of wind speed components are retrieved for the entire spatial and temporal domain. To determine the wind speed at a point of interest, an inverse-distance weighting of spatial and linear interpolation of temporal data is employed.

Wind component values are calculated using an inverse-distance weighted spatial Kriging of 16 known wind velocities surrounding the point of interest for both the start and end of a time step. Equation (32) describes how the weights are calculated, where R is the distance from the interpolation point to the most distant scatter point, h_i is the distance from the interpolation point to the scatter point i , and n is the number of scatter points.

$$w_i = \frac{\left[\frac{R - h_i}{Rh_i} \right]}{\sum_{j=1}^n \left[\frac{R - h_j}{Rh_j} \right]} \quad (32)$$

The wind speeds are calculated using (33), where v_{eff} is the speed at the interpolation point and v_i is the speed in the i^{th} data point. The method is used to calculate wind components in the x-direction (v_x) and y-direction (v_y) separately.

$$v_{eff} = \sum_{i=1}^n w_i v_i \quad (33)$$

The effective wind speed for the wafer is calculated using a linear temporal interpolation between the known wind speeds at the beginning and end of the time steps. The temporal interpolation is described by (34), where v_{x-eff} is the effective speed in the x-direction, $v_{x,i}$ is the speed in the x-direction at the i^{th} time bracket, $v_{x,i+1}$ is the speed in the x-direction at the $i^{th}+1$ time bracket, and t^* is the difference in seconds of the current time and the i^{th} time bracket. A similar equation is used to calculate v_{y-eff} .

$$v_{x-eff} = v_{x,i} + \frac{t^*}{3600}(v_{x,i+1} - v_{x,i}) \quad (34)$$

The program has a built-in check to ensure the linear interpolation time step is limited to 10 seconds or less. If the time step is greater than 10 seconds, the program reduces the time step and repeats the interpolation process.

Figure 17 shows a graphical representation (not to scale) of 16-point spatial Kriging for successive time steps showing a wafer center translating from near the 22 to the 32 grid point.

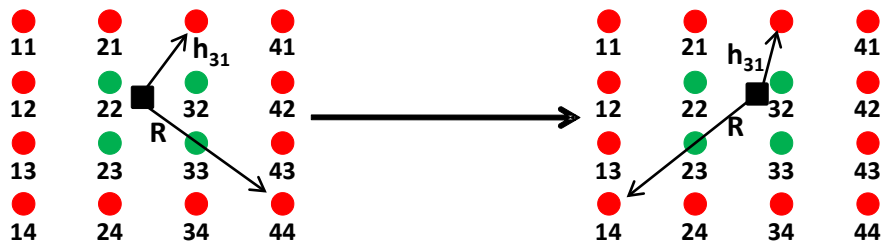


Figure 17. 16-Point Spatial and Temporal Kriging

The Transport module conducts wafer translation and updates wafer lateral dispersion, $\sigma_{effective}$. The Transport module contains separate modules corresponding to the different wind capabilities. The Update Sigma module accounts for toroidal growth during the first three hours of transport and accounts for particle dispersion in the x and y directions separately using Pugh's numerical fit, (6), to calculate the effective dispersion from (18). The Update Sigma also models dispersion in the x and y directions separately using a Pasquill Turbulent Growth (PTG) equation described by (35), where the Pasquill Turbulent Type (PTT) is a weather condition fitting parameter, σ_x is the dispersion in the x direction, and y is the translation of the wafer in the y direction.

$$\sigma_x = PTT \frac{y}{\sqrt{1+0.0001y}} \quad (35)$$

PTT values of 0.16 and 0.11 were used for surface and buried bursts, respectively, which correspond to moderately unstable and slightly unstable boundary layer conditions.

Once the $\sigma_{effective}$ calculated using the PTG dispersive growth is larger than that calculated using Pugh's numerical fit, further dispersion calculations are conducted using the PTG model. This transition from Pugh to PTG dispersive growth was implemented because the PTG better described late time dispersive growth.

An additional feature of the reanalysis transport module is that it integrates terrain into the model. (The single and multiple wind modules operate under a flat earth assumption.) As the wafer center passes from one elevation to the next, the program interpolates elevation data, which is included in the high resolution mesoscale reanalysis weather grid surrounding a disk center, to determine if deposition has occurred.

Other modules include the Time Step module, which calculates the particle fall time for each incremental vertical step; the Fall Module, which uses the US Standard Atmosphere module to determine the particle fall velocity at each altitude step; the Create Check Files module, which creates output files that are used to verify intermediate calculations; the Constants module, which provides constants that are used throughout the program; and the Kinds module, which specifies precision for calculations.

Program Validation

This section describes the methods used to validate the FDC. Program validation focused on verification of numerical correctness of equations, realistic qualitative behavior of all subroutines, and modeling of simple test cases.

Numerical Correctness and Precision

A thorough testing program was essential to development and validation of the FDC. Equations were verified for numerical correctness against Mathematica and/or hand calculations. Each equation was studied and alternative forms of the equation were written to account for the possibility of numerical inaccuracies. Explanations for the different forms of each equation are written directly into the code. Limiting assumptions that could affect the equation applicability are also cited.

Qualitative Behavior

After numerical precision and correctness was verified, each subroutine or function was checked for proper qualitative behavior. Subroutines were created to allow checking of the qualitative behavior of all key subroutines or functions. These check file

subroutines include files to allow checking of group radii; group stabilization heights; group initial top, bottom, and center locations; group initial dispersion in x, y, and z; fall times from one wafer to the next; translation in x and y directions at deposition; and dispersion in x and y directions at deposition.

Modeling Test Cases

The FDC was subjected to a series of simple modeling tests. The behavior of deposition was checked at yields from a range of 0.3KT to 1 MT. A lower limit of 0.3KT was placed on the yield because smaller yields did not produce enough fallout to model them effectively.

The behavior of the FDC was studied for single constant wind for all elevations, layered constant winds, smoothly varying winds in vertical layers, and time changing winds in vertical layers. Time changing winds were studied with abrupt changes at one hour increments and for smooth changing temporally varied winds. Changes to the number of particle size groups, number of wafers, and source normalization constant were also considered. Currently, the program creates 100 equal activity particle size groups but only deposits the largest 81 groups. These particle groups have a radius of 19.357 microns or larger, and were selected because they make up the majority of the local fallout which is of interest in this study. A slab thickness of 50m is used to create wafers from the initial stabilized cloud. The activity within the slab is attributed to a wafer with no vertical thickness. The slab thickness may be decreased in integer increments to 1m; however, no benefit to dose rate contour resolution was noted when

reducing the slab thickness to smaller values. The FDC uses a source normalization

$$\text{constant of } 7.452 \times 10^9 \frac{\text{R}\cdot\text{m}^2}{\text{hr}\cdot\text{KT}}.$$

An example of a generic contour produced using George parameters, with constant wind velocities of $4.47 \text{ m}\cdot\text{s}^{-1}$ (10 mph) from 135 degrees for 10 hours switching abruptly to 45 degrees thereafter, is seen in Figure 18. As expected, the disk that deposits at 10 hours has traveled 160 km along the hotline, equal to translation of 113 km to the west and 113 km to the north.

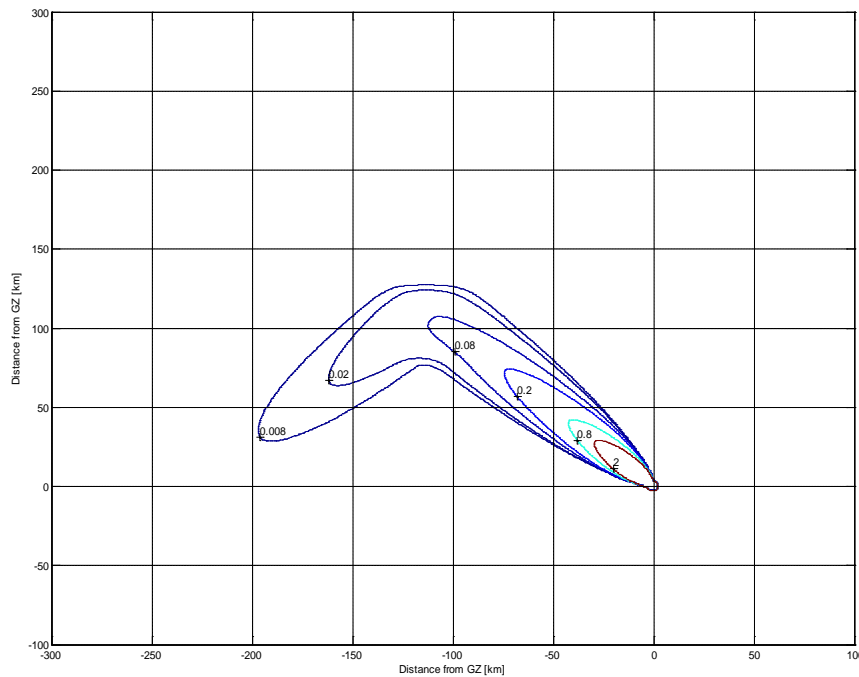


Figure 18. Test Case Dose Rate Contours

A graph of the normalized activity fraction for a single particle group is seen in Figure 19 for an uncapped cloud top.

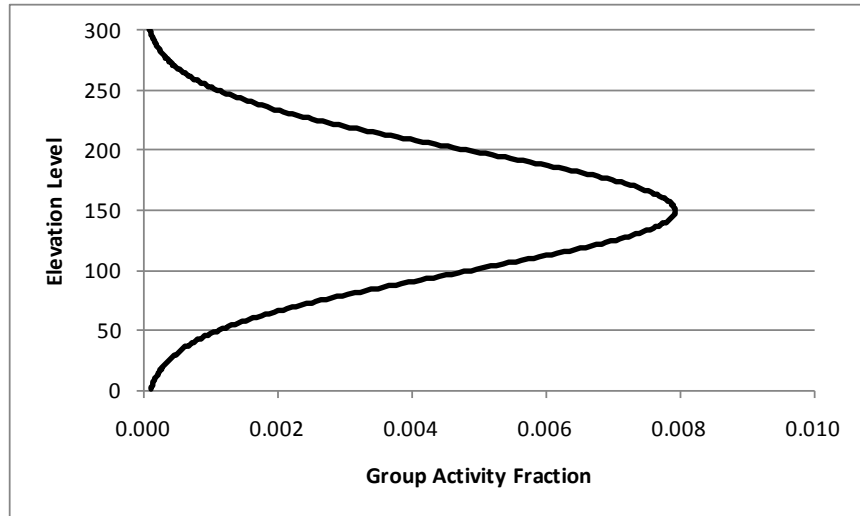


Figure 19. Normalized Vertical Distribution of Activity for 19.357 micron Particle Group

The activity fractions calculated for capped cloud tops is derived from the same vertical distribution. If the vertical distribution exceeds the cloud top height, the distribution is chopped off at the cloud top height, and activity is normalized and forced into the remaining layers.

The dose rate contour for a particle group size of 19.357 microns is shown in Figure 20 with the corresponding horizontal dispersion displayed in Figure 21. The effective dispersions in the x and y directions are equal because the winds selected were 135 and 45 degrees, for which the sine and cosine components are equal.

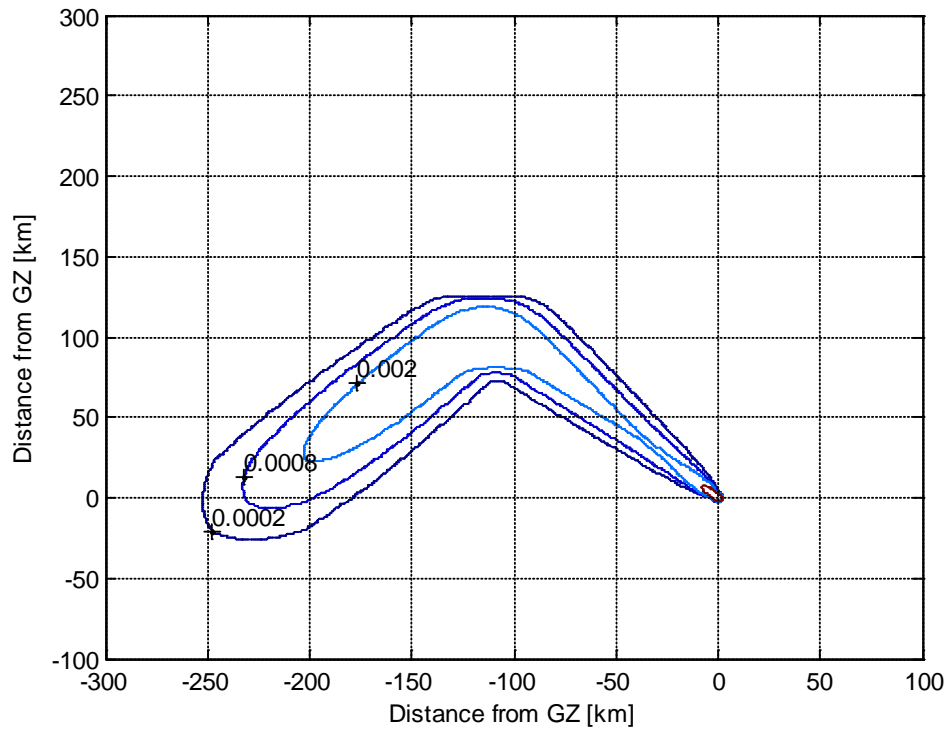


Figure 20. Dose Rate Contour for 19.357 micron Particle Group

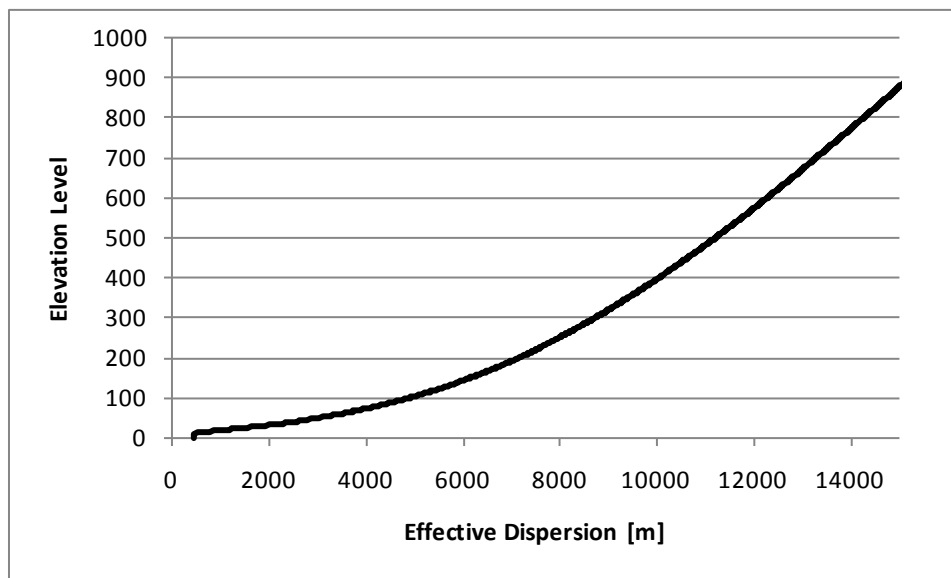


Figure 21. Effective Dispersion in [m] by Elevation Group for 19.357 micron Particle Group

Optimization and Comments

To facilitate FDC use over a broad range of applications, no attempt was made to optimize the code to fit any particular case. The AOI for all cases, except for Johnie Boy, was set to a 200 x 200 mile grid centered over ground zero. For Johnie Boy, the grid was limited to 230km x 230km because the DNA-EX dose rate contour was cut off at 115km north of ground zero. An example of the spatial relationship between the DNA-EX dose rate contour area, weather grid, and AOI is shown in Figure 22.

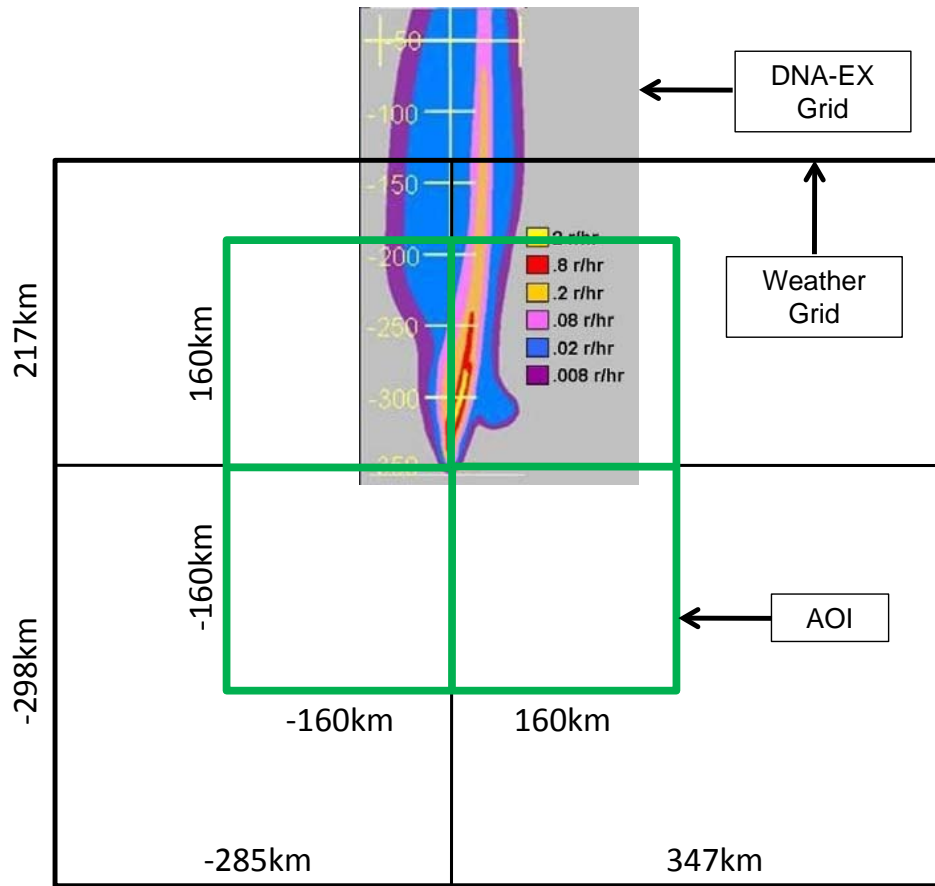


Figure 22. Spatial Relationship of the DNA-EX Dose Rate Contour Area, Reanalysis Weather Grid, and AOI

Additional Codes

Several additional codes were developed in support of this thesis. The Time_Dependent_Winds FORTRAN code was developed to convert Jones' weather reanalysis files into a format that could be used in the FDC. The Create_Output_Grid was developed to create a latitude-longitude grid that could be used in HPAC to sample dose rates at the same locations where dose rates are calculated by the FDC. The DNA_EX_Grids takes Chancellors' dose rate contour digitization data and changes it to a numerical form that can be used for MOE/NAD analysis. The MOE_NAD_ANALYSIS and MOE_NAD_ANALYSIS_HPAC programs conduct a point by point comparison of FDC and HPAC dose rates, respectively, against DNA_EX values and create MOE/NAD/FOM output files. All programs are thoroughly commented in the body of the code.

IV. Results and Analysis

This section presents the results of the research conducted. The results of the preliminary analysis are discussed, including justification for selection of the FDC over HPAC for further analysis. Subsequent analysis considers use of the FDC to determine the best-fit yield and the yield estimates associated with 10%, 25%, and 50% Error in FOM. The affects of capped and uncapped clouds on FDC dose rate contours is also discussed.

Preliminary Results

HPAC 4.04.11 and FDC dose rate contours were compared against DNA-EX dose rate contours for each test. Dose rate contours were recreated for each detonation using ground zero wind data and reanalysis weather data for a range of yields bracketing the DNA-EX recorded weapon yield. The buried shot, ESS, was also modeled even though the FDC was not written to model buried bursts. The HPAC parameters employed and the method used to create HPAC H+1hr dose rate contours are found in *Appendix J: HPAC Parameters*.

Deposition calculations were performed using the AOI grid for each shot. FOM calculations were limited to 100 miles in each cardinal direction from ground zero, except for Johnie Boy where a distance of 115km was used. The DNA-EX minimum value dose rate contour listed for each shot was used for FOM analysis. The vertical domain (altitude) was limited to the DNA-EX listed cloud top height. There were slight differences between the DNA-EX cloud top heights and the corresponding FDC values

calculated at the weapon yield, as seen in Table 4. The FDC predicted cloud top heights listed were calculated from (8) by adding the ground zero elevation and HOB, changing the reference from AGL to MSL. The most significant differences in cloud top height prediction were for Operation TEAPOT—ESS and Operation PLUMBBOB—Smoky. In these cases, the FDC predicted values were 50% and 30% higher than the observed cloud top heights, respectively. All other cloud top heights were within 10-15% of observed values. The significance of these differences is explored later.

Table 4. DNA-EX and FDC Cloud Top Heights

OPERATION: Test	DNA-EX [ft]	FDC Calculated [ft]
TUMBLER-SNAPPER: George	37000	36966
TEAPOT: ESS	12000	18429
TEAPOT: Zucchini	40000	43733
PLUMBBOB: Priscilla	43000	45787
PLUMBBOB: Smoky	38000	49117
SUNBEAM: Johnie Boy	17000	17031

An FOM comparison showed the FDC dose rate contours generally matched the DNA-EX contours more closely than HPAC 4.04.11 did for surface and surface contact bursts. HPAC did, however, outperform the FDC for the buried burst ESS. Table 5 shows the MOE_x, MOE_y, NAD, spatial Figure of Merit (FMS), and FOM for HPAC and the FDC at five yields for each shot bracketing and including the historic yield. Both HPAC and the FDC overestimated the yield of George and Johnie Boy. HPAC estimated the actual yield of ESS more closely. HPAC and the FDC performed equally well in

estimating the yield of Zucchini. The FDC estimated the yield of Priscilla and Smoky more accurately. The FOMs for HPAC, FDC capped cloud tops, and FDC uncapped cloud tops for the preliminary tests are found in *Appendix A: FOM Comparison*.

Table 5. HPAC and FDC Preliminary Results

		HPAC					FDC (Capped)				
Test	Yield	MOEx	MOEy	NAD	FMS	FOM	MOEx	MOEy	NAD	FMS	FOM
George	5	0.110	0.807	0.807	0.107	2.712	0.659	0.949	0.222	0.636	0.281
	10	0.325	0.873	0.526	0.310	0.988	0.797	0.946	0.135	0.762	0.155
	15	0.387	0.899	0.459	0.371	0.778	0.852	0.938	0.107	0.807	0.120
	20	0.435	0.974	0.399	0.430	0.613	0.882	0.929	0.095	0.827	0.105
	25	0.460	0.970	0.376	0.454	0.563	0.898	0.917	0.093	0.830	0.102
ESS	0.5	0.451	0.824	0.417	0.411	0.685	0.295	0.959	0.549	0.291	1.032
	1	0.536	0.550	0.457	0.373	0.840	0.370	0.934	0.470	0.361	0.798
	2	0.611	0.436	0.491	0.341	0.951	0.415	0.917	0.429	0.400	0.695
	5	0.725	0.437	0.455	0.374	0.809	0.464	0.902	0.387	0.442	0.598
	10	0.804	0.443	0.428	0.400	0.718	0.497	0.895	0.361	0.470	0.541
Zucchini	15	0.090	1.000	0.834	0.090	2.774	0.861	0.925	0.108	0.804	0.122
	22	0.351	0.933	0.490	0.342	0.856	0.910	0.918	0.086	0.841	0.094
	28	0.385	0.887	0.463	0.367	0.792	0.935	0.906	0.080	0.852	0.087
	40	0.345	0.819	0.515	0.320	0.969	0.955	0.880	0.084	0.844	0.092
	60	0.291	0.714	0.587	0.261	1.287	0.964	0.853	0.095	0.826	0.105
Priscilla	32	0.037	1.000	0.928	0.037	4.796	0.843	0.702	0.234	0.621	0.304
	35	0.150	1.000	0.739	0.150	1.910	0.854	0.695	0.234	0.621	0.303
	37	0.208	0.978	0.658	0.207	1.460	0.858	0.691	0.235	0.620	0.305
	45	0.664	0.861	0.250	0.600	0.330	0.871	0.680	0.236	0.618	0.307
	60	0.831	0.789	0.191	0.680	0.236	0.884	0.664	0.242	0.611	0.316
Smoky	35	0.064	0.471	0.887	0.060	5.094	0.832	0.703	0.238	0.616	0.311
	40	0.139	0.323	0.806	0.108	3.804	0.837	0.701	0.237	0.617	0.310
	44	0.248	0.333	0.716	0.166	2.491	0.842	0.699	0.236	0.618	0.308
	50	0.329	0.336	0.667	0.200	2.005	0.846	0.695	0.237	0.617	0.310
	60	0.419	0.347	0.620	0.234	1.626	0.851	0.691	0.237	0.617	0.309
Johnie Boy	0.3	0.001	0.000	0.999	0.000	1335.585	0.238	0.824	0.630	0.227	1.422
	0.5	0.001	0.000	0.999	0.000	1412.190	0.391	0.791	0.477	0.355	0.857
	1	0.001	0.000	0.999	0.000	1454.227	0.607	0.707	0.347	0.485	0.530
	2	0.001	0.000	0.999	0.000	1488.855	0.700	0.686	0.307	0.530	0.443
	5	0.002	0.001	0.999	0.000	1126.254	0.779	0.636	0.300	0.539	0.426

In the preliminary analysis, both HPAC and the FDC had a minimum FOM at the actual 28KT yield for Zucchini. Numerically, the FDC dose rate contour FOM of 0.087 was significantly better than the HPAC dose rate contour FOM of 0.792. A visual comparison of FDC, DNA-EX, and HPAC dose rate contours for Zucchini at the actual yield of 28KT, as seen in Figure 23, shows that although both correctly predicted the yield, the FDC dose rate contour provided a more accurate fit. *Appendix B: Visual Comparisons of Historic Yields* contains similar graphics for the remaining tests.

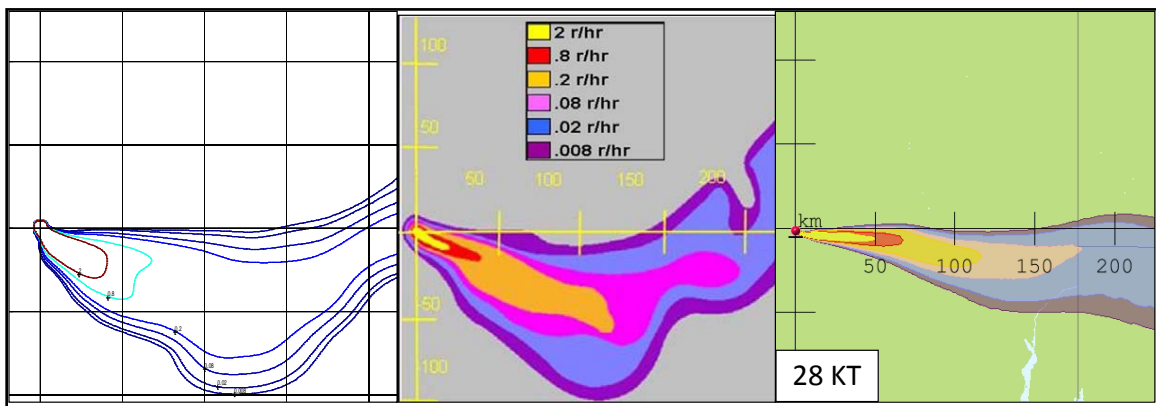


Figure 23. Operation TEAPOT—Zucchini FDC, DNA-EX, and HPAC Dose Rate Contours at 28KT

Figure 24 and Figure 25 show the respective HPAC and FDC dose rate contours for yields of 15, 22, 28, 40, and 60KT. Both modeling tools show dose rate contours do change significantly over nearly a factor of two range of yields. The graphics for the remaining tests are contained in *Appendix C: Dose Rate Contour Changes As a Function of Yield*.

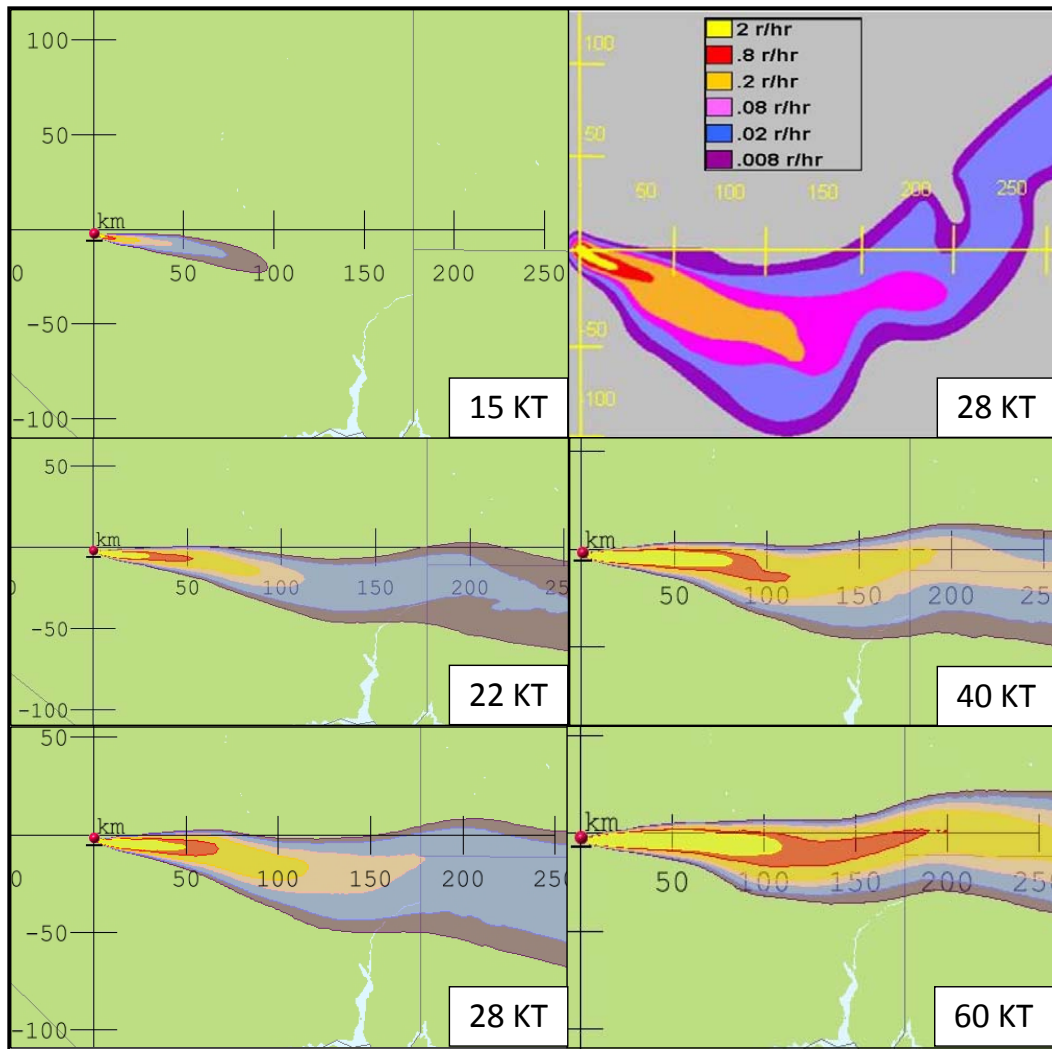


Figure 24. Operation TEAPOT—Zucchini 15, 22, 28, 40, and 60KT Yield HPAC Dose Rate Contours

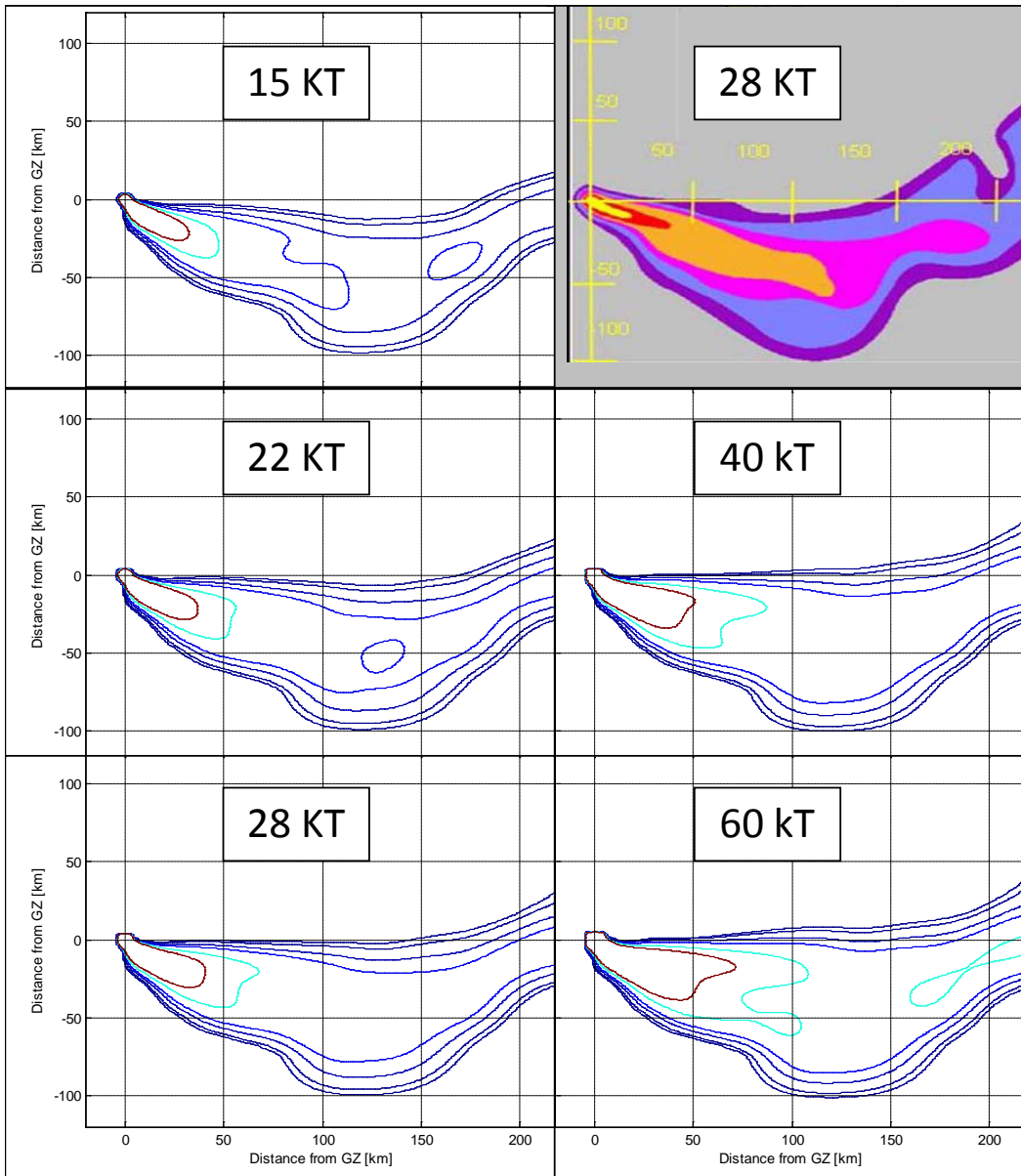


Figure 25. Operation TEAPOT—Zucchini 15, 22, 28, 40, and 60KT Yield FDC Dose Rate Contours

Based on preliminary results in which the FDC performed more accurately at yield estimation than HPAC, had generally better FOM values, and the author better understands how the FDC conducts transport and deposition, the FDC method was used for the remainder of this research.

Operation TUMBLER SNAPPER—George

George was a 15KT tower burst with a HOB of 700 feet [25:93-97]. The site elevation was measured at 4027 ft and the cloud top height was 37,000 ft. The DNA-EX contours, seen in Figure 26, show fallout deposition extended several hundred kilometers to the north and about 100 km east to west from ground zero.

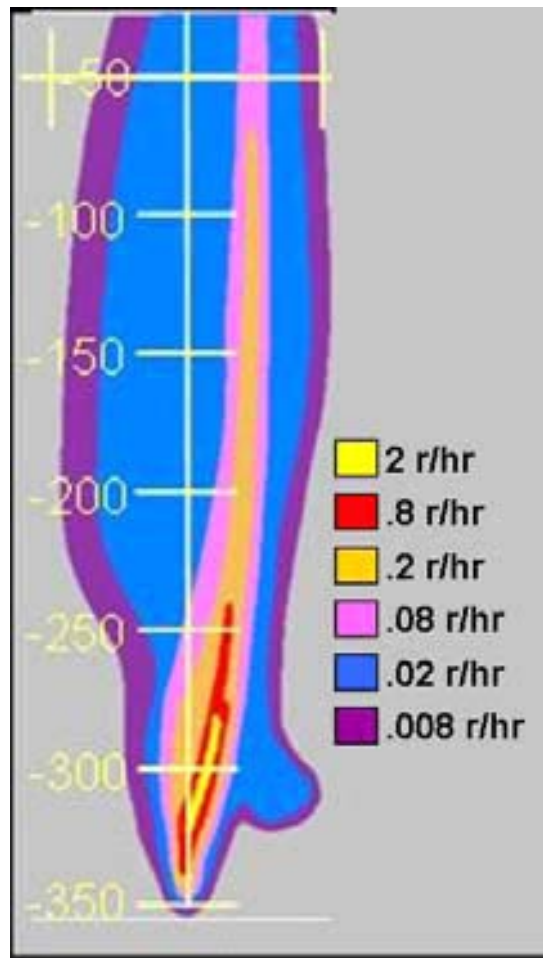


Figure 26. Operation TUMBLER-SNAPPER—George Digitized DNA-EX Contour Plot

Figure 27 contains digital imagery of the terrain surrounding George. A series of ridgelines run north to south, north of ground zero. The terrain gradually rises to over 6000 ft within 100 miles north of ground zero.



Figure 27. Operation TUMBLER-SNAPPER—George Terrain

The H-hr winds for George are generally from the south, with speeds from 20 mph at lower elevations to 50 mph at higher elevations. Wind speeds are only provided to an altitude of 30,000 ft, which is 7,000 ft below the cloud stabilization height. This research assumes the wind vector (41 mph at 190 degrees) for 30,000 ft applied at higher altitudes.

The FDC was used to produce dose rate contours from 1 to 112KT for both capped and uncapped cloud tops cases for a 200 x 200 mile spatial AOI centered on

ground zero. H-hr wind speeds were used for the first 3 hours, and wind vectors from reanalysis data thereafter.

The FDC reproduced reasonable dose rate contours for both capped and uncapped cloud tops scenarios. FOM analysis of the capped cloud top dose rate contours determined a best-fit yield of 23KT, and 10%, 25%, and 50% Error in FOM yield fits of 17KT, 13KT, and 10KT. An uncapped cloud top dose rate contour FOM analysis determined a best-fit yield of 26KT, and 10%, 25%, and 50% Error in FOM yield fits of 18KT, 14KT, and 11KT. Figure 28 shows the dose rate contours produced using capped cloud tops.

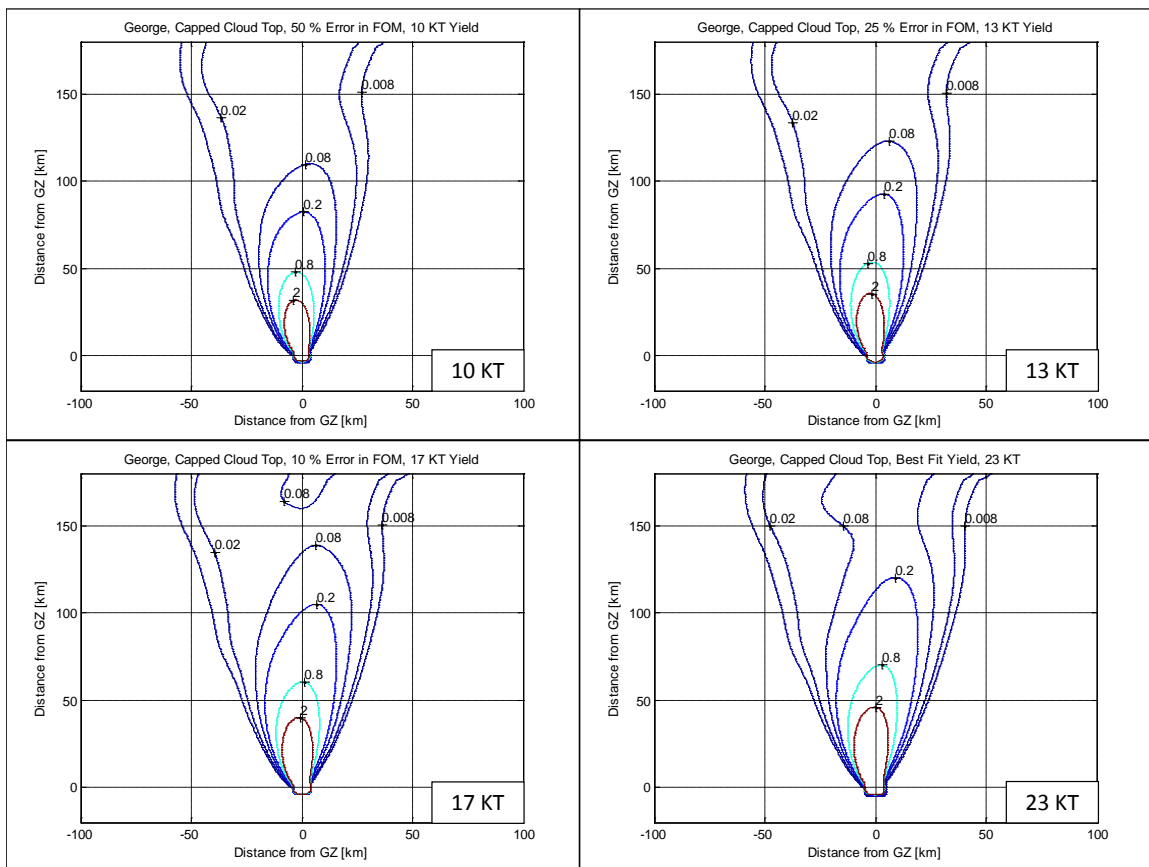


Figure 28. Operation TUMBLER-SNAPPER—George 50% (10KT), 25% (13KT), 10% (17KT) Error in FOM and Best-fit Yield (23KT) Dose Rate Contours

The FDC effectively reproduced dose rate contours for both capped and uncapped cloud top cases. Best-fit yield estimates for both cases were high but within a factor of two of actual weapon yield. The high MOE values demonstrate the DNA-EX winds and weather reanalysis data provide a reasonable estimate of winds during fallout deposition. Figure 29 shows a plot of the MOE_x and MOE_y values for both cloud top cases against NAD isolines for the range of yields. The capped and uncapped cloud top scenarios behave similarly throughout the range of yields. The MOE, NAD, FOM, and relative FOM (REL FOM) values for the capped cloud top yields are listed in *Appendix D: George FOM*.

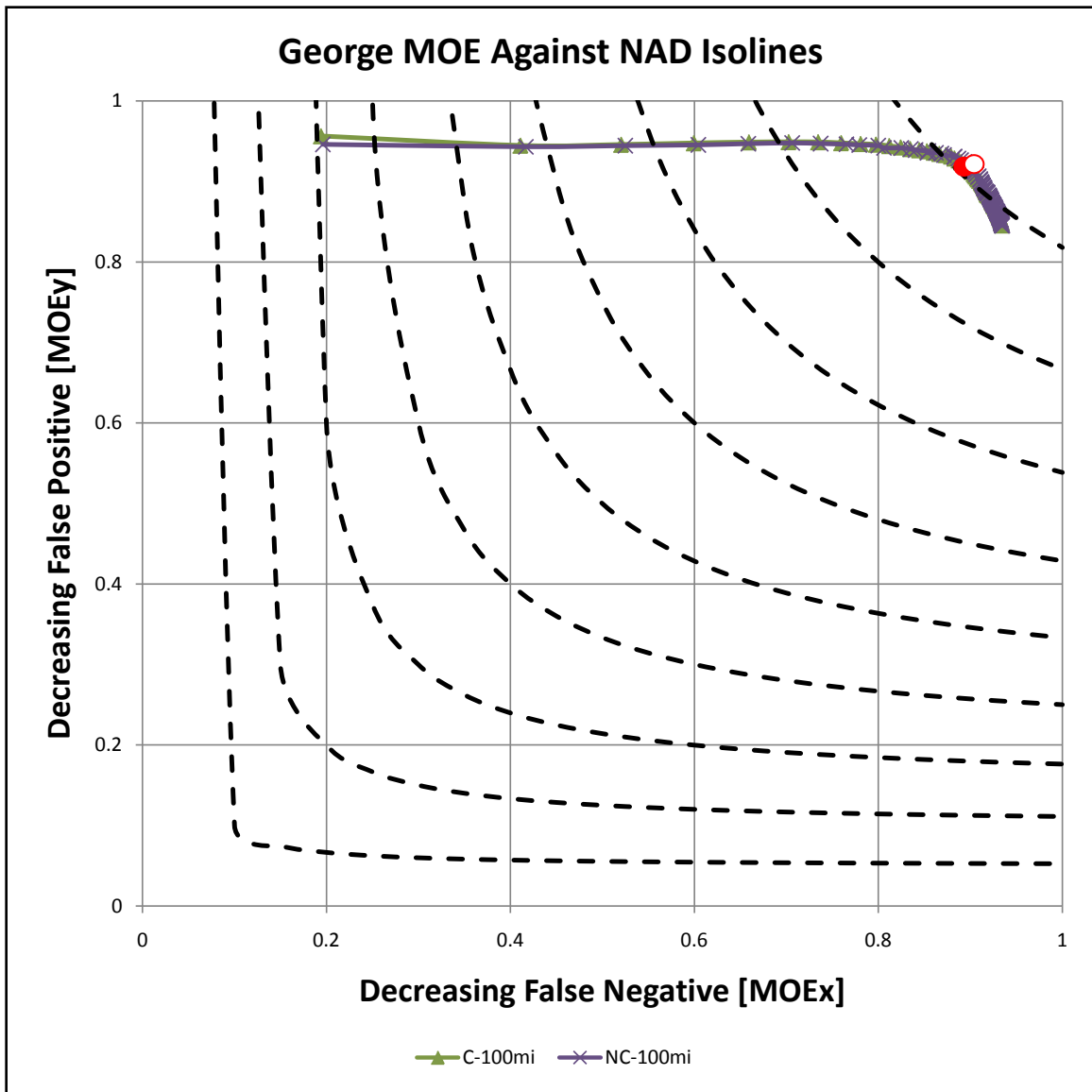


Figure 29. Operation TUMBLER-SNAPPER—George MOE-NAD Isolines

Operation TEAPOT—ESS

ESS was a 1KT burst with a DOB of 67 feet [25:201-207]. The weapon was buried in a filled shaft. The site elevation was 4288 ft and the cloud top height was 12,000 ft. The DNA-EX contours, shown in Figure 30, shows fallout deposition extended several hundred kilometers to the east. The detonation created a 292 ft diameter crater that was 96 ft deep.

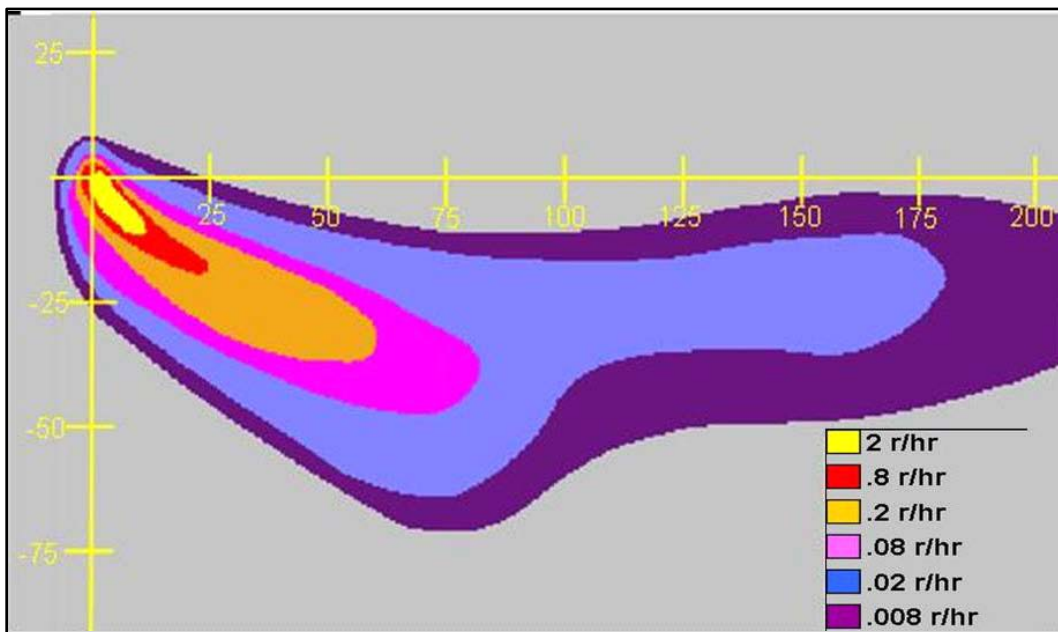


Figure 30. Operation TEAPOT—ESS Digitized DNA-EX Contour Plot

Figure 31 shows digital imagery of the terrain surrounding ESS. The terrain has numerous small ridges located to the south and east of ground zero. Southeast of ground zero, the terrain is at lower elevation than the surrounding terrain and fairly flat out to 50 miles. Thereafter, two major ridgelines run north to south.



Figure 31. Operation TEAPOT—ESS Terrain

The DNA-EX winds range from 310 to 360 degrees and 12 to 29 mph from 12,000 feet and below. These winds can lead to deposition to the southeast but not due east. The DNA-EX contours confirm that initial deposition occurred along the lower elevation area located immediately to the southeast of ground zero and continued in that direction before changing direction to due east after 75 miles. H-hr wind speeds were used for 2 hours after detonation, and reanalysis wind data was used thereafter.

The FDC was used to produce dose rate contours from 0.3 to 20KT at 0.1KT increments for both capped and uncapped cloud tops. Fallout deposition was calculated for a 200 x 200 mile AOI centered at ground zero. The FDC failed to produce a reasonable reproduction of the ESS dose rate contours. Figure 32 shows the MOE_x and MOE_y plot against NAD isolines for the capped and uncapped cases. Over the range of yields, FOM values never reached a minimum so no estimation of yield could be made.

MOE, NAD, and FOM values for ESS capped cloud top dose rate contours for the range of yields are detailed in *Appendix E: ESS FOM*.

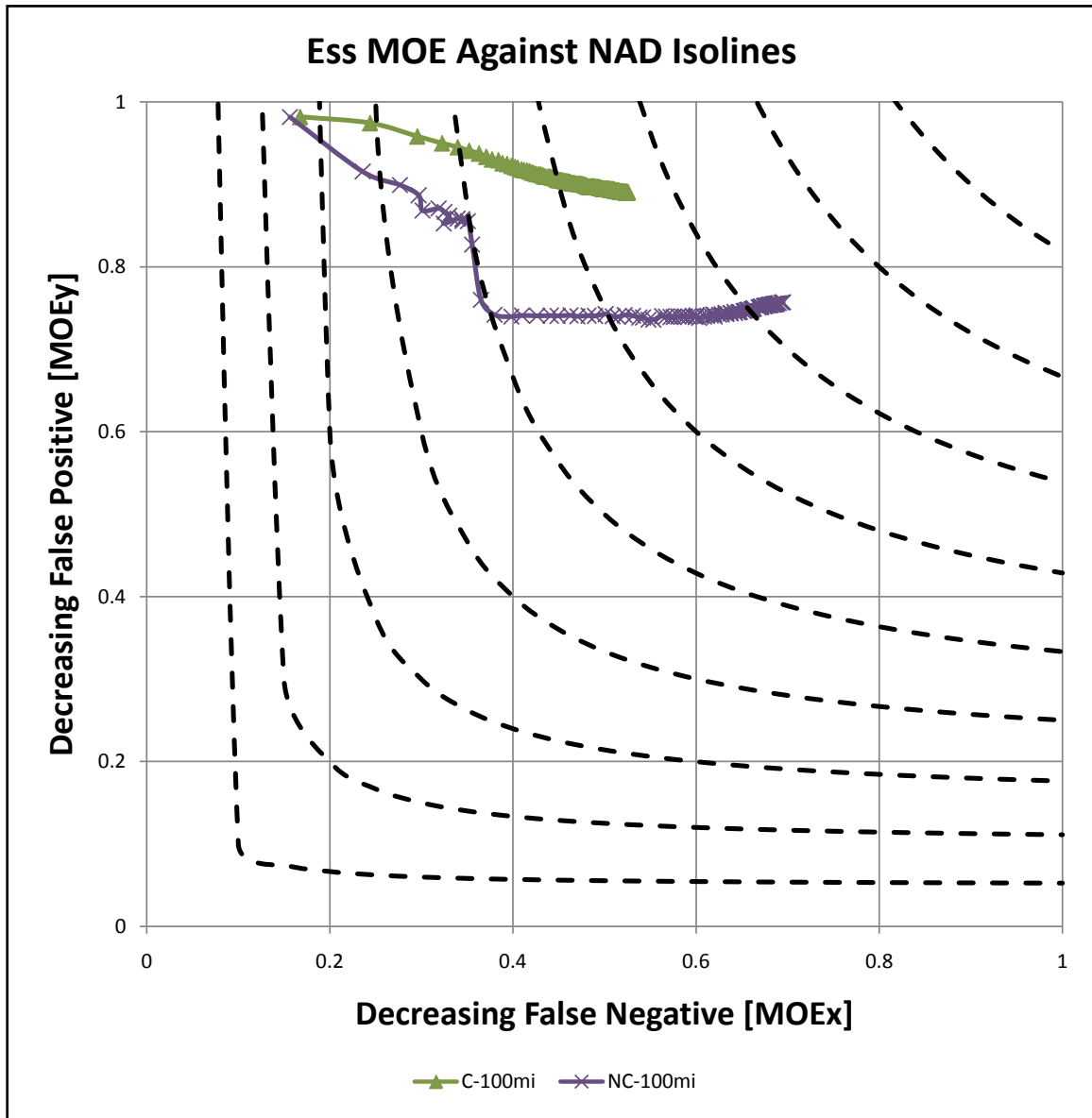


Figure 32. Operation TEAPOT—ESS MOE-NAD Isolines

The FDC failed to recreate a reasonable Operation TEAPOT—ESS dose rate contour. The FDC failed to model ESS adequately, in part, because it uses a distribution of particle size groups developed to model surface or surface contact bursts, only deposits larger particle size groups (at least 19.357 microns), and creates an initial vertical distribution of activity that cannot create a separate base surge cloud of larger particles and main radioactive cloud of much smaller particles.

Poor DNA-EX and reanalysis wind data also precluded effective modeling of ESS. However, the uncapped cloud top iterations provide interesting insights. At higher yields, these shots showed the general curvature of dose rate contours to the east as reported in the DNA-EX. The same behavior was not observed from the capped cloud tops. This behavior indicates that much of the activated debris rose significantly higher than the observed cloud top height. Uncapped cloud top dose rate contours for 5KT, 7.5KT, and 10KT yields are seen in Figure 33 through Figure 35.

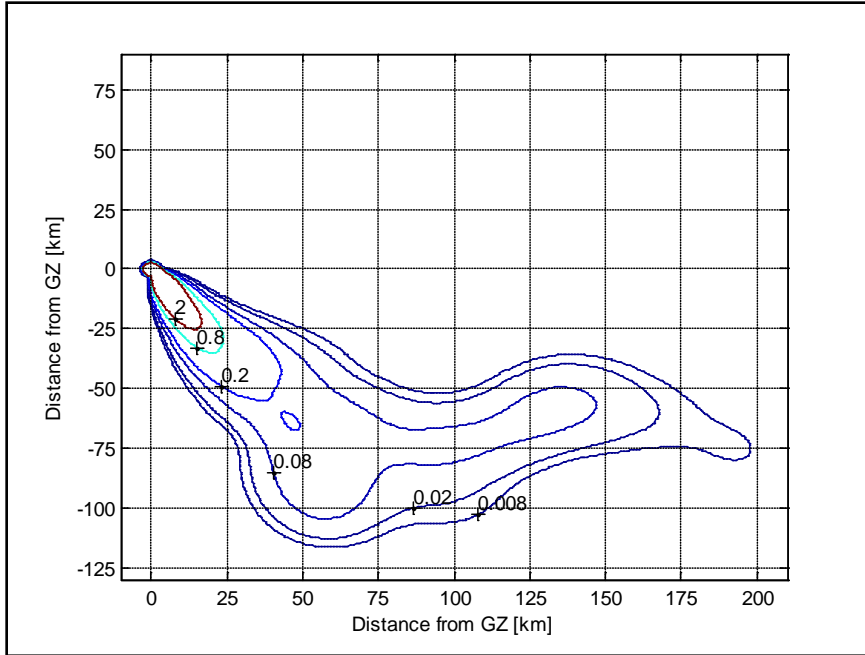


Figure 33. Operation TEAPOT—ESS (No Cap) 5KT Yield Dose Rate Contours

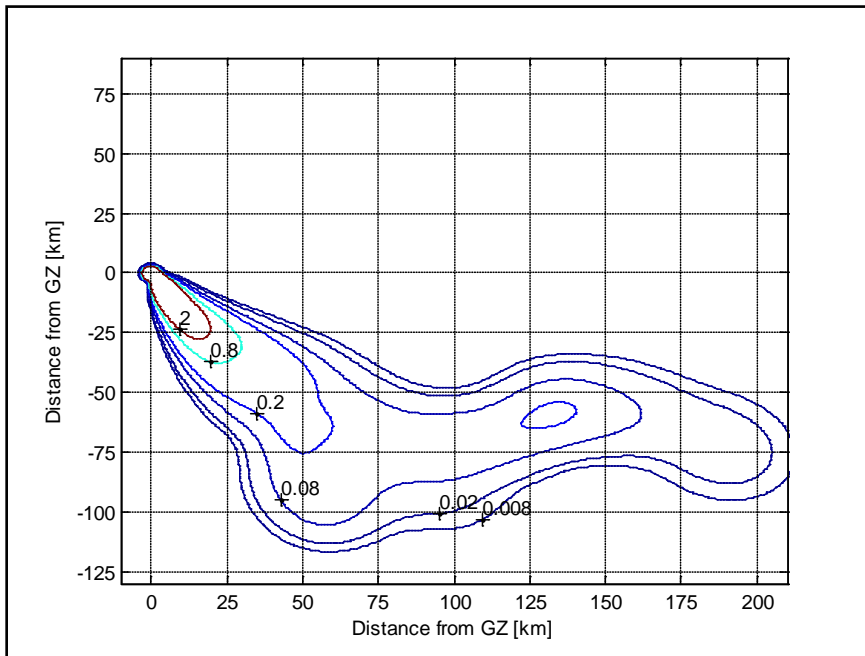


Figure 34. Operation TEAPOT—ESS (No Cap) 7.5KT Yield Dose Rate Contours

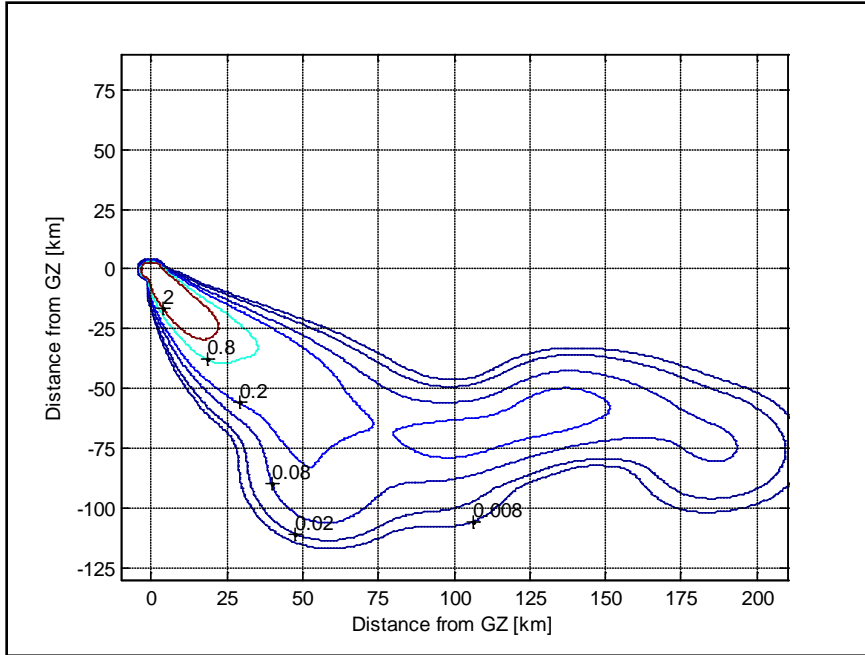


Figure 35. Operation TEAPOT—ESS (No Cap) 10KT Yield Dose Rate Contours

Operation TEAPOT—Zucchini

Zucchini was a 28KT tower burst with a HOB of 500 feet [25:240-245]. The site elevation was measured at 4245 ft and the cloud top height was measured at 40,000 ft and bottom at 25,200 ft. The DNA-EX contours, shown in Figure 36, shows fallout deposition occurred initially to the southeast and eventually to the northeast.

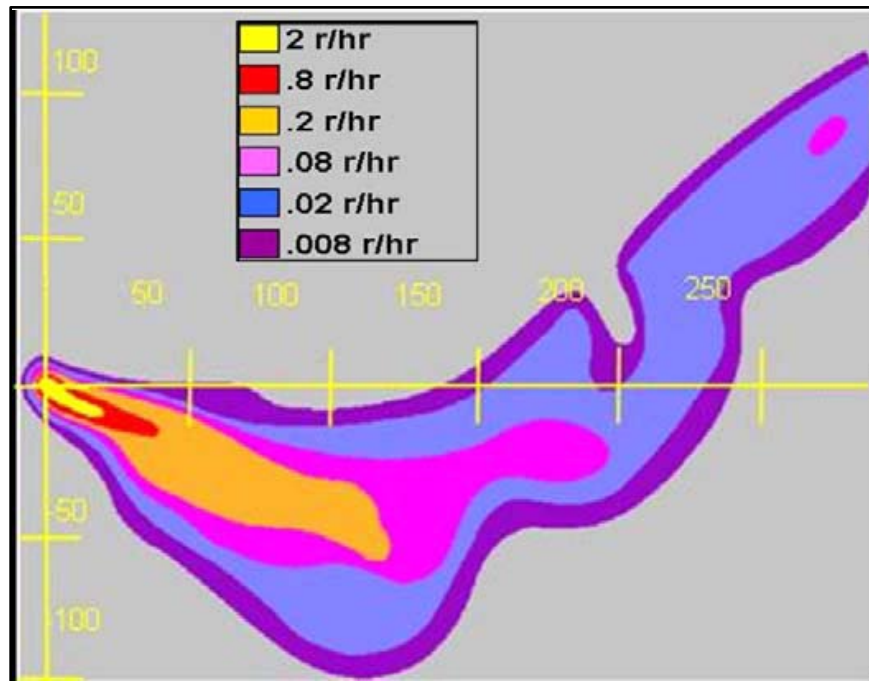


Figure 36. Operation TEAPOT—Zucchini DNA-EX Contour Plot

Figure 37 contains digital imagery of the terrain surrounding Zucchini. There are numerous southwest-northeast running ridgelines throughout the area immediately south of ground zero. A large series of north-south running ridgelines are located from 50 to 100 miles east of ground zero. The largest of the ridgelines runs directly north to south approximately 100 miles east of ground zero.

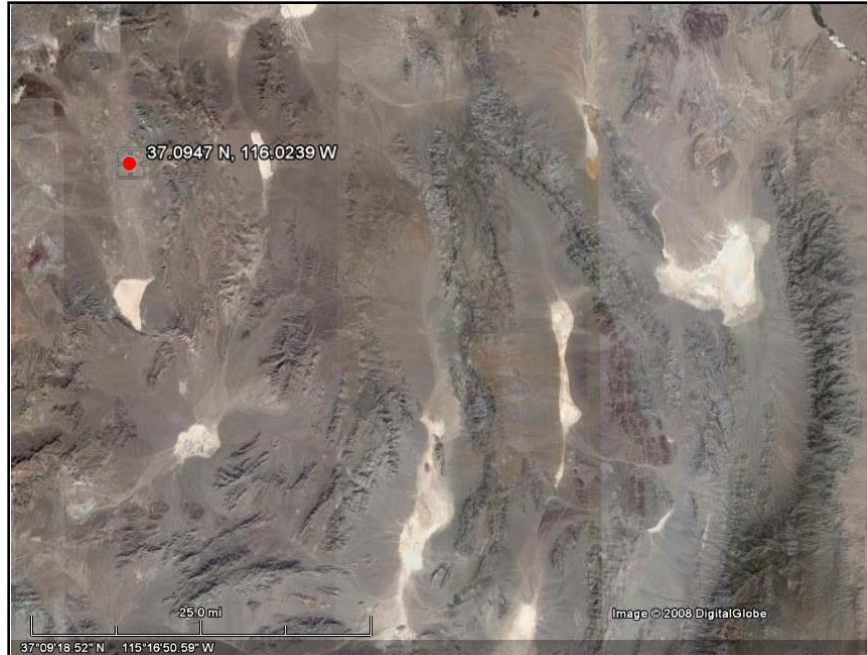


Figure 37. Operation TEAPOT—Zucchini Terrain

The DNA-EX winds provided for Zucchini are fairly uniform from the bottom to the top of the stabilized cloud, at roughly 260 to 270 degrees and 60 to 80 mph. Lower-altitude winds are generally from 300-320 degrees with speeds decreasing from 60 mph to roughly 10 mph near the surface. These winds explain why initial deposition of activity is to the southeast and eventually pushes to the northeast. H-hr wind speeds were used for the first 2 hours.

The FDC was used to produce dose rate contours from 1 to 112KT at 1KT increments for capped and uncapped scenarios for a 200 x 200 mile AOI. FOM analysis of the capped cloud top dose rate contours determined a best-fit yield of 29KT, and 10%, 25%, and 50% Error in FOM yield estimates of 22KT, 17KT, and 14KT. An uncapped cloud top dose rate contour FOM analysis determined a best-fit yield of 32KT, and 10%,

25%, and 50% Error in FOM yield fits of 22KT, 18KT, and 14KT. Figure 38 shows dose rate contours for the capped cloud top yield estimates.

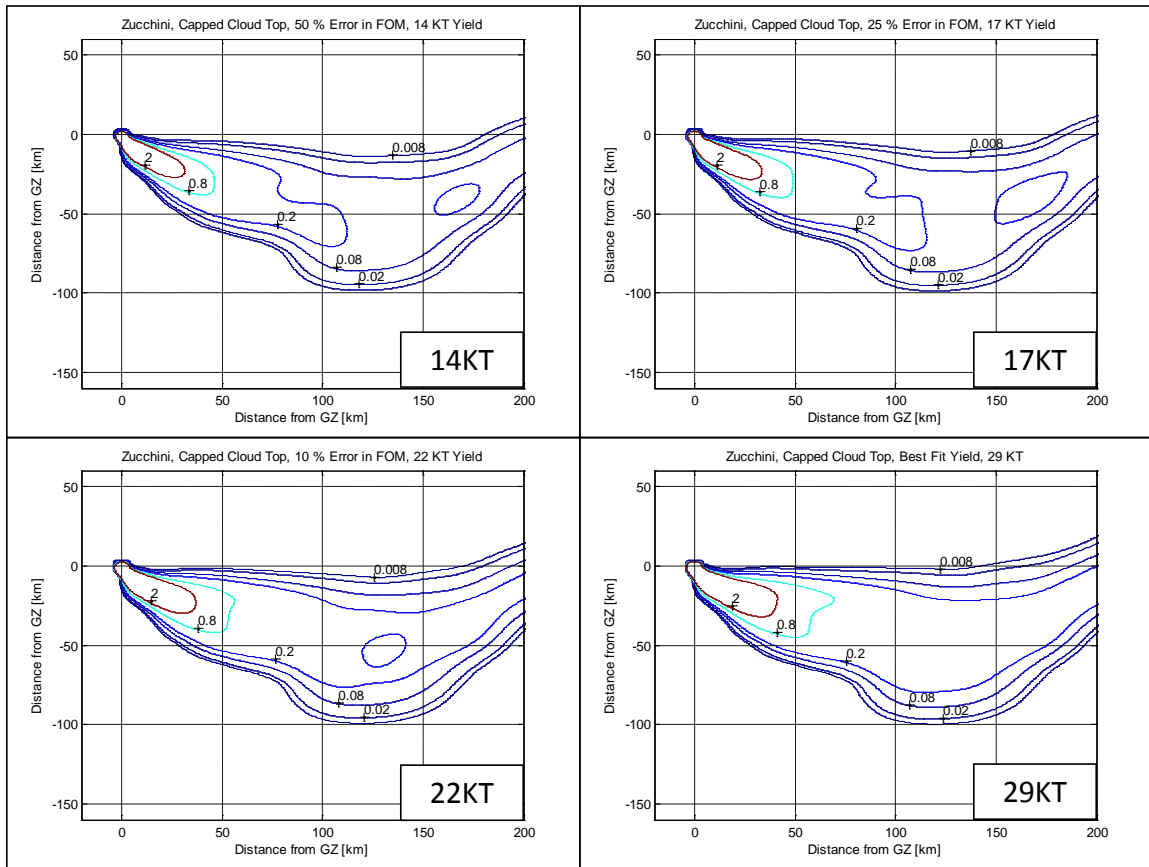


Figure 38. Operation TEAPOT—Zucchini 50% (14KT), 25% (17KT), 10% (22KT) Error in FOM and Best-fit Yield (29KT) Dose Rate Contours

The FDC recreated dose rate contours for capped and uncapped cloud top scenarios that closely matched the DNA-EX dose rate contours. Best-fit yield estimates for both capped (29KT) and uncapped (32KT) were within 15% of the actual yield (28KT). The high MOE and low NAD values indicate that the DNA-EX winds and the weather reanalysis data provide a reasonable approximation of winds during fallout deposition. Figure 39 shows a plot of the MOE_x and MOE_y values against NAD isolines for capped and uncapped clouds for the range of yields. The behavior of the curves

correlates well until the uncapped cloud tops diverge for larger yields. MOE, NAD, FOM, and REL FOM values for all Zucchini dose rate are detailed in *Appendix F*:

Zucchini FOM.

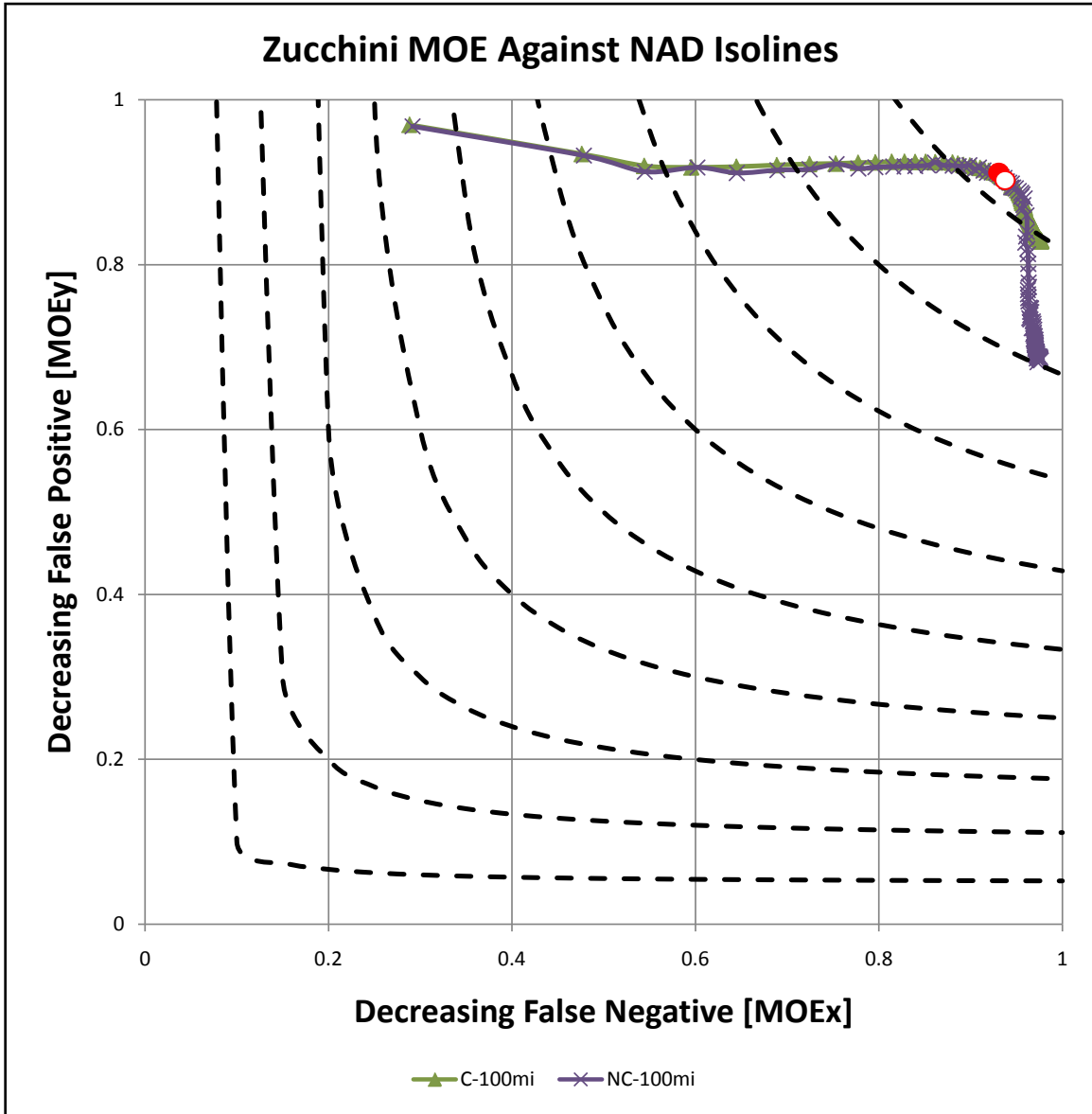


Figure 39. Operation TEAPOT—Zucchini MOE-NAD Isolines

Operation PLUMBBOB—Priscilla

Priscilla was a 37KT balloon burst with a HOB of 700 feet [25:274-278]. The site elevation was measured at 3076 ft, cloud top height at 43,000 ft, and cloud bottom height of 24,000 ft. The DNA-EX contours, seen in Figure 40, shows fallout deposition extended several hundred kilometers to the east.

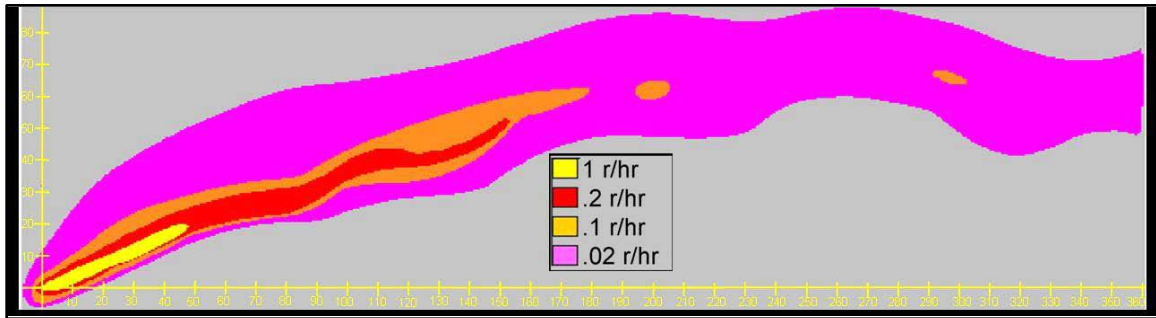


Figure 40. Operation PLUMBBOB—Priscilla DNA-EX Contour Plot

The DNA-EX winds from the cloud top to cloud bottom are generally 250 to 280 degrees with speeds from 50 mph decreasing to 8 mph as altitude decreases. Lower altitude winds are generally 240 to 210 degrees and less than 10 mph. H+1hr wind speeds were used for the first 3 hours and reanalysis wind data thereafter.

Figure 41 contains digital imagery of the terrain surrounding Priscilla. Several north-south running ridgelines are located at roughly 25 mile intervals to the east of ground zero. Higher terrain is located immediately to the south and southeast of ground zero.



Figure 41. Operation PLUMBBOB—Priscilla Terrain

Capped and uncapped cloud top FDC iterations were performed for a yield range of 1 to 112KT at 1KT increments to produce dose rate contours for a 200 x 200 mile AOI centered at ground zero. FOM analysis of the capped cloud top dose rate contours determined a best-fit yield of 36KT, and 10%, 25%, and 50% Error in FOM estimates of 27KT, 25KT, and 22KT. The uncapped cloud top analysis predicted a yield of 36KT, with 10%, 25%, and 50% Error in FOM estimates of 27KT, 25KT, and 23KT, respectively. Figure 42 shows the dose rate contours produced by the FDC under capped cloud top conditions.

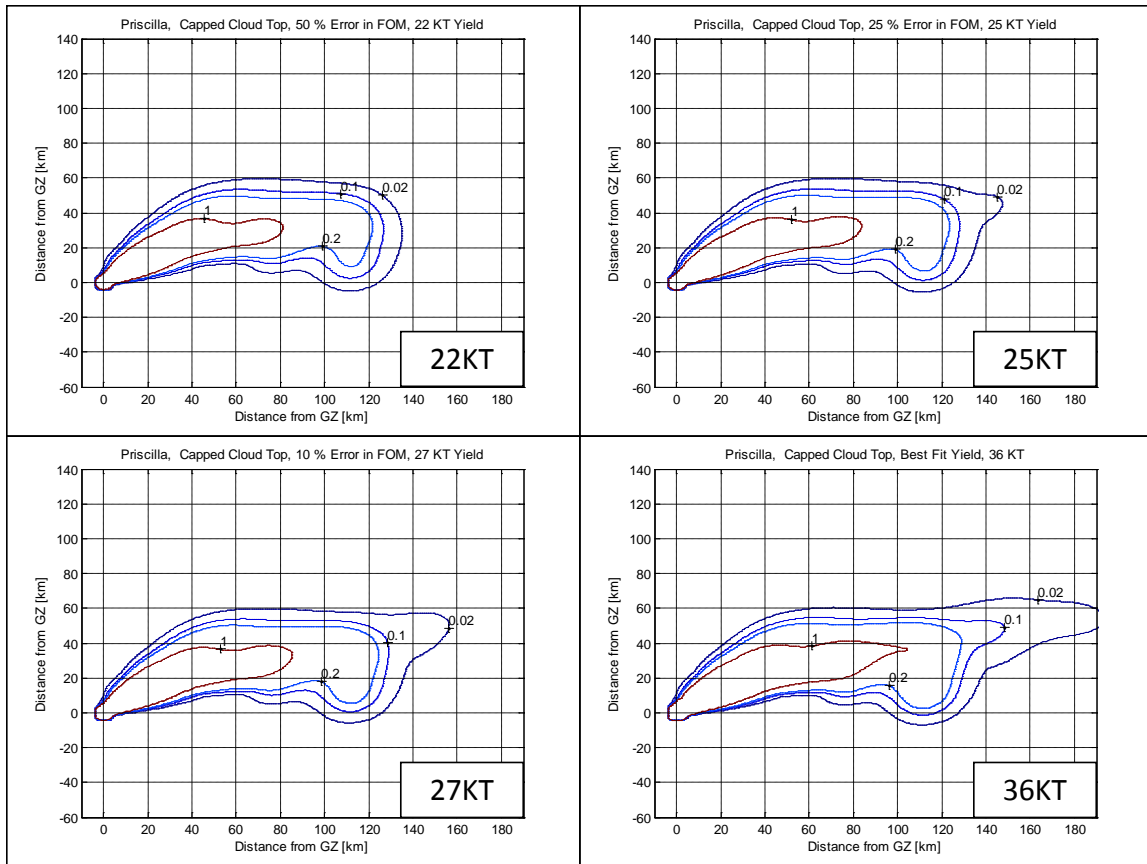


Figure 42. Operation PLUMBBOB—Priscilla 50% (22KT), 25% (25KT), 10% (27KT) Error in FOM and Best-fit Yield (36KT) Dose Rate Contours

The FDC recreated reasonable dose rate contours for Priscilla using both capped and uncapped cloud tops. The best-fit yield estimates for both methods (36KT) closely estimated the actual yield (37KT). The MOE and NAD values were reasonable indicating the DNA-EX and reanalysis weather data provided acceptable estimates of winds during fallout deposition. Figure 43 shows a plot of the MOE values with NAD isolines for capped and uncapped cloud tops over the range of yields. The behavior of the curves correlates well over the range of yields. Priscilla MOE, NAD, FOM, and REL FOM values are found in *Appendix G: Priscilla FOM*.

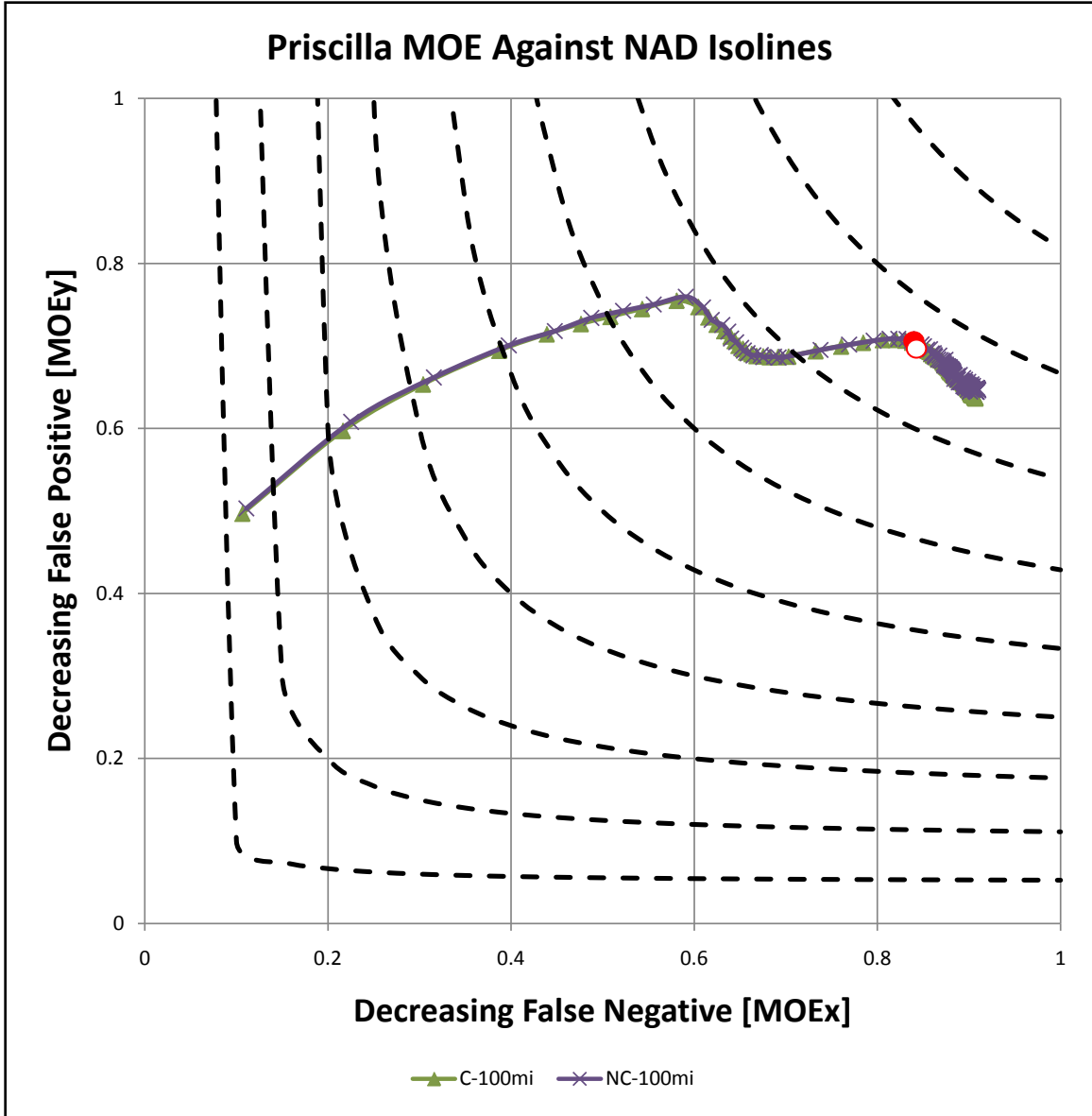


Figure 43. Operation PLUMBBOB—Priscilla MOE-NAD Isolines

Operation PLUMBBOB—Smoky

Smoky was a 44KT tower burst with a HOB of 700 feet [25:326-330]. The site elevation was measured at 4479 ft and the cloud top height was measured at 38,000 ft. The DNA-EX contours, shown in Figure 44, shows fallout deposition occurred generally east for 200 kilometers and then to the northeast.

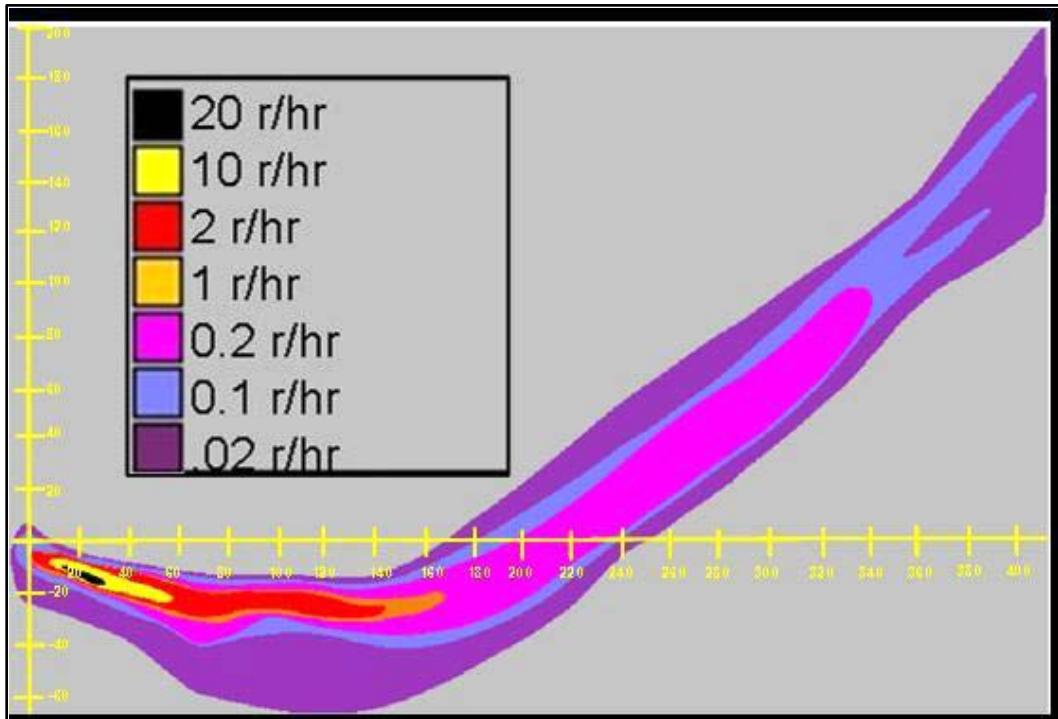


Figure 44. Operation PLUMBBOB—Smoky Digitized DNA-EX Contour Plot

The DNA-EX H-hr reported winds are generally north to south at less than 10 mph for elevations below 15,000 ft and from west to east at 30-40 mph at higher elevations. H-hr wind speeds were used for the first 4 hours. Time of use was extended beyond 3 hours because the H+3hr wind speeds were very similar to the H-hr winds.

Figure 45 contains digital imagery of the terrain surrounding Smoky. A ridgeline running northwest-to-southeast is located immediately to the southeast of ground zero. A north-to-south running valley is located immediately south of the detonation point. A series of north-to-south running ridgelines are located 50 to 80 miles east of ground zero.

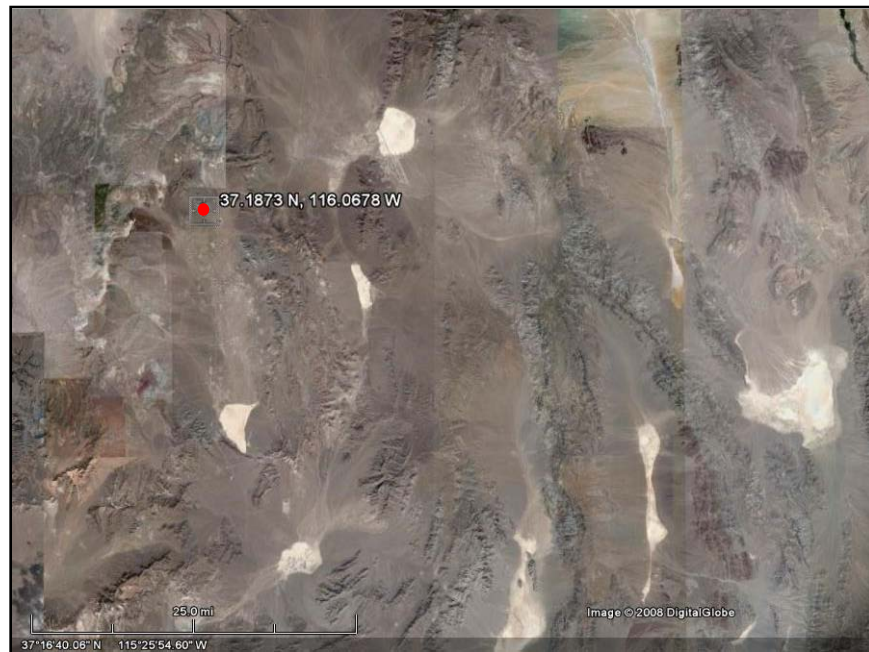


Figure 45. Operation PLUMBBOB—Smoky Terrain

The FDC was used to create capped and uncapped dose rate contours in a 200 x 200 mile spatial AOI centered on ground zero for yields from 1 to 112KT. FOM analysis of the capped cloud top dose rate contours yielded a best estimate yield of 21KT, and 10%, 25%, and 50% Error in FOM yield fits of 10KT, 8KT, and 6KT. The uncapped cloud top dose rate contours estimated a best-fit yield of 25KT and 10%, 25%, and 50% Error in FOM estimates of 10KT, 7KT, and 6KT. Figure 46 shows the capped cloud top dose rate contours.

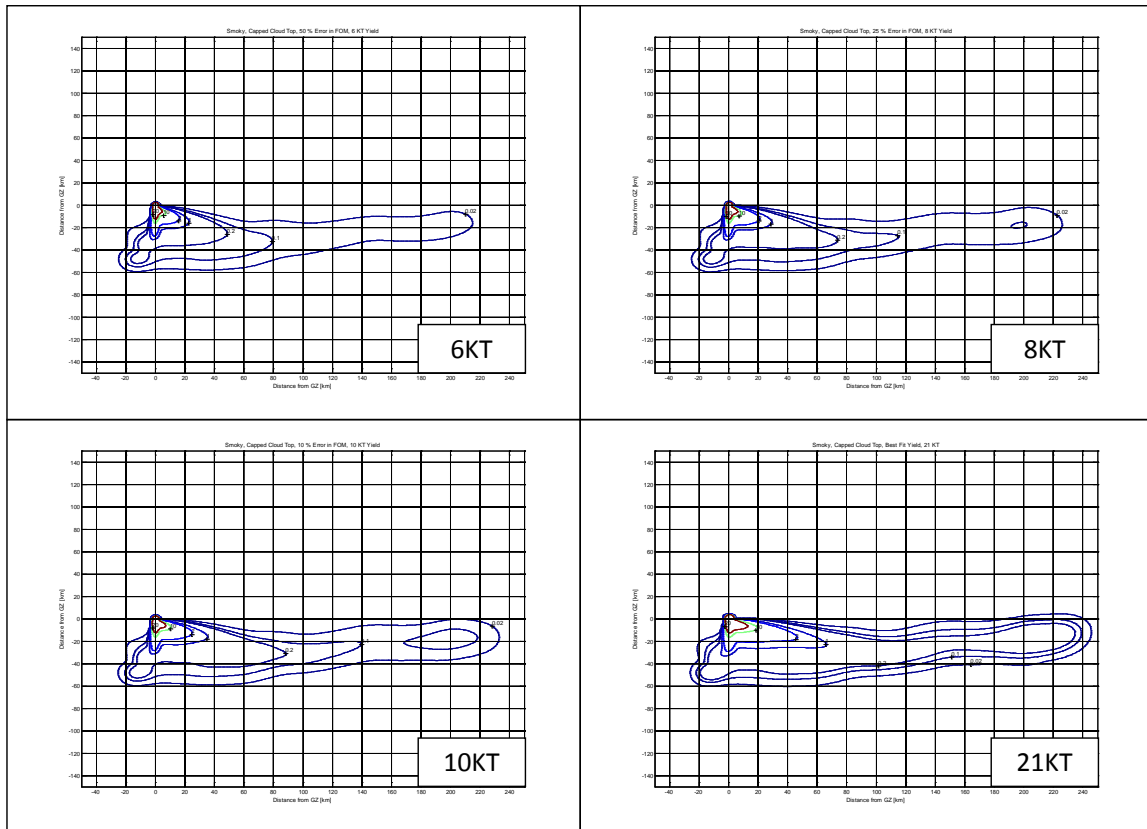


Figure 46. Operation PLUMBBOB—Smoky 50% (6KT), 25% (8KT), 10% (10KT) Error in FOM and Best-fit Yield (21KT) Dose Rate Contours

The FDC recreated reasonable dose rate contours for both capped and uncapped cloud top cases. Best-fit yield estimates for both cases were low at roughly half of the actual weapon yield. The MOE values demonstrate the DNA-EX winds and weather reanalysis data provide a reasonable estimate of winds during fallout deposition. Figure 47 shows the MOE-NAD isoline plot for the range of yields for both capped and uncapped cloud top conditions. MOE, NAD, FOM, and REL FOM values for Smoky dose rate contours for yields from 1 to 112KT are found in *Appendix H: Smoky FOM*.

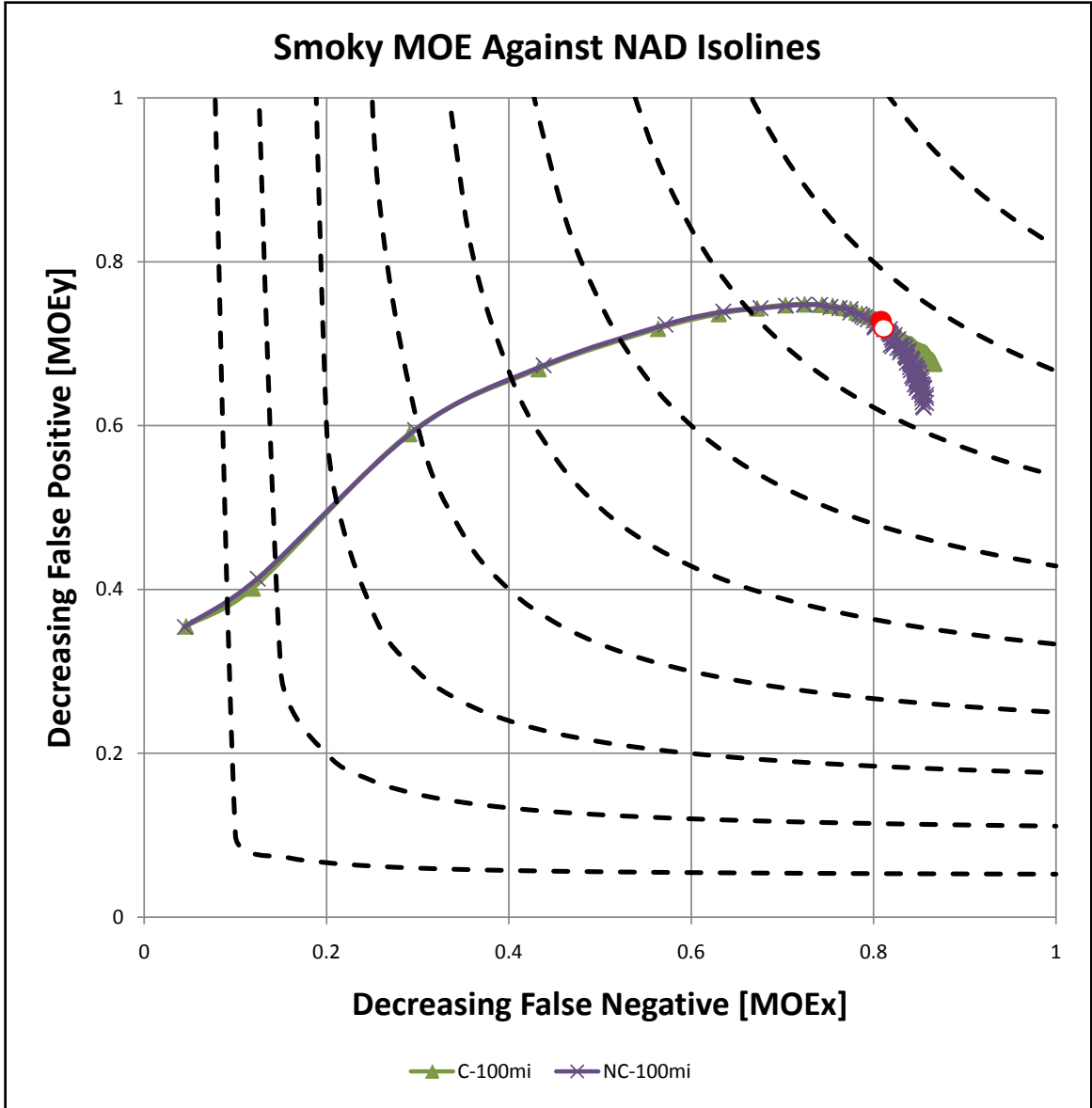


Figure 47. Operation PLUMBBOB—Smoky MOE-NAD Isolines

Operation SUNBEAM—Johnie Boy

Johnie Boy was a 0.5KT shallow buried burst with a DOB of 2 feet [25:563-567]. The site elevation was measured at 5153 ft, cloud top height at 17,000 ft, and cloud bottom height at 12,500 ft. The DNA-EX contours, shown in Figure 48, shows fallout deposition occurred generally to the north to approximately 115 km. The blast created a 122 ft diameter crater 30 ft in depth.

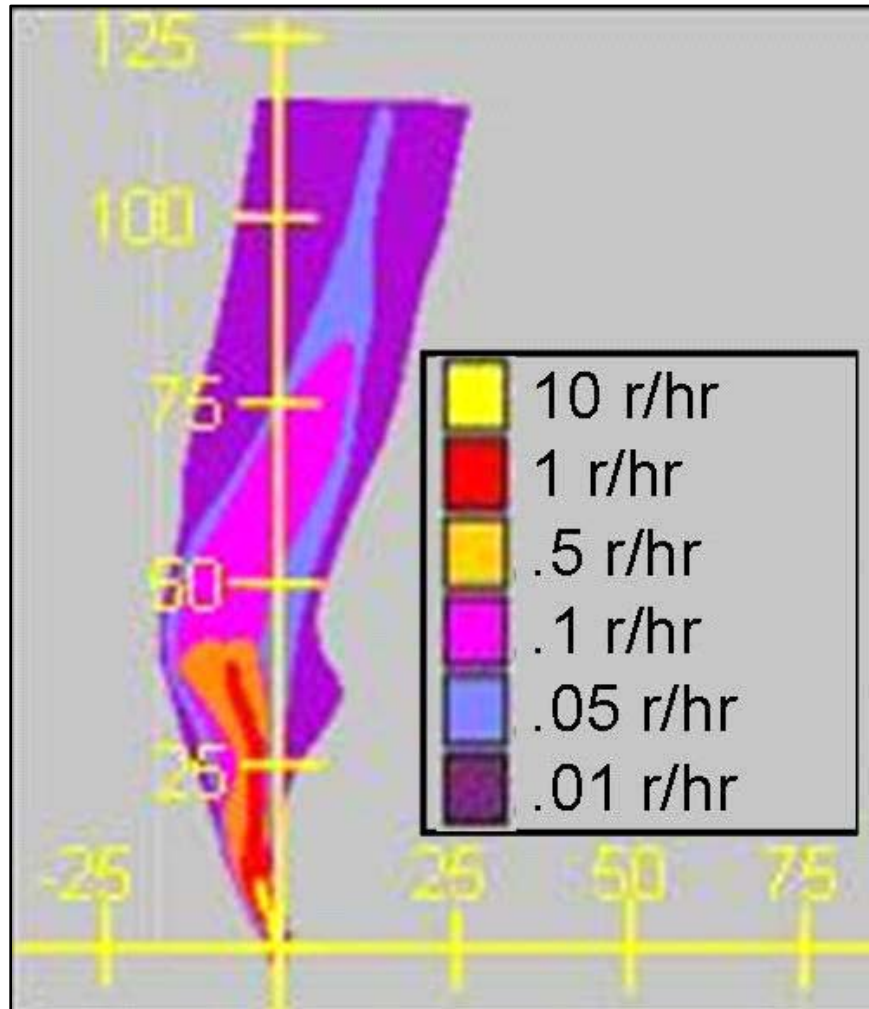


Figure 48. Operation SUNBEAM—Johnie Boy Digitized DNA-EX Contour Plot

The DNA-EX winds for Johnie Boy are generally 30 mph from the southwest above 14,000 ft, 15 mph and from the south from 10,000 to 14,000 ft, and 10 mph from the southeast at lower elevations. H-hr wind speeds were used for the first 3 hours.

Figure 49 contains digital imagery of the terrain surrounding Johnie Boy. The area immediately around ground zero is part of an area of higher elevation with irregular ridgelines. About 25 miles north-northeast of ground zero is an area of lower elevation that runs south to north.



Figure 49. Operation SUNBEAM—Johnie Boy Terrain

For a 144 x 144 mile spatial grid, the FDC was used to produce dose rate contours from 0.3 to 10KT at 0.1KT increments for capped and uncapped cloud top conditions. Capped cloud top dose rate contour FOM analysis determined a best-fit yield of 3.5KT, and 10%, 25%, and 50% Error in FOM estimates of 1.6KT, 1.0KT, and 0.7KT. An uncapped cloud top dose rate contour FOM analysis estimated the yield at 1.5KT, and 10%, 25%, and 50% Error in FOM estimates of 0.8KT, 0.6KT, and 0.5KT. Figure 50 shows the capped cloud top dose rate contours.

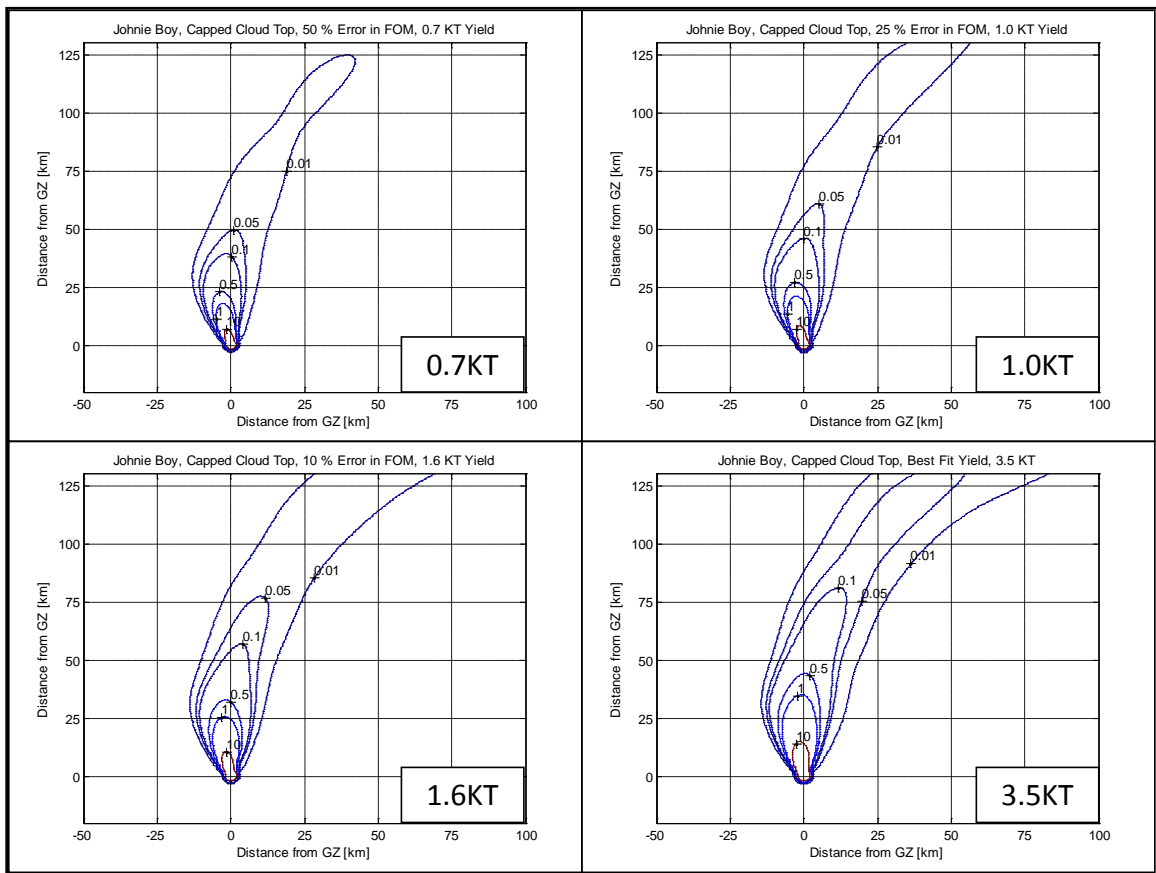


Figure 50. Operation SUNBEAM—Johnie Boy 50% (0.7KT), 25% (1.0KT), 10% (1.6KT) Error in FOM and Best-fit Yield (3.5KT) Dose Rate Contours

The FDC produced reasonable dose rate contours for both capped and uncapped cloud top cases. The best-fit yield estimates for the capped (3.5KT) and uncapped (1.5KT) cases were significantly higher than the actual yield (0.5KT). MOE values indicate that the DNA-EX winds and weather reanalysis data provide a reasonable estimate of winds during fallout deposition. It is important to note that the particle size distribution for Johnie Boy likely falls somewhere between the FDC calculated distribution and one that would be more suitable for a buried burst. Figure 51 shows the capped and uncapped cloud top MOE-NAD isolines graph for the range of yields. The MOE, NAD, FOM, and REL FOM values for Johnie Boy dose rate contours are included in *Appendix I: Johnie Boy FOM*.

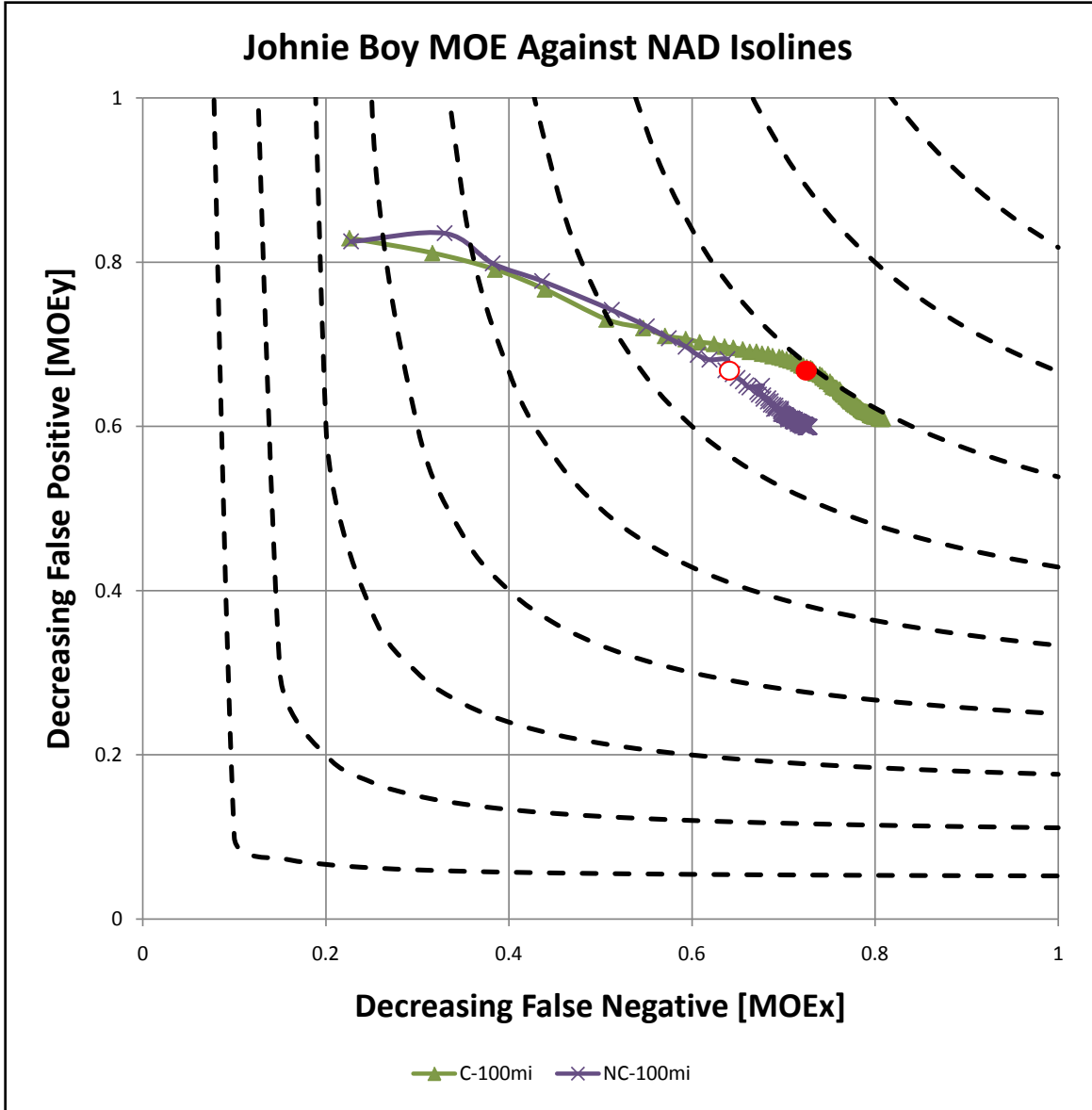


Figure 51. Operation SUNBEAM—Johnie Boy MOE-NAD Isolines

Capped and Uncapped Yield Estimation Results

The capped and uncapped FDC iterations produced comparable best fit yield estimates close to the historic yield for five of the six tests considered. The lone exception was Operation TEAPOT—ESS. The FDC failed to model this detonation well enough to determine a best fit yield estimate for either capped or uncapped cloud top conditions.

Table 6 lists the best-fit and Error in FOM yield estimates for capped and uncapped cloud top cases for the five remaining tests. Yield estimates were not interpolated between data points. The lower yield value was taken when the acceptable Error in FOM value fell between yields.

Table 6. Capped and Uncapped Cloud Height Yield Predictions

Shot	Yield [KT]	Capped Cloud Top				Uncapped Cloud Top			
		Best Fit Yield [KT]	10% FOM Error [KT]	25% FOM Error [KT]	50% FOM Error [KT]	Best Fit Yield [KT]	10% FOM Error [KT]	25% FOM Error [KT]	50% FOM Error [KT]
Tumbler Snapper: George	15	23	17	13	10	26	18	14	11
Teapot: Zucchini	28	29	22	17	14	32	22	18	14
Plumbbob: Priscilla	37	36	27	25	22	36	27	25	23
Plumbbob: Smoky	44	21	10	8	6	25	10	7	6
SUNBEAM: Johnie Boy	0.5	3.5	1.6	1.0	0.7	1.5	0.8	0.6	0.5

A statistical analysis of the best-fit yield estimates determined, with 90% confidence, the actual yield falls within a factor of 0.46 of the predicted yield for the capped cloud top case and within a factor of 0.30 for the uncapped cloud top case. The 10%, 25%, and 50% Error in FOM predictions provide estimates of how uncertainty in dose rate recreation affects yield estimates. The 90% confidence interval for both capped and uncapped cloud tops was a factor of 1.3 for a 10% Error in FOM estimate; 1.7 and 2.1, respectively, for 25% Error in FOM; and a factor of 2.5 for 50% Error in FOM. Given the small sample size, uncertainty in weather data, uncertainty of modeling parameters (such as source normalization constant, cloud rise, and particle size distribution), and dose rate measurements, this method may be used to realistically estimate yield to within a factor of two. Details of the statistical analysis performed on the yield estimates are included in *Appendix K: Statistical Analysis*.

Validity of Weather Data

Figure 52 provides insight into the employment of the FDC to recreate dose rate contours and weather data validity. The graph shows, from right to left, the 50%, 25%, and 10% Error in FOM and best-fit yield estimates for each surface contact burst. The location of the estimates for George and Zucchini at the top right of the graph demonstrate that the combination of ground zero and reanalysis weather winds provide an excellent recreation of the winds during fallout deposition. The wind data associated with the remaining three shots all provided reasonable estimates, allowing fair reproductions of the associated DNA-EX dose rate contours. The use of ground zero and

high resolution mesoscale reanalysis weather data winds within 100 miles of ground zero has been validated.

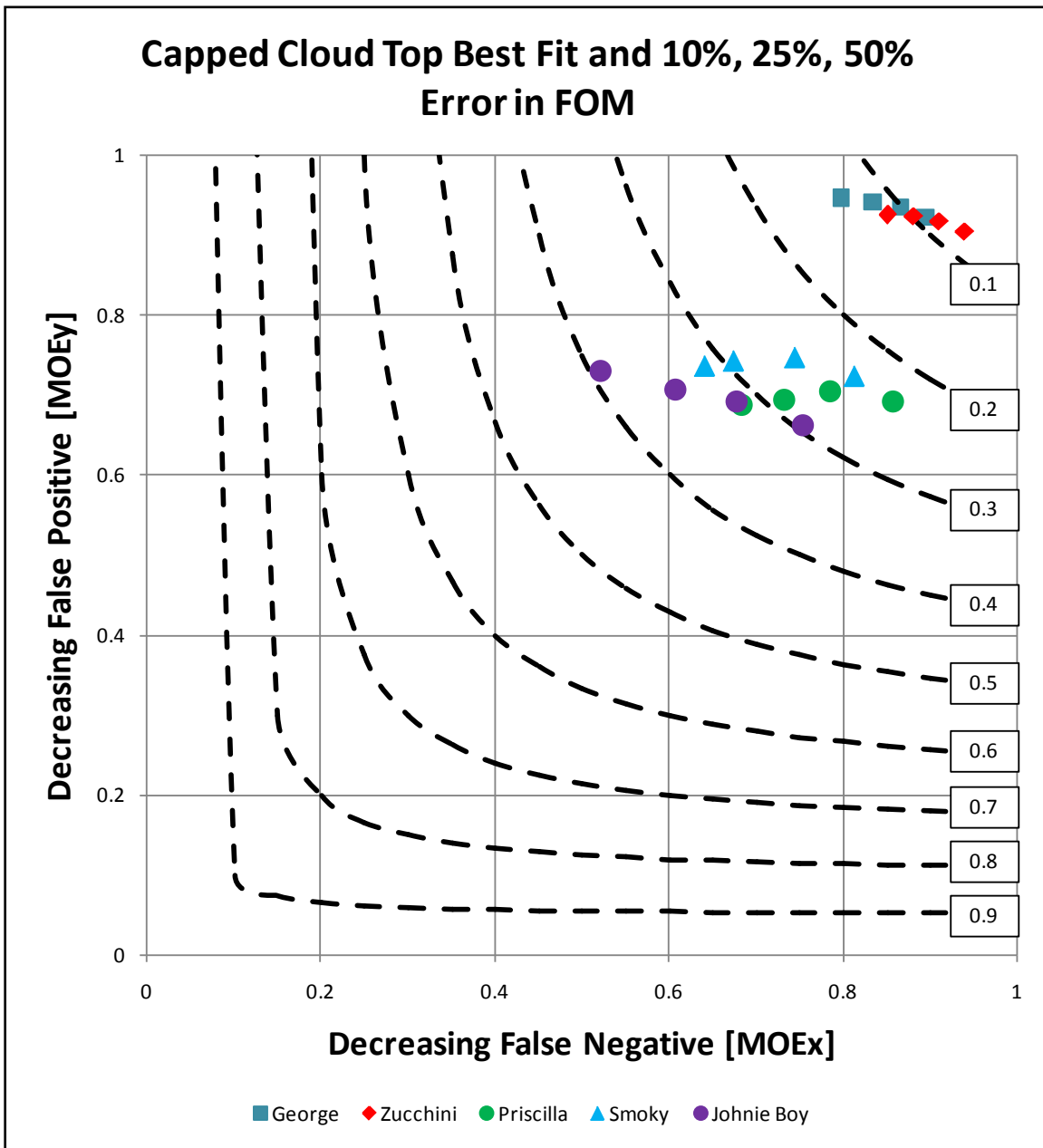


Figure 52. Best-fit and Error in FOM MOE-NAD Isolines

Sources of Error

Measurement, sampling, and modeling errors all contribute to differences between FDC and DNA-EX contours. All activity measurements were adjusted to H+1 hr dose rates using the Way-Wigner approximation. Post-test dose rates were measured when activity levels permitted. Generally, more measurements were taken close to ground zero to allow establishment of a more detailed on-site grid. Those readings of most interest to the establishment of off-site dose rate contours were taken using ground mobile monitors. These ground mobile monitors were used to take activity measurements over a large area in the hours and days following each test. In most cases, the dose rate contours were taken over areas that were tens of thousands of square miles. Producing an accurate dose rate contour over such a large area was certainly a difficult task. For example, George's fallout footprint covered an area of over 12,000 square miles, so more than 31,000 dose rate measurements would be required to construct contours for a uniform grid with 1 km fidelity. The sampling plans after these tests were nowhere near that detailed.

The FDC, like HPAC 4.04.011, neglects the affects of winds during cloud rise. The FDC starts with a stabilized cloud horizontally centered above ground zero. The model fails to account for winds during cloud rise and the location of the cloud upon stabilization. These differences are likely part of the reason that the FDC and DNA-EX dose rate contours differ somewhat near ground zero.

The FDC initial stabilized cloud top and bottom heights were constructed using Hopkins' numerical fits with Conners' numerical fit for the standard deviation to DELFIC CRM outputs. As Jodoin pointed out, the DELFIC CRM underestimates the

height at which larger particles stabilize within the cloud and affects the dose rate contours [5:117-118]. Thus, the error in these numerical fits affected the vertical distribution of activity within the stabilized cloud, most significantly for the largest particle groups, and the corresponding FDC dose rate contours.

Several other modeling assumptions affected the ability of the FDC to recreate DNA-EX dose rate contours. The most significant of these assumptions included use of a single particle distribution for all cases, use of a single-source normalization constant for all shots, and no vertical winds. Particle size distributions certainly varied between shots; therefore, adjustment to the parameters used to define the distribution would change the particle size groups and the contours produced. Any change to the source normalization constant would have changed the dose rates calculated for each grid point and the associated dose rate contours. The simplifying assumption of no vertical winds ignores downdrafts and updrafts that could lead, respectively, to quicker and slower fallout deposition than would otherwise occur.

V. Conclusions and Recommendations

Conclusions

The major accomplishments of this research are that it provides a proof of concept for yield estimation from inversion of dose rate contours, validates the use of ground-zero and high resolution mesoscale reanalysis weather wind data to recreate DNA-EX dose rate contours, develops a single numerical FOM to compare a series of dose rate contours against a reference dose rate contour, and creates a relatively simple fallout deposition code that accounts for time and spatially variable winds.

The Yield Estimation / Yield Approximation (YEYA) inversion technique is reliable to within a factor of two with more than 90% confidence. It is important to note that the dose rate inversion yield estimation technique is not practical for yield diagnosis immediately after a domestic nuclear event. Application of this technique requires a very detailed knowledge of, among other things, dose rate contours that would not be available without substantial effort.

This study determined that a combination of ground zero balloon wind data and reanalysis weather wind data allowed recreation of dose rate contours that more closely matched DNA-EX contours than previous modeling efforts. Further, this research improved on the MOE and NAD analysis techniques by creating the FOM to provide a single numerical quantity to compare a series of predicted dose rate contours against a reference dose rate contour. Finally, the similarities between yield bracketing for the capped and uncapped cloud scenarios indicate that the numerical fits to DELFIC used to create the initial stabilized clouds reasonably described the aggregate vertical distribution

of the 19.357 micron and larger particle groups that were studied. The consistency in yield estimates between capped and uncapped clouds demonstrates that the vertical distribution of activity within the cloud is reasonable. This highlights that a relatively minor modification to HPAC—proper integration of the DELFIC CRM—will dramatically improve HPAC’s predictive capability.

Recommendations for Future Work

There are numerous possible follow-on projects to the work conducted in this thesis. Given the success of the FDC, there are several potential modifications that might improve the model. Some of the major modifications include creation of refined numerical fits to cloud tops, cloud bottoms, and cloud diameter by particle size group using Jodoin’s modified DELFIC; incorporation of winds during cloud rise and prior to stabilization; inclusion of vertical winds; and inclusion of more detailed terrain. Modification of the particle size distribution to separately account for deeply buried, shallow buried, surface, and surface contact bursts would also be useful.

The current dose rate contour inversion technique may be applied to study yield prediction capability for dose rate contours that are closed within the DNA-EX. The FDC may be employed and the inversion technique repeated for DNA-EX on-site dose rate contours using ground zero wind data.

The FDC may be used in its current form, or after slight input-output modifications, to allow study of several other nuclear forensics topics. Two possible areas of research include yield estimation from integration of dose rate contours and yield estimation from dose rate(s) at a point(s). The former seeks to integrate dose rate

contours to determine the total activity deposited and relate it to weapon yield. The FDC output files can be used to create a first approximation. In the latter, using simple unidirectional winds, it may be possible to relate dose rates at points downwind to the weapon yield and time. For example, the H+1 hr dose rates for a 10KT burst at 25km and 50km directly downwind from a 10mph may be established, or the values for 10KT, 25KT, and 50KT bursts may be compared at these locations.

Use of Kriging to perform a statistically sound reproduction of the post-test dose rate contours and comparing them to DNA-EX and other dose rate reproductions may be useful. Although the data is sparse, a researcher may be able to go to original historical sources and obtain data that would provide more resolution to the actual dose rate contours produced by nuclear tests.

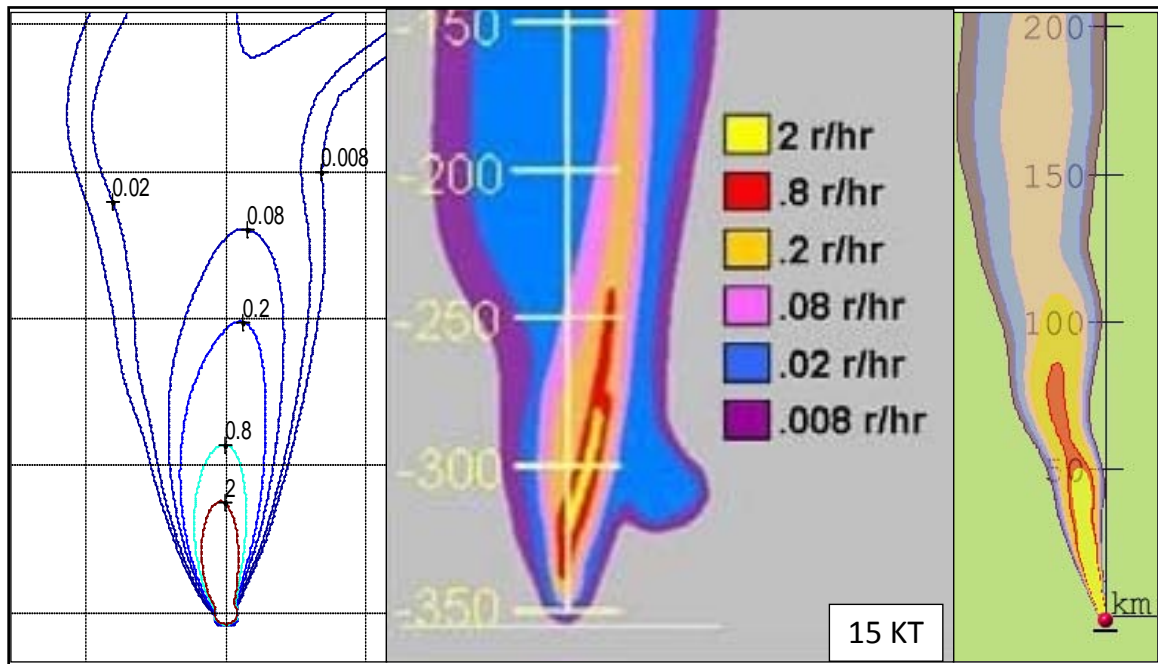
Appendix A: FOM Comparison

Test	Yield	HPAC					FDC (Capped)					FDC (Uncapped)				
		MOEx	MOEy	NAD	FMS	FOM	MOEx	MOEy	NAD	FMS	FOM	MOEx	MOEy	NAD	FMS	FOM
George	5	0.110	0.807	0.807	0.107	2.712	0.659	0.949	0.222	0.636	0.281	0.659	0.947	0.223	0.635	0.283
	10	0.325	0.873	0.526	0.310	0.988	0.797	0.946	0.135	0.762	0.155	0.800	0.945	0.134	0.764	0.154
	15	0.387	0.899	0.459	0.371	0.778	0.852	0.938	0.107	0.807	0.120	0.854	0.938	0.106	0.808	0.118
	20	0.435	0.974	0.399	0.430	0.613	0.882	0.929	0.095	0.827	0.105	0.883	0.931	0.094	0.829	0.103
Ess	25	0.460	0.970	0.376	0.454	0.563	0.898	0.917	0.093	0.830	0.102	0.896	0.922	0.091	0.833	0.100
	0.5	0.451	0.824	0.417	0.411	0.685	0.295	0.959	0.549	0.291	1.032	0.277	0.899	0.577	0.268	1.157
	1	0.536	0.550	0.457	0.373	0.840	0.370	0.934	0.470	0.361	0.798	0.330	0.862	0.522	0.314	0.979
	2	0.611	0.436	0.491	0.341	0.951	0.415	0.917	0.429	0.400	0.695	0.410	0.741	0.472	0.358	0.857
	5	0.725	0.437	0.455	0.374	0.809	0.464	0.902	0.387	0.442	0.598	0.609	0.740	0.332	0.501	0.495
Zucchini	10	0.804	0.443	0.428	0.400	0.718	0.497	0.895	0.361	0.470	0.541	0.687	0.755	0.281	0.562	0.390
	15	0.090	1.000	0.834	0.090	2.774	0.861	0.925	0.108	0.804	0.122	0.861	0.924	0.109	0.804	0.122
	22	0.351	0.933	0.490	0.342	0.856	0.910	0.918	0.086	0.841	0.094	0.909	0.918	0.087	0.841	0.095
	28	0.385	0.887	0.463	0.367	0.792	0.935	0.906	0.080	0.852	0.087	0.934	0.906	0.080	0.851	0.087
	40	0.345	0.819	0.515	0.320	0.969	0.955	0.880	0.084	0.844	0.092	0.959	0.881	0.082	0.849	0.089
Priscilla	60	0.291	0.714	0.587	0.261	1.287	0.964	0.853	0.095	0.826	0.105	0.965	0.747	0.158	0.728	0.186
	32	0.037	1.000	0.928	0.037	4.796	0.843	0.702	0.234	0.621	0.304	0.842	0.701	0.235	0.620	0.306
	35	0.150	1.000	0.739	0.150	1.910	0.854	0.695	0.234	0.621	0.303	0.854	0.695	0.233	0.622	0.303
	37	0.208	0.978	0.658	0.207	1.460	0.858	0.691	0.235	0.620	0.305	0.859	0.691	0.234	0.621	0.304
	45	0.664	0.861	0.250	0.600	0.330	0.871	0.680	0.236	0.618	0.307	0.874	0.683	0.233	0.622	0.301
Smoky	60	0.831	0.789	0.191	0.680	0.236	0.884	0.664	0.242	0.611	0.316	0.883	0.665	0.241	0.611	0.315
	35	0.064	0.471	0.887	0.060	5.094	0.832	0.703	0.238	0.616	0.311	0.819	0.699	0.246	0.605	0.325
	40	0.139	0.323	0.806	0.108	3.804	0.837	0.701	0.237	0.617	0.310	0.831	0.698	0.242	0.611	0.317
	44	0.248	0.333	0.716	0.166	2.491	0.842	0.699	0.236	0.618	0.308	0.834	0.694	0.242	0.610	0.318
	50	0.329	0.336	0.667	0.200	2.005	0.846	0.695	0.237	0.617	0.310	0.837	0.690	0.243	0.609	0.320
Johnie Boy	60	0.419	0.347	0.620	0.234	1.626	0.851	0.691	0.237	0.617	0.309	0.842	0.680	0.248	0.603	0.327
	0.3	0.001	0.000	0.999	0.000	1335.585	0.225	0.830	0.646	0.215	1.493	0.238	0.824	0.630	0.227	1.422
	0.5	0.001	0.000	0.999	0.000	1412.190	0.384	0.791	0.482	0.349	0.875	0.391	0.791	0.477	0.355	0.857
	1	0.001	0.000	0.999	0.000	1454.227	0.593	0.707	0.355	0.476	0.549	0.607	0.707	0.347	0.485	0.530
	2	0.001	0.000	0.999	0.000	1488.855	0.687	0.686	0.313	0.523	0.456	0.700	0.686	0.307	0.530	0.443
5	0.002	0.001	0.999	0.000	1126.254	0.767	0.637	0.304	0.534	0.435	0.779	0.636	0.300	0.539	0.426	

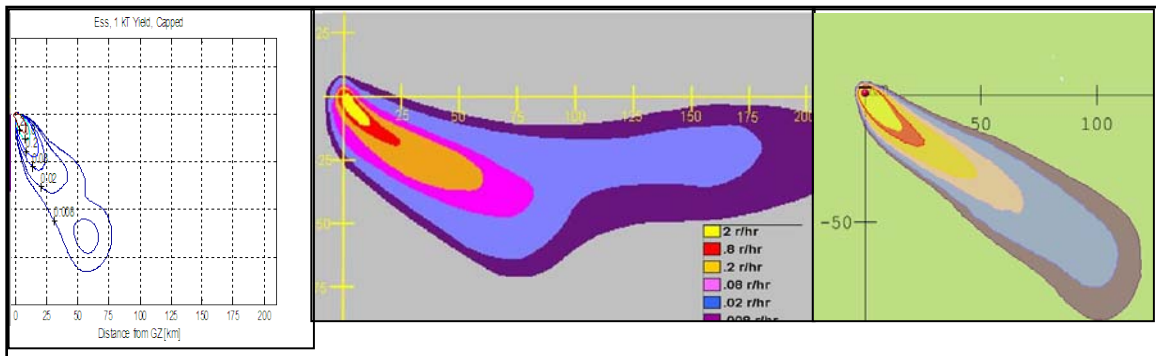
Appendix B: Visual Comparisons of Historic Yields

For each test shot, graphics are shown, from left to right, for the FDC, DNA-EX, and HPAC dose rate contours at the historic yield.

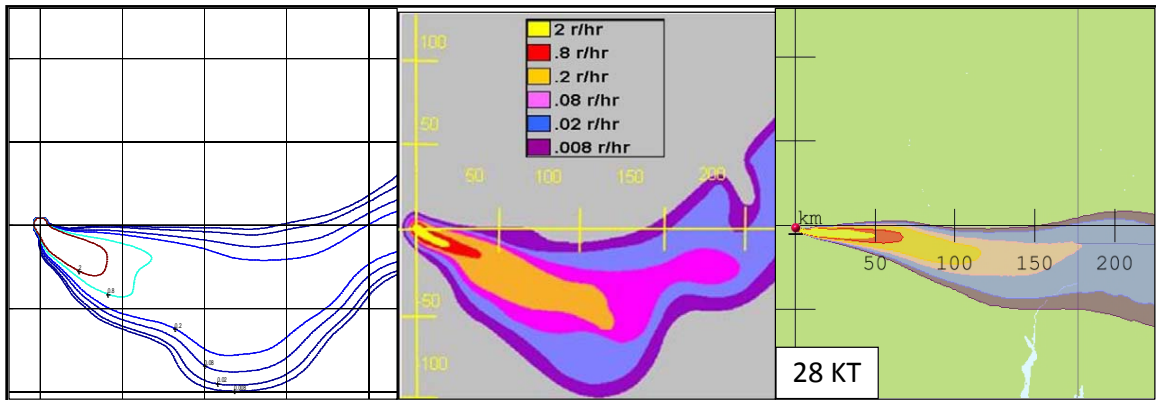
George 15KT yield dose rate contours. Note that HPAC significantly underestimates the lateral dispersion of fallout deposition. HPAC gets the cardinal direction (north) of deposition correct, but predicts movement of the cloud more to the west than east along the north-south running ridge.



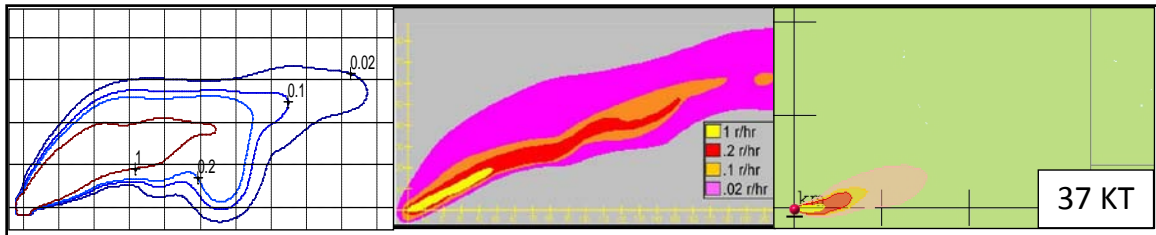
ESS 1KT yield dose rate contours. HPAC does a better job of recreating the dose rate contours over the first 100 km. In both cases, neither reproduction captures the curvature of the contours to the east beyond 100 km.



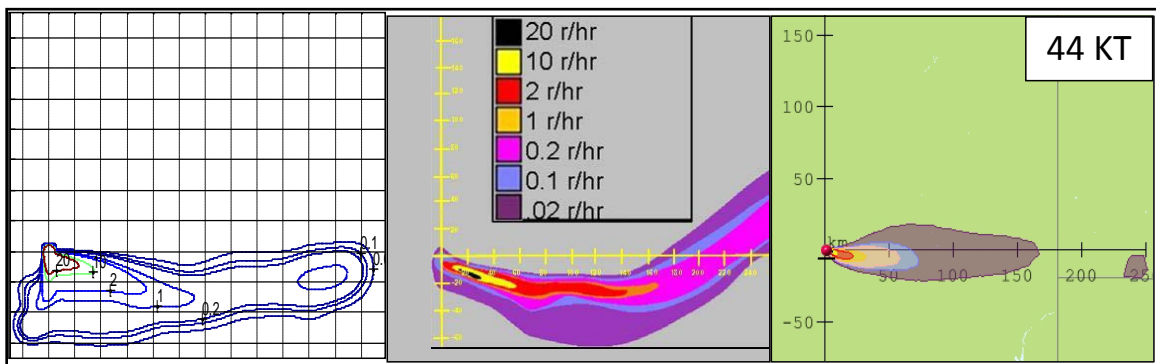
Zucchini 28KT yield dose rate contours. HPAC again fails to model the lateral dispersion and deposition of activity. The FDC provides a reasonable reproduction of the DNA-EX dose rate contours, including capturing the curvature taking place at approximately 110 km east of ground zero.



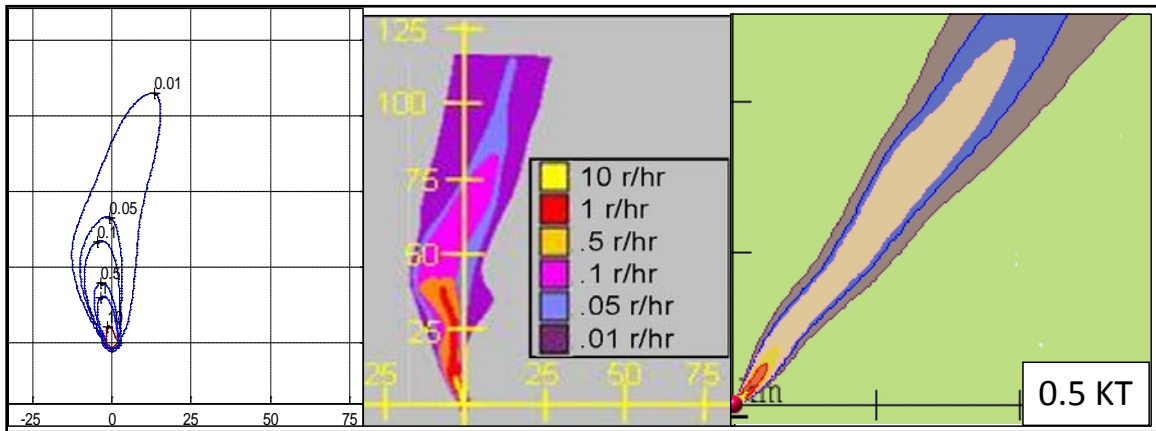
Priscilla 37KT yield dose rate contours. Neither HPAC nor FDC accurately recreate fallout deposition beyond 100 miles. The ground zero balloon wind data used in the FDC does a better job of capturing the direction of initial fallout (east-northeast) but underestimates the eventual movement of the radioactive cloud to the north.



Smoky 44KT yield dose rate contours. HPAC fails to capture the curvature of fallout deposition. The FDC is affected by the winds at elevation and the local terrain near ground zero, leading to irregular contours near ground zero. The additional deposition that occurs in the FDC near 160 km is due to the combination of zero vertical winds, a westerly wind, and a large north-south running ridgeline leading to increased deposition here.

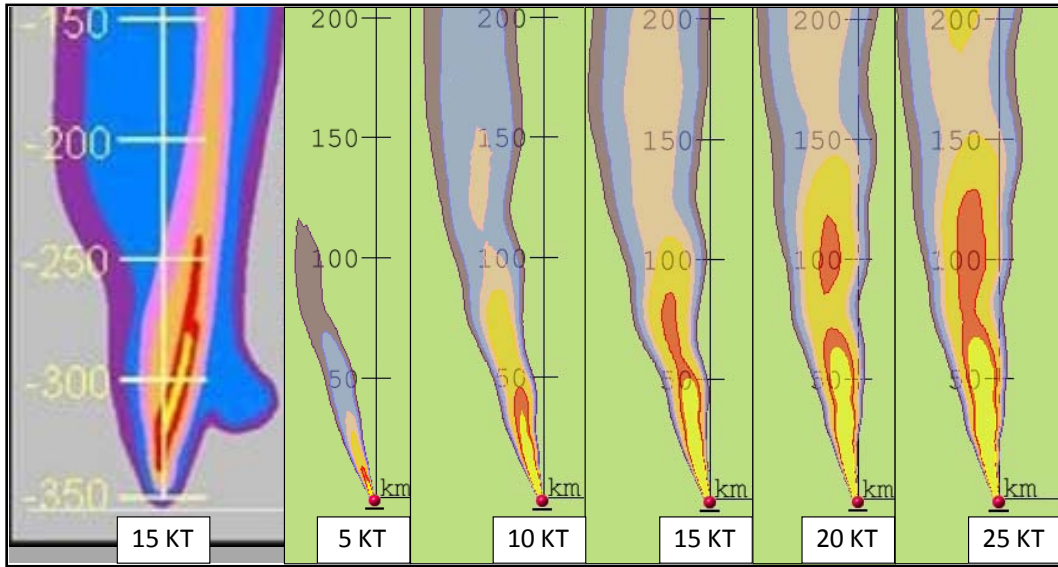


Johnie Boy 0.5KT yield dose rate contours. HPAC produced dose rate contours do not appear to account for changes to the wind at altitude. The FDC dose rate contours do not extend far enough from ground zero. However, the FDC does a reasonable job capturing the curvature of the dose rate contours that occurs at approximately 40 km north of ground zero.

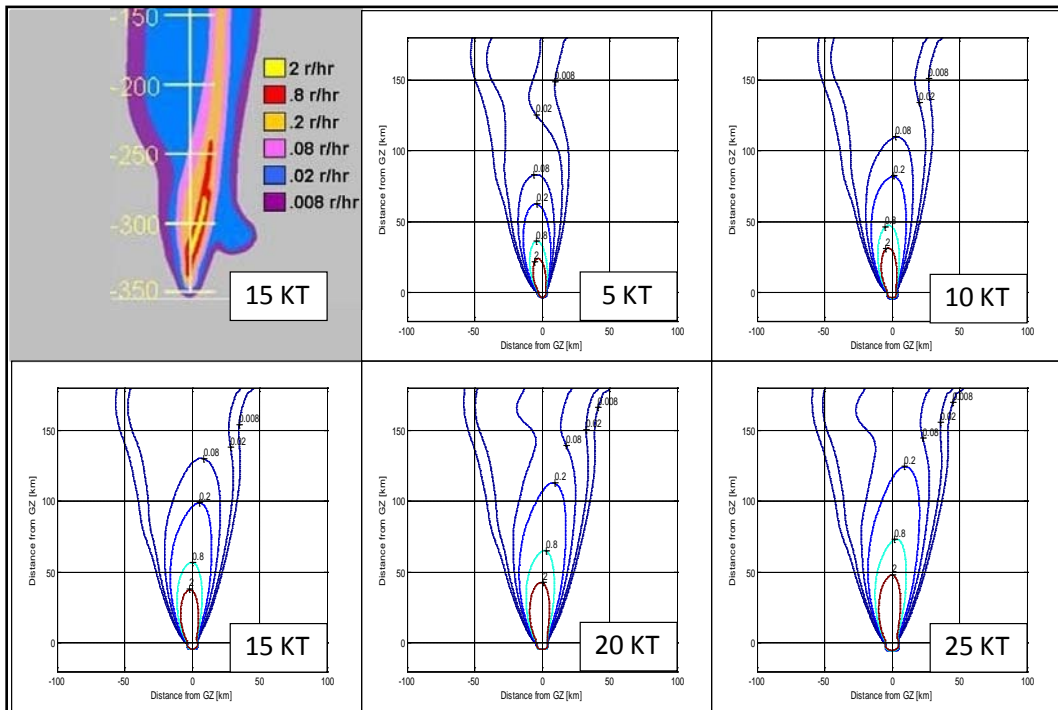


Appendix C: Dose Rate Contour Changes As a Function of Yield

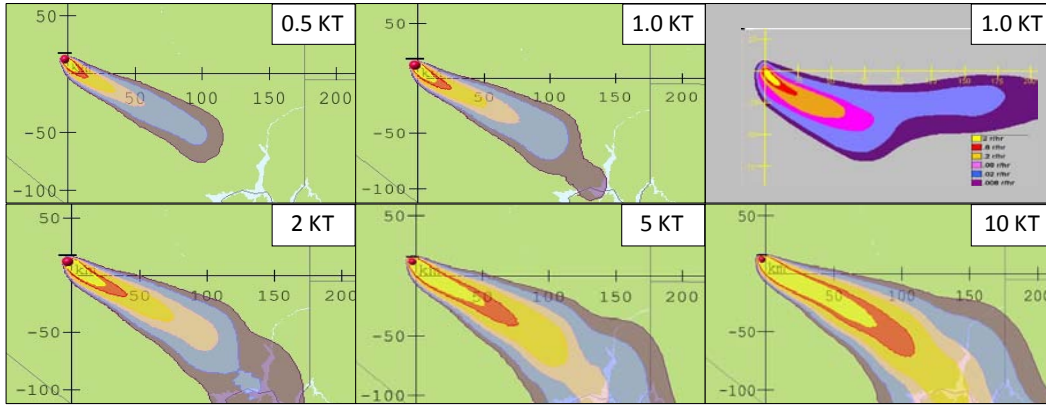
George HPAC Dose Rate Contours



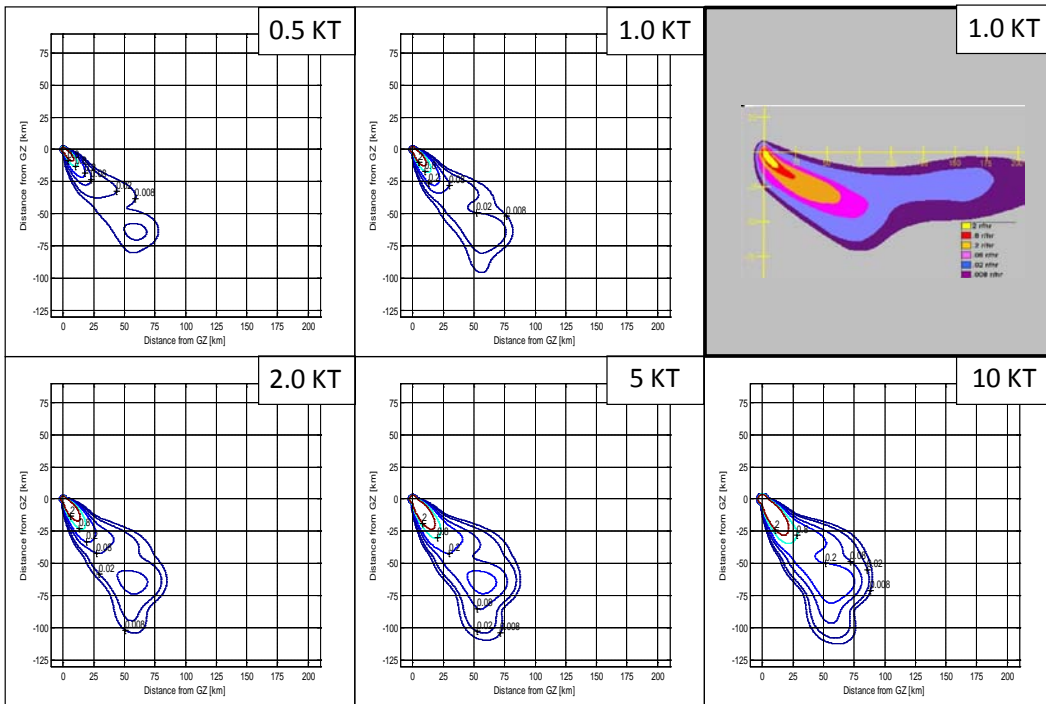
George FDC Dose Rate Contours



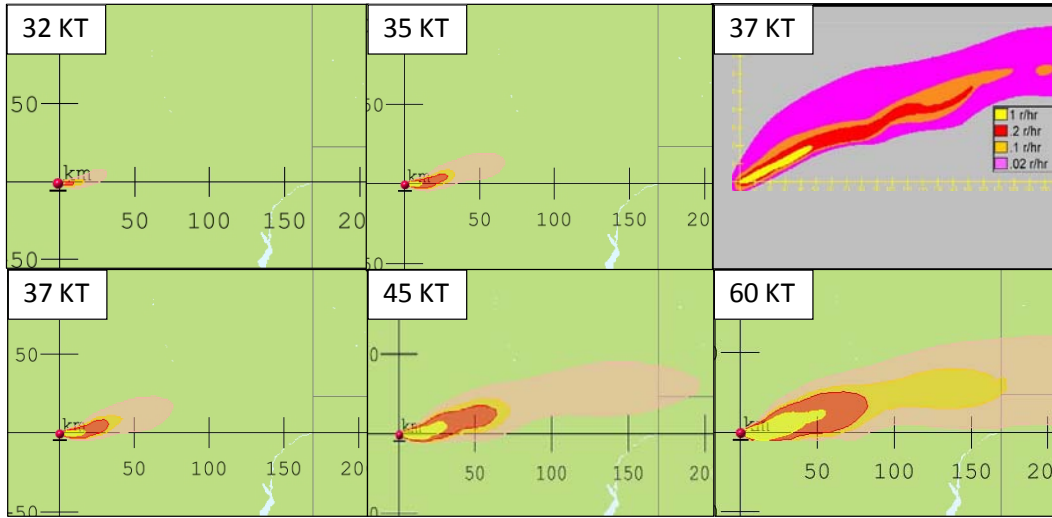
ESS HPAC Dose Rate Contours



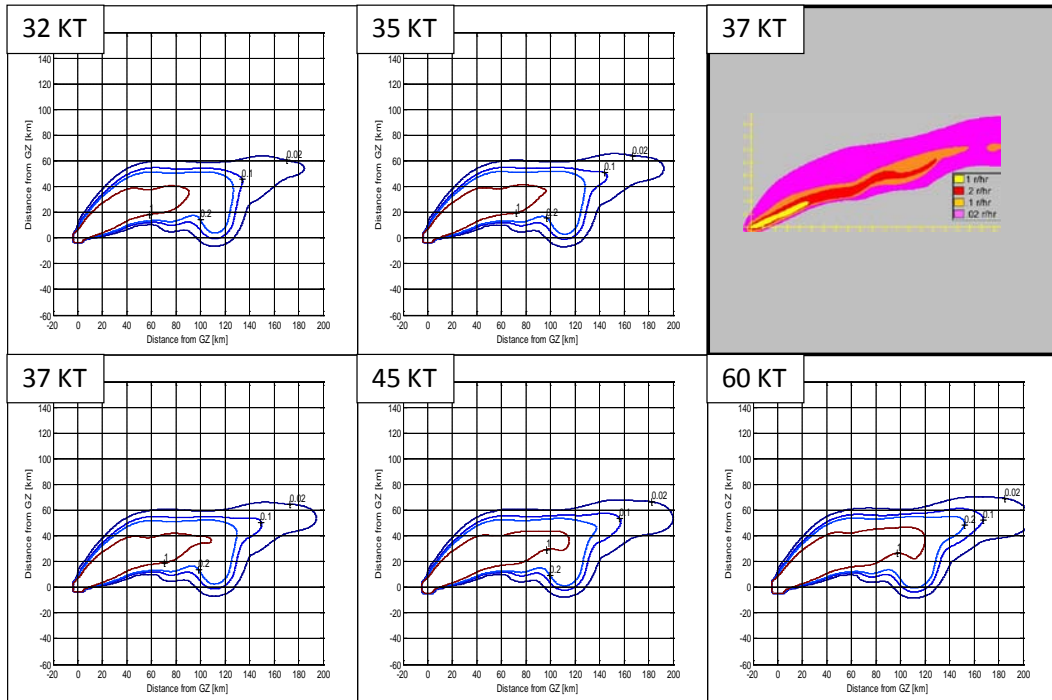
ESS FDC Dose Rate Contours



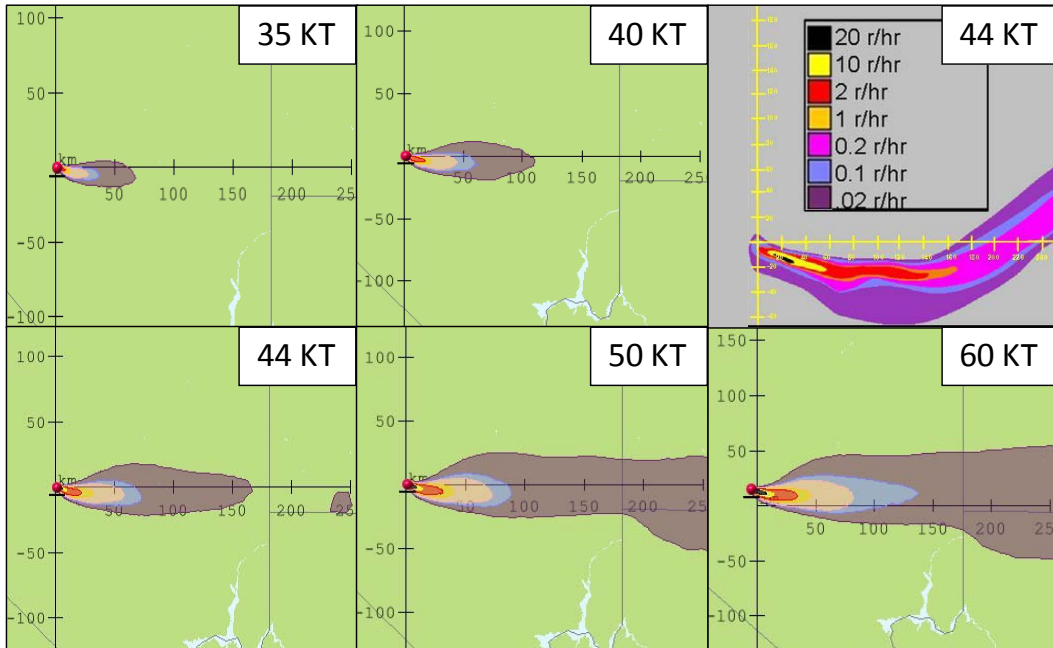
Priscilla HPAC Dose Rate Contours



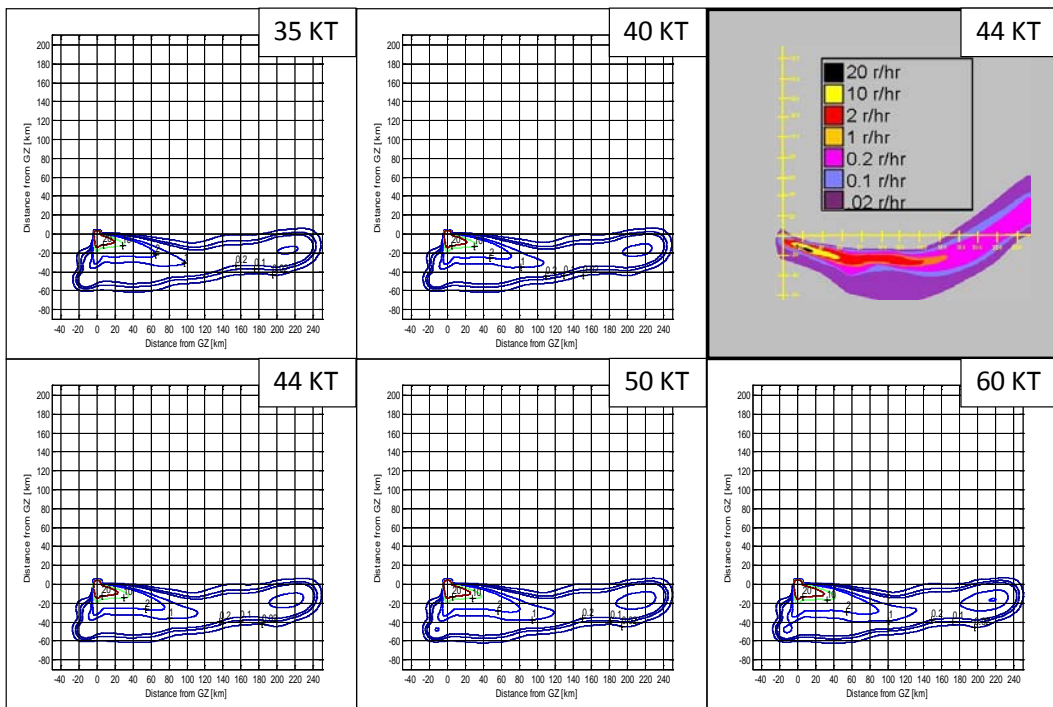
Priscilla FDC Dose Rate Contours



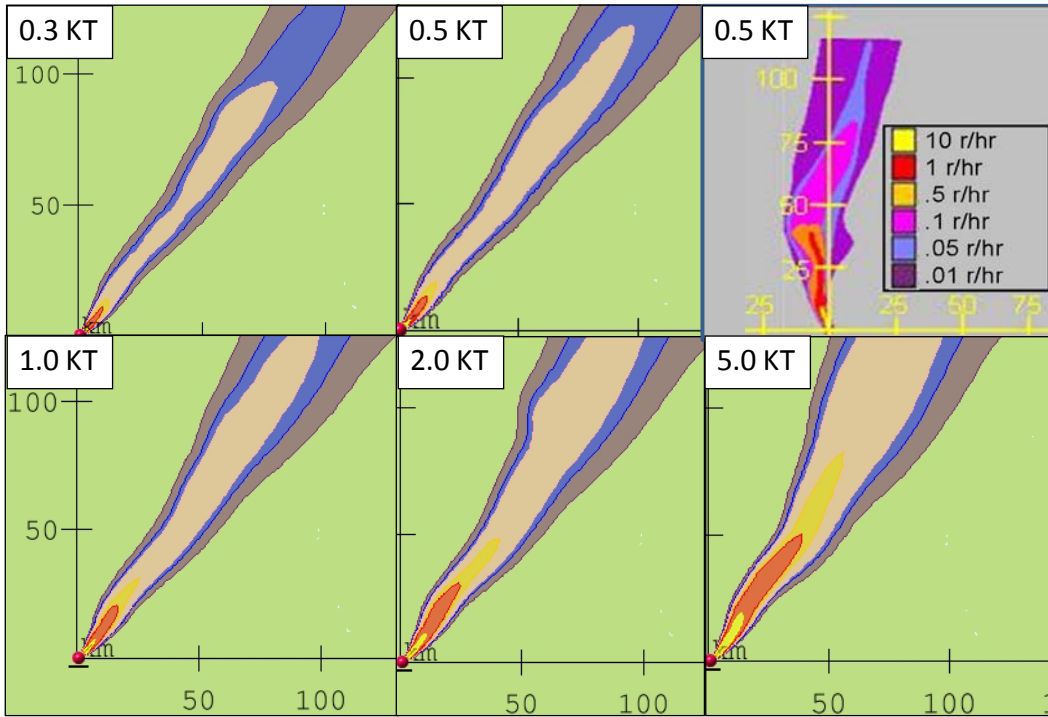
Smoky HPAC Dose Rate Contours



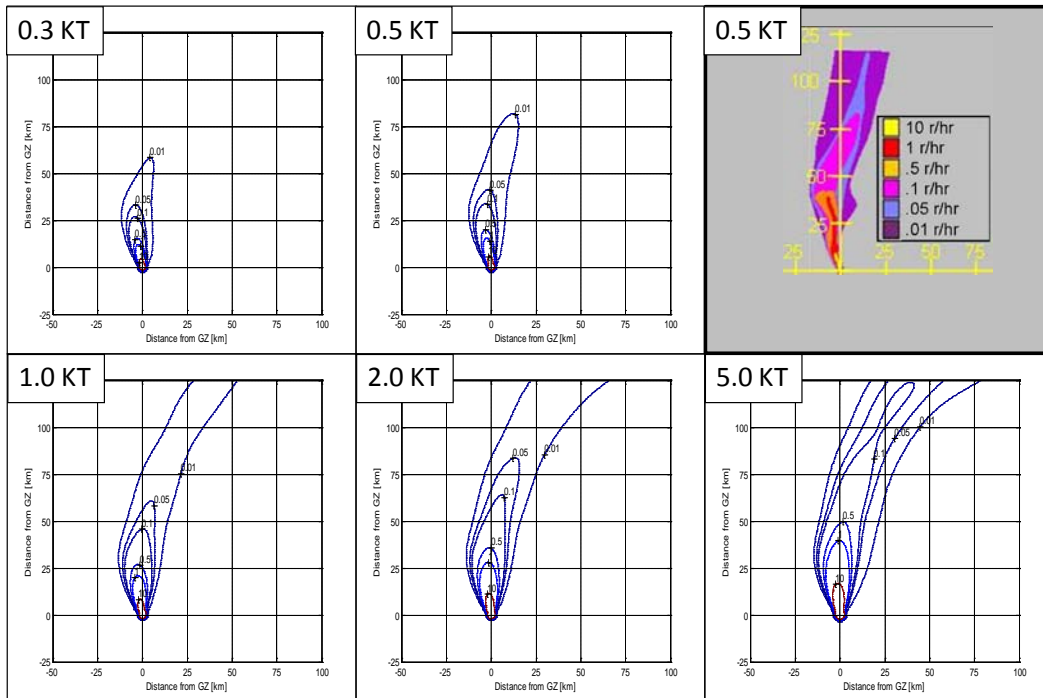
Smoky FDC Dose Rate Contours



Johnie Boy HPAC Dose Rate Contours



Johnie Boy FDC Dose Rate Contours



Appendix D: George FOM

Yield	MOEx	MOEy	NAD	FMS	FOM	REL FOM	Yield	MOEx	MOEy	NAD	FMS	FOM	REL FOM
1	0.194	0.957	0.678	0.192	1.576	↑5.448	57	0.923	0.874	0.102	0.815	0.113	1.112
2	0.410	0.945	0.428	0.401	0.687	6.733	58	0.924	0.873	0.102	0.815	0.114	1.113
3	0.520	0.946	0.329	0.505	0.469	4.598	59	0.924	0.872	0.102	0.814	0.114	1.118
4	0.599	0.948	0.266	0.580	0.353	3.460	60	0.925	0.872	0.103	0.814	0.114	1.120
5	0.659	0.949	0.222	0.636	0.281	2.756	61	0.925	0.871	0.103	0.813	0.115	1.123
6	0.702	0.949	0.193	0.677	0.236	2.316	62	0.925	0.870	0.103	0.813	0.115	1.127
7	0.734	0.949	0.172	0.706	0.206	2.021	63	0.925	0.870	0.103	0.813	0.115	1.128
8	0.759	0.948	0.157	0.729	0.185	1.812	64	0.926	0.869	0.103	0.812	0.115	1.131
9	0.780	0.947	0.144	0.748	0.168	1.647	65	0.926	0.868	0.104	0.812	0.116	1.133
10	0.797	0.946	0.135	0.762	0.155	1.522	66	0.927	0.867	0.104	0.812	0.116	1.137
11	0.811	0.944	0.127	0.774	0.145	1.424	67	0.927	0.866	0.104	0.811	0.117	1.142
12	0.824	0.943	0.121	0.785	0.137	1.343	68	0.927	0.866	0.105	0.811	0.117	1.144
13	0.834	0.941	0.116	0.792	0.131	1.281	69	0.928	0.865	0.105	0.810	0.117	1.146
14	0.844	0.939	0.111	0.800	0.125	1.221	70	0.928	0.865	0.105	0.810	0.117	1.147
15	0.852	0.938	0.107	0.807	0.120	1.172	71	0.928	0.864	0.105	0.810	0.117	1.150
16	0.860	0.936	0.104	0.812	0.115	1.131	72	0.928	0.864	0.105	0.810	0.118	1.152
17	0.866	0.935	0.101	0.817	0.112	1.101	73	0.929	0.863	0.105	0.809	0.118	1.154
18	0.873	0.933	0.098	0.822	0.109	1.064	74	0.929	0.863	0.105	0.809	0.118	1.153
19	0.879	0.931	0.096	0.825	0.106	1.037	75	0.929	0.862	0.106	0.809	0.118	1.158
20	0.882	0.929	0.095	0.827	0.105	1.028	76	0.930	0.861	0.106	0.809	0.118	1.159
21	0.887	0.927	0.094	0.829	0.103	1.012	77	0.930	0.861	0.106	0.808	0.119	1.162
22	0.890	0.924	0.093	0.829	0.103	1.010	78	0.930	0.860	0.106	0.808	0.119	1.165
23	0.894	0.922	0.093	0.831	0.102	1.000	79	0.930	0.860	0.106	0.808	0.119	1.167
24	0.896	0.919	0.093	0.830	0.102	1.002	80	0.930	0.859	0.107	0.807	0.119	1.170
25	0.898	0.917	0.093	0.830	0.102	1.001	81	0.930	0.859	0.107	0.807	0.119	1.171
26	0.900	0.915	0.093	0.830	0.102	1.003	82	0.930	0.858	0.107	0.807	0.120	1.175
27	0.901	0.912	0.093	0.829	0.103	1.008	83	0.930	0.858	0.107	0.806	0.120	1.177
28	0.903	0.910	0.093	0.829	0.103	1.010	84	0.931	0.858	0.107	0.806	0.120	1.179
29	0.904	0.908	0.094	0.829	0.103	1.014	85	0.931	0.857	0.108	0.806	0.120	1.180
30	0.905	0.907	0.094	0.828	0.104	1.017	86	0.931	0.857	0.108	0.805	0.121	1.183
31	0.907	0.905	0.094	0.828	0.104	1.020	87	0.931	0.856	0.108	0.805	0.121	1.185
32	0.908	0.903	0.095	0.827	0.105	1.024	88	0.932	0.856	0.108	0.805	0.121	1.185
33	0.909	0.901	0.095	0.827	0.105	1.026	89	0.932	0.855	0.108	0.805	0.121	1.187
34	0.911	0.899	0.095	0.827	0.105	1.027	90	0.932	0.855	0.108	0.805	0.121	1.189
35	0.912	0.898	0.095	0.826	0.105	1.032	91	0.932	0.854	0.109	0.804	0.122	1.194
36	0.912	0.897	0.096	0.826	0.106	1.036	92	0.932	0.853	0.109	0.804	0.122	1.197
37	0.913	0.895	0.096	0.825	0.106	1.042	93	0.932	0.853	0.109	0.803	0.122	1.200
38	0.914	0.894	0.096	0.824	0.107	1.045	94	0.932	0.853	0.109	0.803	0.123	1.202
39	0.915	0.892	0.097	0.823	0.107	1.051	95	0.932	0.852	0.109	0.803	0.123	1.203
40	0.915	0.891	0.097	0.823	0.108	1.056	96	0.932	0.852	0.110	0.802	0.123	1.208
41	0.915	0.890	0.098	0.822	0.108	1.060	97	0.933	0.852	0.110	0.802	0.123	1.207
42	0.916	0.889	0.098	0.822	0.109	1.064	98	0.933	0.851	0.110	0.802	0.123	1.207
43	0.917	0.887	0.098	0.821	0.109	1.070	99	0.933	0.851	0.110	0.802	0.123	1.208
44	0.917	0.886	0.099	0.821	0.109	1.071	100	0.933	0.850	0.110	0.802	0.124	1.212
45	0.917	0.885	0.099	0.820	0.110	1.078	101	0.933	0.850	0.110	0.801	0.124	1.213
46	0.918	0.884	0.099	0.819	0.110	1.083	102	0.933	0.850	0.110	0.801	0.124	1.215
47	0.919	0.883	0.099	0.819	0.110	1.082	103	0.933	0.849	0.111	0.801	0.124	1.218
48	0.920	0.882	0.099	0.819	0.110	1.082	104	0.933	0.849	0.111	0.800	0.125	1.223
49	0.921	0.881	0.100	0.819	0.111	1.086	105	0.933	0.848	0.111	0.800	0.125	1.224
50	0.921	0.880	0.100	0.818	0.111	1.088	106	0.934	0.848	0.111	0.800	0.125	1.226
51	0.922	0.879	0.100	0.818	0.111	1.092	107	0.934	0.848	0.111	0.799	0.125	1.228
52	0.922	0.878	0.101	0.817	0.112	1.096	108	0.934	0.847	0.112	0.799	0.125	1.230
53	0.922	0.877	0.101	0.817	0.112	1.099	109	0.934	0.847	0.112	0.799	0.126	1.233
54	0.922	0.876	0.101	0.816	0.113	1.104	110	0.934	0.847	0.112	0.799	0.126	1.233
55	0.923	0.876	0.101	0.816	0.113	1.106	111	0.934	0.846	0.112	0.799	0.126	1.235
56	0.923	0.875	0.102	0.815	0.113	1.111	112	0.934	0.846	0.112	0.798	0.126	1.237

Appendix E: ESS FOM

Yield	MOEx	MOEy	NAD	FMS	FOM	REL FOM	Yield	MOEx	MOEy	NAD	FMS	FOM	REL FOM
0.1	0.000	NaN	1.000	0.000	NaN		5.1	0.465	0.902	0.387	0.442	0.597	1.204
0.2	0.000	NaN	1.000	0.000	NaN		5.2	0.466	0.902	0.386	0.443	0.595	1.199
0.3	0.167	0.982	0.714	0.167	1.763	3.553	5.3	0.467	0.902	0.385	0.444	0.593	1.195
0.4	0.244	0.975	0.610	0.242	1.253	2.525	5.4	0.467	0.902	0.385	0.444	0.593	1.195
0.5	0.295	0.959	0.549	0.291	1.032	2.079	5.5	0.469	0.901	0.384	0.446	0.590	1.189
0.6	0.322	0.950	0.519	0.317	0.938	1.890	5.6	0.470	0.901	0.382	0.447	0.587	1.184
0.7	0.339	0.946	0.501	0.333	0.884	1.782	5.7	0.472	0.901	0.381	0.449	0.584	1.176
0.8	0.352	0.941	0.488	0.344	0.848	1.709	5.8	0.473	0.901	0.380	0.449	0.582	1.174
0.9	0.363	0.938	0.477	0.354	0.818	1.649	5.9	0.473	0.901	0.380	0.450	0.582	1.172
1	0.370	0.934	0.470	0.361	0.798	1.609	6	0.474	0.901	0.379	0.450	0.580	1.169
1.1	0.377	0.931	0.464	0.366	0.783	1.578	6.1	0.475	0.901	0.378	0.451	0.579	1.166
1.2	0.384	0.930	0.457	0.373	0.765	1.542	6.2	0.475	0.901	0.378	0.452	0.577	1.164
1.3	0.388	0.926	0.453	0.376	0.756	1.523	6.3	0.476	0.900	0.377	0.452	0.576	1.160
1.4	0.393	0.925	0.448	0.381	0.743	1.498	6.4	0.477	0.900	0.377	0.453	0.575	1.158
1.5	0.398	0.923	0.444	0.385	0.733	1.477	6.5	0.478	0.899	0.376	0.454	0.573	1.155
1.6	0.402	0.921	0.440	0.389	0.724	1.458	6.6	0.478	0.899	0.376	0.454	0.573	1.154
1.7	0.405	0.920	0.438	0.391	0.717	1.445	6.7	0.479	0.899	0.375	0.455	0.570	1.150
1.8	0.409	0.918	0.434	0.395	0.708	1.428	6.8	0.480	0.899	0.374	0.455	0.570	1.149
1.9	0.412	0.918	0.432	0.397	0.703	1.416	6.9	0.480	0.898	0.374	0.456	0.569	1.147
2	0.415	0.917	0.429	0.400	0.695	1.401	7	0.480	0.898	0.374	0.456	0.569	1.147
2.1	0.418	0.916	0.426	0.402	0.689	1.389	7.1	0.481	0.898	0.373	0.456	0.568	1.145
2.2	0.420	0.915	0.424	0.404	0.684	1.379	7.2	0.482	0.898	0.373	0.457	0.567	1.143
2.3	0.422	0.914	0.422	0.406	0.680	1.370	7.3	0.483	0.898	0.372	0.458	0.565	1.139
2.4	0.425	0.913	0.420	0.409	0.674	1.358	7.4	0.484	0.898	0.371	0.458	0.564	1.136
2.5	0.428	0.913	0.417	0.411	0.668	1.346	7.5	0.484	0.898	0.371	0.459	0.563	1.134
2.6	0.430	0.912	0.416	0.413	0.664	1.338	7.6	0.485	0.898	0.371	0.459	0.562	1.132
2.7	0.432	0.912	0.414	0.414	0.660	1.330	7.7	0.485	0.898	0.370	0.460	0.561	1.130
2.8	0.433	0.910	0.413	0.416	0.657	1.324	7.8	0.485	0.898	0.370	0.460	0.560	1.129
2.9	0.435	0.910	0.411	0.417	0.654	1.318	7.9	0.486	0.898	0.369	0.461	0.559	1.126
3	0.438	0.910	0.409	0.419	0.648	1.307	8	0.487	0.898	0.368	0.462	0.557	1.122
3.1	0.440	0.910	0.407	0.421	0.643	1.297	8.1	0.487	0.898	0.368	0.462	0.556	1.121
3.2	0.441	0.909	0.406	0.423	0.641	1.291	8.2	0.488	0.898	0.368	0.462	0.556	1.120
3.3	0.443	0.909	0.405	0.424	0.638	1.286	8.3	0.488	0.898	0.367	0.463	0.555	1.118
3.4	0.445	0.908	0.403	0.425	0.634	1.278	8.4	0.489	0.898	0.367	0.463	0.553	1.115
3.5	0.446	0.908	0.402	0.427	0.631	1.272	8.5	0.490	0.897	0.366	0.464	0.553	1.114
3.6	0.447	0.907	0.401	0.428	0.630	1.269	8.6	0.490	0.897	0.366	0.464	0.551	1.111
3.7	0.449	0.906	0.400	0.429	0.627	1.265	8.7	0.491	0.897	0.365	0.465	0.551	1.110
3.8	0.450	0.906	0.399	0.430	0.625	1.259	8.8	0.491	0.897	0.365	0.465	0.550	1.108
3.9	0.452	0.906	0.397	0.432	0.621	1.251	8.9	0.492	0.897	0.364	0.466	0.548	1.105
4	0.452	0.905	0.397	0.432	0.620	1.249	9	0.493	0.897	0.364	0.466	0.547	1.103
4.1	0.454	0.905	0.395	0.433	0.616	1.242	9.1	0.493	0.897	0.364	0.467	0.547	1.103
4.2	0.456	0.905	0.394	0.435	0.613	1.236	9.2	0.493	0.897	0.364	0.467	0.547	1.102
4.3	0.457	0.904	0.393	0.436	0.611	1.232	9.3	0.494	0.897	0.363	0.467	0.546	1.100
4.4	0.458	0.904	0.392	0.437	0.609	1.226	9.4	0.494	0.897	0.363	0.468	0.545	1.098
4.5	0.459	0.904	0.391	0.438	0.607	1.223	9.5	0.495	0.897	0.362	0.468	0.544	1.097
4.6	0.460	0.903	0.390	0.439	0.605	1.219	9.6	0.495	0.896	0.362	0.468	0.544	1.096
4.7	0.461	0.903	0.390	0.439	0.604	1.217	9.7	0.496	0.897	0.362	0.469	0.543	1.094
4.8	0.462	0.903	0.389	0.440	0.601	1.212	9.8	0.496	0.896	0.362	0.469	0.542	1.093
4.9	0.463	0.902	0.388	0.441	0.600	1.209	9.9	0.496	0.896	0.361	0.469	0.542	1.092
5	0.464	0.902	0.387	0.442	0.598	1.204	10	0.497	0.895	0.361	0.470	0.541	1.090

Yield	MOEx	MOEy	NAD	FMS	FOM	REL FOM	Yield	MOEx	MOEy	NAD	FMS	FOM	REL FOM
10.1	0.497	0.895	0.360	0.470	0.540	1.089	15.1	0.514	0.893	0.347	0.484	0.513	1.033
10.2	0.498	0.895	0.360	0.471	0.539	1.086	15.2	0.514	0.893	0.347	0.484	0.513	1.033
10.3	0.499	0.895	0.359	0.471	0.538	1.084	15.3	0.515	0.893	0.347	0.485	0.512	1.032
10.4	0.499	0.895	0.359	0.472	0.537	1.082	15.4	0.515	0.892	0.347	0.485	0.512	1.032
10.5	0.500	0.895	0.359	0.472	0.536	1.081	15.5	0.515	0.892	0.347	0.485	0.512	1.032
10.6	0.500	0.895	0.358	0.472	0.536	1.079	15.6	0.516	0.893	0.346	0.485	0.511	1.029
10.7	0.500	0.895	0.358	0.473	0.535	1.079	15.7	0.516	0.892	0.346	0.486	0.510	1.028
10.8	0.500	0.895	0.358	0.473	0.535	1.078	15.8	0.516	0.892	0.346	0.486	0.510	1.028
10.9	0.501	0.895	0.358	0.473	0.535	1.078	15.9	0.517	0.892	0.346	0.486	0.509	1.026
11	0.501	0.895	0.358	0.473	0.534	1.076	16	0.517	0.892	0.346	0.486	0.509	1.026
11.1	0.502	0.895	0.357	0.474	0.533	1.074	16.1	0.517	0.892	0.346	0.486	0.509	1.026
11.2	0.502	0.895	0.357	0.474	0.532	1.072	16.2	0.517	0.892	0.345	0.487	0.508	1.025
11.3	0.503	0.895	0.356	0.475	0.531	1.070	16.3	0.517	0.892	0.345	0.487	0.508	1.024
11.4	0.503	0.895	0.356	0.475	0.530	1.068	16.4	0.518	0.892	0.345	0.487	0.507	1.023
11.5	0.503	0.895	0.356	0.475	0.530	1.067	16.5	0.518	0.892	0.345	0.487	0.507	1.023
11.6	0.504	0.895	0.355	0.476	0.529	1.066	16.6	0.518	0.892	0.345	0.487	0.507	1.023
11.7	0.504	0.895	0.355	0.476	0.529	1.066	16.7	0.518	0.892	0.345	0.487	0.507	1.022
11.8	0.504	0.895	0.355	0.476	0.528	1.065	16.8	0.519	0.892	0.344	0.488	0.506	1.020
11.9	0.505	0.895	0.355	0.476	0.528	1.063	16.9	0.519	0.892	0.344	0.488	0.506	1.019
12	0.505	0.895	0.354	0.477	0.527	1.063	17	0.519	0.892	0.344	0.488	0.506	1.020
12.1	0.506	0.895	0.354	0.477	0.526	1.061	17.1	0.519	0.892	0.344	0.488	0.505	1.019
12.2	0.506	0.895	0.354	0.477	0.526	1.060	17.2	0.519	0.892	0.344	0.489	0.505	1.017
12.3	0.506	0.895	0.354	0.478	0.526	1.059	17.3	0.520	0.892	0.343	0.489	0.504	1.016
12.4	0.506	0.895	0.353	0.478	0.525	1.059	17.4	0.520	0.892	0.343	0.489	0.504	1.015
12.5	0.506	0.894	0.353	0.478	0.525	1.059	17.5	0.520	0.892	0.343	0.489	0.504	1.015
12.6	0.507	0.894	0.353	0.478	0.524	1.057	17.6	0.520	0.891	0.343	0.489	0.504	1.015
12.7	0.507	0.894	0.353	0.478	0.524	1.057	17.7	0.521	0.892	0.342	0.490	0.503	1.013
12.8	0.507	0.894	0.353	0.479	0.523	1.055	17.8	0.521	0.892	0.342	0.490	0.502	1.013
12.9	0.508	0.895	0.352	0.479	0.523	1.054	17.9	0.521	0.891	0.342	0.490	0.502	1.011
13	0.508	0.895	0.352	0.479	0.522	1.052	18	0.521	0.891	0.342	0.490	0.502	1.011
13.1	0.509	0.895	0.351	0.480	0.521	1.050	18.1	0.522	0.891	0.342	0.491	0.501	1.010
13.2	0.509	0.895	0.351	0.480	0.521	1.050	18.2	0.522	0.891	0.341	0.491	0.500	1.008
13.3	0.509	0.895	0.351	0.480	0.521	1.049	18.3	0.522	0.891	0.341	0.491	0.500	1.008
13.4	0.509	0.894	0.351	0.480	0.520	1.048	18.4	0.522	0.891	0.341	0.491	0.500	1.008
13.5	0.510	0.894	0.351	0.481	0.519	1.046	18.5	0.523	0.891	0.341	0.491	0.500	1.008
13.6	0.510	0.894	0.350	0.481	0.519	1.046	18.6	0.523	0.891	0.341	0.491	0.500	1.007
13.7	0.511	0.894	0.350	0.481	0.518	1.045	18.7	0.523	0.891	0.341	0.492	0.499	1.006
13.8	0.511	0.894	0.350	0.481	0.518	1.044	18.8	0.523	0.891	0.341	0.492	0.499	1.005
13.9	0.511	0.893	0.350	0.481	0.518	1.044	18.9	0.524	0.891	0.340	0.492	0.498	1.004
14	0.511	0.893	0.350	0.482	0.518	1.044	19	0.524	0.891	0.340	0.492	0.498	1.003
14.1	0.511	0.893	0.350	0.482	0.518	1.044	19.1	0.524	0.891	0.340	0.492	0.498	1.003
14.2	0.511	0.893	0.350	0.482	0.518	1.043	19.2	0.524	0.891	0.340	0.493	0.498	1.003
14.3	0.511	0.893	0.350	0.482	0.517	1.043	19.3	0.524	0.891	0.340	0.493	0.498	1.003
14.4	0.512	0.893	0.349	0.482	0.517	1.042	19.4	0.524	0.891	0.340	0.493	0.497	1.002
14.5	0.512	0.893	0.349	0.482	0.516	1.041	19.5	0.524	0.891	0.340	0.493	0.497	1.001
14.6	0.512	0.893	0.349	0.483	0.516	1.040	19.6	0.524	0.891	0.340	0.493	0.497	1.001
14.7	0.512	0.893	0.349	0.483	0.516	1.040	19.7	0.525	0.891	0.340	0.493	0.497	1.001
14.8	0.513	0.893	0.349	0.483	0.515	1.038	19.8	0.525	0.891	0.339	0.493	0.496	1.000
14.9	0.513	0.893	0.348	0.483	0.514	1.037	19.9	0.525	0.891	0.339	0.493	0.496	1.000
15	0.514	0.893	0.348	0.484	0.513	1.035	20	0.525	0.891	0.339	0.493	0.496	1.000

Appendix F: Zucchini FOM

Yield	MOEx	MOEy	NAD	FMS	FOM	REL FOM	Yield	MOEx	MOEy	NAD	FMS	FOM	REL FOM
1	0.288	0.970	0.556	0.285	1.052	12.300	57	0.963	0.855	0.095	0.827	0.104	1.218
2	0.476	0.935	0.370	0.460	0.554	6.482	58	0.963	0.854	0.095	0.827	0.104	1.221
3	0.544	0.920	0.317	0.519	0.448	5.233	59	0.963	0.853	0.095	0.826	0.105	1.226
4	0.595	0.918	0.278	0.565	0.376	4.393	60	0.964	0.853	0.095	0.826	0.105	1.227
5	0.644	0.919	0.243	0.610	0.315	3.686	61	0.964	0.852	0.096	0.825	0.106	1.234
6	0.688	0.921	0.212	0.650	0.267	3.118	62	0.964	0.851	0.096	0.825	0.106	1.237
7	0.724	0.922	0.189	0.682	0.231	2.703	63	0.965	0.850	0.096	0.824	0.107	1.245
8	0.752	0.923	0.171	0.708	0.205	2.400	64	0.965	0.849	0.097	0.824	0.107	1.249
9	0.777	0.924	0.156	0.730	0.184	2.154	65	0.965	0.848	0.097	0.823	0.107	1.255
10	0.796	0.924	0.145	0.747	0.169	1.976	66	0.965	0.847	0.098	0.822	0.108	1.261
11	0.813	0.925	0.134	0.763	0.155	1.811	67	0.967	0.847	0.097	0.823	0.107	1.255
12	0.827	0.925	0.127	0.775	0.145	1.691	68	0.968	0.846	0.097	0.823	0.107	1.252
13	0.839	0.925	0.120	0.785	0.137	1.596	69	0.968	0.846	0.097	0.823	0.107	1.255
14	0.850	0.925	0.114	0.795	0.128	1.502	70	0.968	0.845	0.098	0.822	0.108	1.260
15	0.861	0.925	0.108	0.804	0.122	1.421	71	0.968	0.844	0.098	0.822	0.108	1.265
16	0.870	0.924	0.104	0.812	0.116	1.352	72	0.968	0.844	0.098	0.821	0.109	1.270
17	0.880	0.924	0.099	0.820	0.109	1.279	73	0.969	0.843	0.099	0.820	0.109	1.276
18	0.886	0.923	0.096	0.824	0.106	1.244	74	0.969	0.843	0.099	0.820	0.109	1.278
19	0.892	0.921	0.094	0.828	0.104	1.210	75	0.969	0.842	0.099	0.820	0.109	1.278
20	0.899	0.921	0.091	0.834	0.100	1.165	76	0.969	0.842	0.099	0.820	0.110	1.283
21	0.904	0.919	0.089	0.837	0.097	1.136	77	0.969	0.841	0.099	0.819	0.110	1.284
22	0.910	0.918	0.086	0.841	0.094	1.104	78	0.969	0.841	0.099	0.819	0.110	1.288
23	0.914	0.916	0.085	0.843	0.093	1.085	79	0.970	0.841	0.099	0.819	0.110	1.287
24	0.919	0.914	0.083	0.846	0.091	1.065	80	0.970	0.840	0.099	0.819	0.110	1.288
25	0.925	0.912	0.082	0.849	0.089	1.039	81	0.970	0.840	0.100	0.819	0.110	1.289
26	0.929	0.911	0.080	0.851	0.087	1.021	82	0.970	0.840	0.100	0.819	0.111	1.292
27	0.932	0.908	0.080	0.852	0.087	1.019	83	0.970	0.839	0.100	0.818	0.111	1.297
28	0.935	0.906	0.080	0.852	0.087	1.013	84	0.970	0.839	0.100	0.818	0.111	1.299
29	0.939	0.905	0.079	0.854	0.086	1.000	85	0.970	0.838	0.101	0.817	0.112	1.306
30	0.941	0.901	0.080	0.853	0.086	1.010	86	0.970	0.837	0.101	0.817	0.112	1.310
31	0.943	0.900	0.079	0.853	0.086	1.006	87	0.971	0.837	0.101	0.816	0.112	1.313
32	0.944	0.896	0.081	0.851	0.088	1.025	88	0.971	0.836	0.101	0.816	0.112	1.315
33	0.945	0.894	0.081	0.850	0.088	1.032	89	0.971	0.836	0.102	0.816	0.113	1.319
34	0.948	0.894	0.080	0.852	0.087	1.017	90	0.971	0.835	0.102	0.815	0.113	1.322
35	0.950	0.891	0.080	0.851	0.087	1.023	91	0.972	0.835	0.102	0.815	0.113	1.323
36	0.952	0.888	0.081	0.850	0.088	1.033	92	0.972	0.835	0.102	0.815	0.113	1.326
37	0.953	0.886	0.082	0.849	0.089	1.040	93	0.972	0.834	0.102	0.815	0.113	1.326
38	0.953	0.884	0.082	0.848	0.090	1.050	94	0.972	0.834	0.102	0.814	0.114	1.328
39	0.954	0.882	0.084	0.846	0.091	1.065	95	0.972	0.833	0.102	0.814	0.114	1.330
40	0.955	0.880	0.084	0.844	0.092	1.076	96	0.972	0.833	0.103	0.814	0.114	1.332
41	0.955	0.877	0.085	0.843	0.093	1.090	97	0.972	0.833	0.103	0.814	0.114	1.335
42	0.956	0.875	0.086	0.841	0.094	1.104	98	0.972	0.832	0.103	0.813	0.115	1.339
43	0.958	0.874	0.086	0.841	0.094	1.103	99	0.973	0.832	0.103	0.813	0.115	1.342
44	0.958	0.871	0.087	0.840	0.095	1.115	100	0.974	0.832	0.103	0.814	0.114	1.333
45	0.958	0.870	0.088	0.838	0.096	1.126	101	0.975	0.832	0.103	0.814	0.114	1.331
46	0.959	0.869	0.088	0.838	0.097	1.133	102	0.975	0.831	0.103	0.814	0.114	1.332
47	0.959	0.866	0.090	0.835	0.098	1.151	103	0.975	0.831	0.103	0.814	0.114	1.334
48	0.960	0.865	0.090	0.834	0.099	1.158	104	0.976	0.830	0.103	0.813	0.114	1.337
49	0.960	0.864	0.091	0.834	0.099	1.163	105	0.976	0.830	0.103	0.813	0.115	1.340
50	0.960	0.863	0.091	0.833	0.100	1.171	106	0.976	0.830	0.103	0.813	0.115	1.341
51	0.961	0.862	0.092	0.832	0.101	1.176	107	0.976	0.830	0.103	0.813	0.115	1.340
52	0.961	0.860	0.092	0.831	0.101	1.185	108	0.976	0.829	0.103	0.813	0.115	1.342
53	0.962	0.858	0.093	0.830	0.102	1.198	109	0.976	0.829	0.103	0.813	0.115	1.342
54	0.962	0.857	0.094	0.829	0.103	1.205	110	0.976	0.829	0.103	0.813	0.115	1.341
55	0.962	0.856	0.094	0.828	0.104	1.212	111	0.977	0.829	0.103	0.813	0.115	1.341
56	0.963	0.855	0.094	0.828	0.104	1.215	112	0.977	0.829	0.103	0.813	0.115	1.344

Appendix G: Priscilla FOM

Yield	MOEx	MOEy	NAD	FMS	FOM	REL FOM	Yield	MOEx	MOEy	NAD	FMS	FOM	REL FOM
1	0.106	0.497	0.825	0.096	3.590	11.841	57	0.882	0.666	0.241	0.611	0.315	1.038
2	0.216	0.597	0.683	0.189	1.901	6.270	58	0.882	0.666	0.241	0.611	0.315	1.039
3	0.304	0.654	0.585	0.261	1.314	4.335	59	0.883	0.665	0.241	0.611	0.315	1.040
4	0.387	0.695	0.503	0.331	0.971	3.202	60	0.884	0.664	0.242	0.611	0.316	1.041
5	0.439	0.715	0.456	0.373	0.815	2.689	61	0.885	0.663	0.242	0.610	0.316	1.042
6	0.476	0.727	0.425	0.404	0.722	2.382	62	0.886	0.662	0.242	0.610	0.316	1.043
7	0.508	0.736	0.399	0.430	0.652	2.152	63	0.886	0.662	0.242	0.610	0.317	1.044
8	0.543	0.745	0.372	0.458	0.585	1.930	64	0.886	0.661	0.243	0.609	0.317	1.046
9	0.580	0.755	0.344	0.489	0.519	1.712	65	0.887	0.661	0.243	0.609	0.317	1.047
10	0.604	0.748	0.332	0.502	0.494	1.628	66	0.888	0.660	0.243	0.609	0.317	1.046
11	0.615	0.735	0.330	0.503	0.491	1.620	67	0.888	0.659	0.243	0.609	0.318	1.048
12	0.624	0.726	0.329	0.505	0.488	1.611	68	0.890	0.659	0.243	0.609	0.317	1.045
13	0.632	0.719	0.327	0.507	0.486	1.602	69	0.891	0.658	0.243	0.609	0.317	1.045
14	0.639	0.712	0.326	0.508	0.484	1.596	70	0.892	0.658	0.243	0.609	0.317	1.047
15	0.644	0.707	0.326	0.508	0.484	1.596	71	0.892	0.657	0.243	0.609	0.318	1.048
16	0.648	0.701	0.327	0.508	0.485	1.599	72	0.892	0.656	0.244	0.608	0.318	1.050
17	0.653	0.697	0.326	0.508	0.483	1.594	73	0.893	0.655	0.244	0.608	0.319	1.052
18	0.656	0.693	0.326	0.508	0.484	1.595	74	0.893	0.655	0.244	0.607	0.320	1.054
19	0.662	0.691	0.324	0.511	0.479	1.579	75	0.894	0.654	0.244	0.607	0.320	1.054
20	0.668	0.688	0.322	0.513	0.475	1.568	76	0.895	0.654	0.245	0.607	0.320	1.055
21	0.675	0.688	0.319	0.517	0.468	1.543	77	0.896	0.653	0.245	0.607	0.320	1.054
22	0.682	0.687	0.316	0.520	0.461	1.521	78	0.896	0.653	0.245	0.607	0.320	1.057
23	0.691	0.687	0.311	0.525	0.452	1.490	79	0.896	0.652	0.245	0.606	0.321	1.057
24	0.703	0.687	0.305	0.532	0.439	1.448	80	0.896	0.651	0.245	0.606	0.321	1.060
25	0.732	0.694	0.287	0.554	0.403	1.330	81	0.897	0.651	0.246	0.606	0.322	1.061
26	0.760	0.700	0.271	0.573	0.372	1.227	82	0.897	0.650	0.246	0.605	0.322	1.063
27	0.784	0.704	0.258	0.590	0.347	1.145	83	0.897	0.650	0.246	0.605	0.323	1.064
28	0.805	0.708	0.247	0.604	0.327	1.077	84	0.898	0.649	0.247	0.604	0.323	1.067
29	0.820	0.708	0.240	0.613	0.315	1.040	85	0.898	0.648	0.247	0.604	0.324	1.068
30	0.830	0.707	0.236	0.618	0.309	1.018	86	0.899	0.648	0.247	0.604	0.324	1.069
31	0.837	0.705	0.235	0.620	0.306	1.008	87	0.899	0.647	0.247	0.603	0.325	1.070
32	0.843	0.702	0.234	0.621	0.304	1.004	88	0.900	0.647	0.247	0.603	0.324	1.069
33	0.848	0.700	0.234	0.621	0.303	1.000	89	0.900	0.646	0.248	0.603	0.325	1.071
34	0.851	0.697	0.234	0.621	0.304	1.001	90	0.900	0.646	0.248	0.603	0.325	1.073
35	0.854	0.695	0.234	0.621	0.303	1.001	91	0.901	0.645	0.248	0.602	0.326	1.075
36	0.856	0.693	0.234	0.621	0.303	1.000	92	0.901	0.644	0.249	0.602	0.326	1.077
37	0.858	0.691	0.235	0.620	0.305	1.005	93	0.901	0.644	0.249	0.601	0.327	1.078
38	0.860	0.689	0.235	0.620	0.305	1.006	94	0.901	0.644	0.249	0.601	0.327	1.079
39	0.862	0.688	0.235	0.620	0.305	1.006	95	0.901	0.643	0.249	0.601	0.328	1.081
40	0.863	0.687	0.235	0.620	0.305	1.006	96	0.902	0.643	0.250	0.600	0.328	1.082
41	0.865	0.686	0.235	0.620	0.305	1.006	97	0.902	0.642	0.250	0.600	0.328	1.082
42	0.866	0.684	0.236	0.619	0.306	1.010	98	0.902	0.642	0.250	0.600	0.329	1.084
43	0.869	0.683	0.235	0.619	0.305	1.007	99	0.902	0.642	0.250	0.600	0.329	1.085
44	0.870	0.682	0.235	0.619	0.305	1.007	100	0.902	0.641	0.250	0.600	0.329	1.086
45	0.871	0.680	0.236	0.618	0.307	1.012	101	0.904	0.641	0.250	0.600	0.329	1.085
46	0.872	0.679	0.237	0.617	0.308	1.015	102	0.905	0.640	0.250	0.600	0.329	1.084
47	0.873	0.677	0.237	0.616	0.309	1.019	103	0.905	0.640	0.250	0.600	0.329	1.084
48	0.874	0.676	0.238	0.616	0.309	1.019	104	0.905	0.640	0.250	0.600	0.329	1.085
49	0.875	0.675	0.238	0.616	0.309	1.020	105	0.905	0.639	0.251	0.599	0.329	1.086
50	0.876	0.674	0.238	0.616	0.310	1.021	106	0.906	0.639	0.251	0.599	0.329	1.087
51	0.877	0.673	0.238	0.615	0.310	1.023	107	0.906	0.639	0.251	0.599	0.330	1.088
52	0.878	0.671	0.239	0.614	0.312	1.029	108	0.906	0.638	0.251	0.599	0.330	1.089
53	0.878	0.670	0.240	0.613	0.312	1.031	109	0.906	0.638	0.251	0.598	0.331	1.091
54	0.879	0.669	0.240	0.612	0.313	1.034	110	0.906	0.638	0.251	0.598	0.331	1.090
55	0.880	0.668	0.240	0.613	0.313	1.033	111	0.907	0.637	0.251	0.598	0.331	1.091
56	0.881	0.667	0.241	0.612	0.314	1.036	112	0.907	0.637	0.252	0.598	0.331	1.093

Appendix H: Smoky FOM

Yield	MOEx	MOEy	NAD	FMS	FOM	REL FOM	Yield	MOEx	MOEy	NAD	FMS	FOM	REL FOM
1	0.045	0.355	0.919	0.042	7.240	23.648	57	0.850	0.692	0.237	0.617	0.309	1.010
2	0.119	0.401	0.817	0.101	3.739	12.213	58	0.850	0.692	0.237	0.617	0.309	1.010
3	0.290	0.590	0.611	0.242	1.475	4.819	59	0.850	0.691	0.237	0.616	0.309	1.011
4	0.432	0.669	0.475	0.356	0.883	2.883	60	0.851	0.691	0.237	0.617	0.309	1.009
5	0.563	0.719	0.369	0.461	0.579	1.893	61	0.852	0.691	0.237	0.617	0.309	1.009
6	0.630	0.737	0.321	0.514	0.471	1.540	62	0.852	0.691	0.237	0.617	0.309	1.009
7	0.672	0.744	0.294	0.545	0.416	1.360	63	0.853	0.690	0.237	0.617	0.309	1.009
8	0.703	0.747	0.276	0.568	0.380	1.242	64	0.854	0.690	0.237	0.617	0.308	1.007
9	0.724	0.748	0.264	0.582	0.359	1.172	65	0.855	0.690	0.236	0.618	0.308	1.005
10	0.743	0.748	0.255	0.594	0.342	1.116	66	0.855	0.690	0.236	0.618	0.308	1.005
11	0.755	0.747	0.249	0.601	0.332	1.086	67	0.856	0.689	0.237	0.617	0.308	1.007
12	0.766	0.744	0.245	0.606	0.325	1.061	68	0.856	0.689	0.237	0.617	0.308	1.007
13	0.774	0.743	0.242	0.611	0.319	1.041	69	0.856	0.689	0.237	0.617	0.308	1.007
14	0.781	0.739	0.241	0.612	0.317	1.036	70	0.856	0.689	0.237	0.617	0.308	1.007
15	0.787	0.737	0.239	0.614	0.314	1.026	71	0.857	0.688	0.237	0.617	0.308	1.006
16	0.793	0.735	0.237	0.617	0.310	1.014	72	0.857	0.688	0.236	0.618	0.308	1.005
17	0.798	0.733	0.236	0.618	0.308	1.007	73	0.857	0.688	0.237	0.617	0.308	1.006
18	0.802	0.729	0.236	0.618	0.309	1.008	74	0.857	0.688	0.237	0.617	0.309	1.008
19	0.806	0.727	0.235	0.619	0.308	1.004	75	0.858	0.687	0.237	0.617	0.309	1.008
20	0.810	0.725	0.235	0.620	0.306	1.001	76	0.858	0.687	0.237	0.617	0.308	1.007
21	0.812	0.724	0.235	0.620	0.306	1.000	77	0.858	0.687	0.237	0.617	0.309	1.008
22	0.814	0.722	0.235	0.619	0.307	1.002	78	0.859	0.687	0.237	0.617	0.309	1.009
23	0.816	0.720	0.235	0.619	0.307	1.003	79	0.859	0.686	0.237	0.616	0.309	1.010
24	0.818	0.718	0.236	0.619	0.308	1.005	80	0.859	0.686	0.237	0.616	0.309	1.010
25	0.819	0.716	0.236	0.618	0.308	1.006	81	0.859	0.685	0.238	0.616	0.310	1.011
26	0.821	0.714	0.236	0.618	0.308	1.006	82	0.860	0.685	0.238	0.616	0.310	1.011
27	0.823	0.713	0.236	0.619	0.307	1.004	83	0.860	0.685	0.238	0.616	0.310	1.012
28	0.824	0.712	0.236	0.618	0.308	1.006	84	0.860	0.684	0.238	0.615	0.310	1.014
29	0.825	0.710	0.237	0.617	0.309	1.009	85	0.860	0.683	0.238	0.615	0.311	1.014
30	0.827	0.709	0.237	0.617	0.309	1.011	86	0.861	0.683	0.238	0.615	0.311	1.015
31	0.828	0.707	0.237	0.617	0.310	1.012	87	0.861	0.683	0.238	0.615	0.311	1.016
32	0.829	0.706	0.237	0.617	0.310	1.012	88	0.861	0.682	0.239	0.615	0.311	1.017
33	0.830	0.705	0.238	0.616	0.311	1.014	89	0.861	0.682	0.239	0.615	0.311	1.017
34	0.831	0.704	0.238	0.616	0.311	1.016	90	0.862	0.682	0.239	0.614	0.312	1.018
35	0.832	0.703	0.238	0.616	0.311	1.016	91	0.862	0.681	0.239	0.614	0.312	1.019
36	0.834	0.703	0.237	0.616	0.310	1.013	92	0.862	0.681	0.239	0.614	0.312	1.020
37	0.835	0.702	0.237	0.617	0.310	1.012	93	0.862	0.681	0.239	0.614	0.312	1.019
38	0.835	0.702	0.237	0.616	0.310	1.013	94	0.863	0.681	0.239	0.614	0.312	1.019
39	0.836	0.701	0.237	0.616	0.310	1.013	95	0.863	0.680	0.239	0.614	0.312	1.020
40	0.837	0.701	0.237	0.617	0.310	1.011	96	0.863	0.680	0.239	0.614	0.312	1.020
41	0.839	0.700	0.237	0.617	0.309	1.009	97	0.864	0.680	0.239	0.614	0.312	1.019
42	0.840	0.700	0.236	0.618	0.308	1.007	98	0.864	0.680	0.239	0.614	0.312	1.020
43	0.841	0.699	0.236	0.618	0.308	1.007	99	0.864	0.679	0.239	0.614	0.312	1.020
44	0.842	0.699	0.236	0.618	0.308	1.006	100	0.864	0.679	0.240	0.613	0.313	1.022
45	0.842	0.698	0.236	0.618	0.308	1.007	101	0.864	0.678	0.240	0.613	0.313	1.023
46	0.843	0.698	0.237	0.617	0.308	1.008	102	0.865	0.678	0.240	0.613	0.313	1.023
47	0.844	0.697	0.237	0.617	0.309	1.008	103	0.865	0.678	0.240	0.613	0.313	1.024
48	0.845	0.697	0.237	0.617	0.308	1.008	104	0.865	0.678	0.240	0.613	0.313	1.023
49	0.845	0.696	0.237	0.617	0.309	1.010	105	0.865	0.678	0.240	0.613	0.314	1.024
50	0.846	0.695	0.237	0.617	0.310	1.011	106	0.865	0.677	0.240	0.613	0.314	1.024
51	0.846	0.694	0.237	0.616	0.310	1.012	107	0.866	0.677	0.240	0.613	0.314	1.024
52	0.847	0.694	0.237	0.616	0.310	1.011	108	0.866	0.677	0.240	0.613	0.314	1.025
53	0.847	0.693	0.238	0.616	0.310	1.013	109	0.866	0.677	0.240	0.612	0.314	1.026
54	0.848	0.693	0.237	0.616	0.310	1.011	110	0.866	0.676	0.240	0.612	0.314	1.026
55	0.849	0.693	0.237	0.616	0.310	1.011	111	0.866	0.676	0.241	0.612	0.314	1.027
56	0.849	0.692	0.238	0.616	0.310	1.012	112	0.866	0.676	0.241	0.612	0.314	1.027

Appendix I: Johnie Boy FOM

Yield	MOEx	MOEy	NAD	FMS	FOM	REL FOM	Yield	MOEx	MOEy	NAD	FMS	FOM	REL FOM
0.1	0.000	NaN	1.000	0.000	NaN		5.1	0.780	0.636	0.299	0.539	0.425	1.017
0.2	0.000	NaN	1.000	0.000	NaN		5.2	0.781	0.634	0.300	0.539	0.426	1.019
0.3	0.238	0.824	0.630	0.227	1.422	3.399	5.3	0.783	0.633	0.300	0.538	0.427	1.020
0.4	0.325	0.812	0.536	0.302	1.044	2.497	5.4	0.783	0.632	0.301	0.538	0.427	1.022
0.5	0.391	0.791	0.477	0.355	0.857	2.048	5.5	0.784	0.630	0.301	0.537	0.428	1.024
0.6	0.452	0.767	0.432	0.397	0.733	1.753	5.6	0.786	0.629	0.301	0.537	0.428	1.024
0.7	0.521	0.731	0.392	0.437	0.635	1.517	5.7	0.787	0.628	0.302	0.536	0.429	1.027
0.8	0.561	0.719	0.370	0.460	0.582	1.391	5.8	0.788	0.627	0.302	0.537	0.429	1.025
0.9	0.584	0.710	0.359	0.472	0.557	1.332	5.9	0.789	0.626	0.302	0.536	0.430	1.028
1	0.607	0.707	0.347	0.485	0.530	1.267	6	0.791	0.625	0.302	0.537	0.429	1.025
1.1	0.622	0.703	0.340	0.492	0.515	1.231	6.1	0.792	0.624	0.302	0.536	0.430	1.028
1.2	0.637	0.701	0.333	0.501	0.498	1.190	6.2	0.793	0.623	0.302	0.536	0.430	1.027
1.3	0.648	0.697	0.328	0.506	0.488	1.167	6.3	0.794	0.622	0.302	0.536	0.430	1.029
1.4	0.658	0.696	0.323	0.511	0.478	1.143	6.4	0.795	0.622	0.302	0.536	0.430	1.029
1.5	0.668	0.694	0.319	0.516	0.469	1.122	6.5	0.795	0.620	0.303	0.535	0.432	1.033
1.6	0.676	0.691	0.317	0.519	0.463	1.107	6.6	0.796	0.620	0.303	0.535	0.432	1.032
1.7	0.683	0.691	0.313	0.523	0.456	1.090	6.7	0.796	0.619	0.304	0.534	0.432	1.034
1.8	0.689	0.689	0.311	0.525	0.452	1.080	6.8	0.797	0.618	0.303	0.534	0.432	1.033
1.9	0.695	0.688	0.308	0.529	0.446	1.066	6.9	0.798	0.618	0.304	0.534	0.433	1.034
2	0.700	0.686	0.307	0.530	0.443	1.059	7	0.799	0.617	0.303	0.534	0.432	1.033
2.1	0.707	0.685	0.304	0.534	0.437	1.045	7.1	0.800	0.617	0.303	0.535	0.431	1.031
2.2	0.711	0.684	0.303	0.535	0.435	1.039	7.2	0.801	0.617	0.303	0.535	0.431	1.030
2.3	0.715	0.682	0.302	0.536	0.433	1.034	7.3	0.802	0.616	0.303	0.535	0.431	1.030
2.4	0.719	0.680	0.301	0.538	0.430	1.027	7.4	0.803	0.616	0.303	0.535	0.430	1.028
2.5	0.723	0.679	0.300	0.539	0.428	1.022	7.5	0.803	0.615	0.303	0.535	0.431	1.030
2.6	0.728	0.677	0.299	0.540	0.426	1.017	7.6	0.805	0.616	0.302	0.536	0.430	1.027
2.7	0.731	0.675	0.298	0.541	0.424	1.015	7.7	0.805	0.615	0.303	0.535	0.431	1.030
2.8	0.733	0.674	0.298	0.541	0.423	1.012	7.8	0.805	0.613	0.304	0.534	0.433	1.035
2.9	0.737	0.672	0.297	0.542	0.422	1.008	7.9	0.805	0.613	0.304	0.534	0.433	1.034
3	0.741	0.671	0.296	0.543	0.419	1.003	8	0.807	0.613	0.304	0.534	0.432	1.033
3.1	0.743	0.669	0.296	0.544	0.419	1.003	8.1	0.807	0.612	0.304	0.534	0.432	1.033
3.2	0.745	0.667	0.296	0.543	0.421	1.006	8.2	0.808	0.612	0.303	0.534	0.431	1.031
3.3	0.747	0.665	0.297	0.542	0.421	1.007	8.3	0.809	0.611	0.304	0.534	0.432	1.032
3.4	0.751	0.663	0.296	0.544	0.419	1.001	8.4	0.810	0.611	0.303	0.535	0.431	1.030
3.5	0.753	0.662	0.295	0.544	0.418	1.000	8.5	0.810	0.611	0.303	0.535	0.431	1.030
3.6	0.754	0.660	0.296	0.543	0.420	1.004	8.6	0.812	0.611	0.303	0.535	0.429	1.027
3.7	0.757	0.658	0.296	0.543	0.420	1.003	8.7	0.812	0.611	0.303	0.535	0.430	1.028
3.8	0.758	0.655	0.297	0.542	0.421	1.007	8.8	0.812	0.611	0.303	0.535	0.430	1.027
3.9	0.762	0.654	0.296	0.543	0.419	1.002	8.9	0.813	0.611	0.302	0.536	0.429	1.026
4	0.763	0.652	0.297	0.542	0.421	1.006	9	0.813	0.610	0.303	0.535	0.430	1.027
4.1	0.765	0.651	0.297	0.542	0.420	1.005	9.1	0.814	0.610	0.303	0.535	0.430	1.028
4.2	0.765	0.648	0.298	0.541	0.423	1.012	9.2	0.814	0.609	0.303	0.535	0.431	1.029
4.3	0.768	0.647	0.298	0.541	0.422	1.009	9.3	0.814	0.609	0.303	0.535	0.431	1.030
4.4	0.770	0.646	0.297	0.541	0.422	1.008	9.4	0.814	0.608	0.303	0.534	0.431	1.030
4.5	0.773	0.645	0.297	0.542	0.421	1.006	9.5	0.815	0.609	0.303	0.535	0.430	1.029
4.6	0.773	0.643	0.298	0.541	0.423	1.011	9.6	0.816	0.608	0.303	0.535	0.430	1.027
4.7	0.774	0.641	0.299	0.540	0.424	1.013	9.7	0.817	0.608	0.303	0.535	0.429	1.027
4.8	0.775	0.639	0.299	0.539	0.425	1.016	9.8	0.817	0.608	0.303	0.535	0.430	1.027
4.9	0.777	0.638	0.299	0.539	0.425	1.016	9.9	0.818	0.608	0.303	0.535	0.429	1.026
5	0.779	0.636	0.300	0.539	0.426	1.018	10	0.819	0.608	0.302	0.536	0.428	1.023

Appendix J: HPAC Parameters

All HPAC scenarios were run using HPAC 4.04.11. Incompatibilities with the weather files precluded the use of HPAC 5 SP1 for deposition calculations. HPAC 4.04.11 was used to create HPAC dose rate contours. Default parameters were used for HPAC except the temporal domain was adjusted to 48 hours from the detonation time, the horizontal spatial domain was limited to the weather grid, and the vertical domain was limited to the cloud top height.

The HPAC 4.04.11 projects were exported to HPAC 5 SP1 and H+1hr dose rate contours were recreated from HPAC 48-hr dose rates. H+1hr dose rates were exported from HPAC at 1km grid spacing around ground zero for the entire weather grid. To create H+1 dose rate contours, HPAC was run until deposition was complete for the temporal and/or spatial domain. In all cases, the radioactive cloud exited the spatial domain prior to 48 hours. HPAC 4.04.11 was used to create 48-hr dose rate contours. The Way-Wigner decay law relationship was used to convert 48-hr dose rate contours to H+1hr dose rate contours using (36), where $\dot{D}(x, y, 1)$ is the H+1hr dose rate, $\dot{D}(x, y, 48)$ is the H+48hr dose rate, and t is 48-hours.

$$\dot{D}(x, y, 1) = \dot{D}(x, y, t) * t^{1.2} \quad (36)$$

Using a conversion factor of $0.877 \frac{rad}{roentgen}$ Equation (36) may be rewritten as (37).

$$\dot{D}(x, y, 1) = 153.325 \dot{D}(x, y, 48) \quad (37)$$

Appendix K: Statistical Analysis

A statistical analysis of the predicted best-fit and Error in FOM yield estimates were conducted for the five surface and surface contact bursts. In all cases, data is calculated using relative predicted values. The DNA-EX recorded yield values are taken as the accepted value. The relative yield is defined by (38).

$$x = \frac{Y_{predicted}}{Y_{DASA-EX}} \quad (38)$$

For this analysis, since a lower-end bracket for yield is estimated, a more conservative approach to defining the relative yield is defined by (39).

$$x = \frac{Y_{DASA-EX}}{Y_{PREDICTED}} \quad (39)$$

The estimated standard deviation, s , for a set of data points is calculated using (40), where x_i is the relative yield of the i th data point, \bar{x} is the estimated mean relative yield, and N is the number of data points [30:75].

$$s = \sqrt{\frac{\sum (x_i - \bar{x})^2}{N - 1}} \quad (40)$$

For this analysis, \bar{x} and N are one and five, respectively.

The confidence limit, CL , for a data set is calculated using (41), where t is a statistical factor depending on the number of degrees of freedom [30:90].

$$CL = \bar{x} \pm \frac{ts}{\sqrt{N}} \quad (41)$$

For this analysis, a t -value of 2.132 was used for 90% confidence [30:90].

Appendix L: Glossary

4-D Winds—Winds derived from Jones’ high resolution mesoscale reanalysis weather data. The wind components in the x and y directions at eleven different elevation levels are retrieved for each point in the weather reanalysis grid at 1-hour increments for more than 60 hours. Vertical winds from the reanalysis weather data are not considered but the horizontal wind components vary as the wafers settle. The wind data undergoes temporal changes.

Area of Interest (AOI)—Area around ground zero for which recreated dose rate contours are compared with the historic dose rate contours. The AOI for all cases, except for Johnie Boy, was set to a 200 x 200 mile grid centered over ground zero. For Johnie Boy, the grid was limited to 230km x 230km because the DNA-EX dose rate contour was cut off at 115km north of ground zero.

Balloon Winds—Winds taken from balloon soundings at or near atomic test sites.

Capped Cloud Tops—Case in which the distribution of activity for each particle size group is restricted to below the DNA-EX observed cloud top height. The cumulative distribution for each particle size group below the observed cloud top height is normalized to a value of “1”. The activity for each particle size group is distributed to this normalized distribution.

Error in Figure of Merit (Error in FOM)—Quantification (relative difference) of the difference in FOM for a yield to the FOM for the best fit yield.

Figure of Merit (FOM)—Figure of Merit created to quantitatively describe the relationship of Warner and Platt’s MOE_x , MOE_y , and NAD. The possible range for

FOM values includes all non-negative numbers. An FOM value of zero represents perfect agreement between reference and reproduced dose rate contours.

Hotline Length—Distance from ground zero to the end of the dose rate contour. It is calculated traveling along the center of a dose rate contour to its end.

Inversion—Mathematical analysis of the dose rate contours associated with a range of yields using the FOM.

Uncapped Cloud Tops—The distribution of particles for each equal activity particle size group is not restricted to below the observed cloud top height.

Bibliography

1. **US Government.** *National Strategy for Combating Terrorism.* Washington, D.C. : United States Government, 2006.
2. **Defense Threat Reduction Agency.** About DTRA: Mission. *DTRALink.* [Online] 2008. [Cited: August 18, 2008.] <http://www.dtra.mil/about/mission.cfm>.
3. **Former, Charles.** *Memorandum For Distribution (Hazard Prediction Assessment Capability Users).* Fort Belvoir : Defense Threat Reduction Agency, 2008.
4. **Jones, Christopher P.** *High Resolution Mesoscale Weather Data Improvement to Spatial Effects for Dose-Rate Contour Plot Predictions.* Wright-Patterson AFB : Air Force Institute of Technology, March 2007.
5. **Jodoin, V. J.** *Nuclear Cloud Rise And Growth.* Wright-Patterson AFB : Air Force Institute of Technology, June 1994.
6. **Norment, Hillyer G.** *Validation and Refinement of the DELFIC Cloud Rise Module.* Washington D.C. : Defense Nuclear Agency, 1977.
7. —. *DELFIIC: Department of Defense Fallout Prediction System Volume I - Fundamentals.* Washington D.C. : Defense Nuclear Agency, 1979.
8. **Medalia, Jonathan.** *Congressional Research Service Report for Congress: Terrorist Nuclear Attacks on Seaports: Threat and Response.* Washington, D.C. : The Library of Congress, 2002.
9. **Nevada Operations Office.** *United States Nuclear Tests: July 1945 through September 1992.* Springfield, VA : U.S. Department of Energy, December 2000.
10. **Chancellor, Richard W.** *A Comparison of Hazard Prediction and Assessment Capability (HPAC) Software Dose-Rate Contour Plots to a sample of Local Fallout Data from Test Detonations in the Continental United States, 1945-1962.* Wright Patterson AFB : Air Force Institute of Technology, March 2005.
11. **Pace, Kevin D.** *Terrain and Spatial Effects on a Hazard Prediction and Assessment Capability (HPAC) Software Dose-rate Contour Plot Predictions as Compared to a Sample of Local Fallout Data from Test Detonations in the Continental United States, 1945-1962.* Wright-Patterson AFB : Air Force Institute of Technology., March 2006.

12. **Jones, Christopher P.** *High Resolution Mesoscale Weather Data Improvement To Spatial Effects For Dose-Rate Contour Plot Predictions.* Wright-Patterson AFB : Air Force Institute of Technology, March 2007.
13. **Bridgman, Charles J.** *Introduction to the Physics of Nuclear Weapons Effects.* Fort Belvoir : Defense Threat Reduction Agency, 2001.
14. **Dolan, Philip J. and Glasstone, Samual.** *The Effects of Nuclear Weapons.* Alexandria, Va : The United States Department of Defense and the United States Department of Energy, 1977.
15. **Hopkins, A. T.** *Development And Validation Of A New Fallout Transport Method Using Variable Spectral Winds.* Wright-Patterson AFB : Air Force Institute of Technology, September 1984.
16. **Connors, Stephen P.** *Aircrew Dose and Engine Dust Ingestion From Nuclear Cloud Penetration.* Wright-Patterson AFB : Air Force Institute of Technology, September 1985.
17. **Pugh, George E. and Galiano, Robert J.** *An Analytical Model of Close-In Deposition of Fallout for Use in Operational Type Studies.* Washington, D.C. : The Pentagon, Weapon System Evaluation, October 1959.
18. **Baker III, George H.** *Implications of Atmospheric Test Fallout Data For Nuclear Winter.* Wright-Patterson AFB : Air Force Institute of Technology, February 1987.
19. **Davis, N. C.** *Particle Size Determination from Local Fallout.* Wright Patterson AFB : Air Force Institute of Technology, December 1986.
20. **Izrael, YU. A.** *Radioactive Fallout After Nuclear Explosions and Accidents.* Amsterdam : Elsevier, 2002.
21. *Definitive Equations for the Fluid Resistance of Spheres.* **Davies, C.N.** London : The Proceedings of the Physical Society, July 1945, Vol. 57.
22. *An Aid to Computation of Terminal Fall Velocities of Spheres.* **McDonald, James E.** s.l. : Journal of Meteorology, August 1960, Vol. 17.
23. **Hopkins, A. T.** *A Two Step Method To Treat Variable Winds In Fallout Smearing Codes.* Wright-Patterson AFB : Air Force Institute of Technology, 1982.
24. *The Rate of Decay of Fission Products.* **Way, Kathrine and P., Wigner E.** 375, s.l. : Physical Review, 1948, Vol. 76.
25. **DNA 1251-1-EX.** *Compilation of Local Fallout Data from Test Detonations 1945-1962 Extracted From DASA 1251.* Washington D.C. : Defense Nuclear Agency, 1979.

26. *Reexamination of the 9-10 November 1975 "Edmund Fitzgerald" Storm Using Today's Technology.* **Hultquist, Thomas R., Dutter, Michael R. and Schwab, David J.** s.l. : American Meteorological Society, May 2006.

27. *User-Oriented Two-Dimensional Measure of Effectiveness for the Evaluation of Transport and Dispersion Models.* **Warner, Steve and others.** s.l. : Journal of Applied Meteorology, January 2004, Vols. 43:58-73.

28. **Garcia, Fred E.** *Aircrew Ionizing Doses From Nuclear Weapon Bursts.* Wright-Patterson AFB : Air Force Institute of Technology, March 2001.

29. **Abramowitz, M. and I., Stegun.** *Handbook of Mathematical Functions with Formulas, Graphs, and Mathematical Tables.* Washington, D.C. : U.S. Government Printing Office, March 1964.

30. **Christian, Gary D.** *Analytical Chemistry.* s.l. : John Wiley & Sons, Inc., March 2003.

REPORT DOCUMENTATION PAGE

Form Approved
OMB No. 074-0188

The public reporting burden for this collection of information is estimated to average 1 hour per response, including the time for reviewing instructions, searching existing data sources, gathering and maintaining the data needed, and completing and reviewing the collection of information. Send comments regarding this burden estimate or any other aspect of the collection of information, including suggestions for reducing this burden to Department of Defense, Washington Headquarters Services, Directorate for Information Operations and Reports (0704-0188), 1215 Jefferson Davis Highway, Suite 1204, Arlington, VA 22202-4302. Respondents should be aware that notwithstanding any other provision of law, no person shall be subject to a penalty for failing to comply with a collection of information if it does not display a currently valid OMB control number.

PLEASE DO NOT RETURN YOUR FORM TO THE ABOVE ADDRESS.

1. REPORT DATE (DD-MM-YYYY) 27-03-2009		2. REPORT TYPE Master's Thesis		3. DATES COVERED (From – To) Oct 2008—Mar 2009	
4. TITLE AND SUBTITLE Estimation of Weapon Yield From Inversion of Dose Rate Contours				5a. CONTRACT NUMBER	
				5b. GRANT NUMBER	
				5c. PROGRAM ELEMENT NUMBER	
6. AUTHOR(S) O'Day, Buckley E., MAJOR, USA				5d. PROJECT NUMBER	
				5e. TASK NUMBER	
				5f. WORK UNIT NUMBER	
7. PERFORMING ORGANIZATION NAMES(S) AND ADDRESS(S) Air Force Institute of Technology Graduate School of Engineering and Management (AFIT/EN) 2950 Hobson Way WPAFB OH 45433-7765				8. PERFORMING ORGANIZATION REPORT NUMBER AFIT/GNE/ENP/09-M05	
9. SPONSORING/MONITORING AGENCY NAME(S) AND ADDRESS(ES) DTRA/NTD Dr. Ed Turano 8725 John J. Klingman Rd. Stop 6201 Ft. Belvoir, VA 22060				10. SPONSOR/MONITOR'S ACRONYM(S)	
				11. SPONSOR/MONITOR'S REPORT NUMBER(S)	
12. DISTRIBUTION/AVAILABILITY STATEMENT APPROVED FOR PUBLIC RELEASE; DISTRIBUTION UNLIMITED					
13. SUPPLEMENTARY NOTES					
14. ABSTRACT This research studies the uncertainty in yield estimation from inversion of dose rate contours. The Hazard Prediction and Assessment Capability (HPAC) and a simple FORTTRAN95 based Fallout Deposition Code (FDC) are used to recreate dose rate contours from historic nuclear tests. Fallout footprints from six atomic tests are recreated using balloon wind soundings and high resolution mesoscale weather reanalysis data. Dose rate contour plots are created for different yields for a single set of weather conditions. Dose rate contours are compared to determine uncertainty in yield estimation from inversion of dose rate contour plots. Results of these dose rate recreations are compared to historical patterns found in the Defense Nuclear Agency's (DNA) DNA 1251-1-EX Compilation of Local Fallout Data From Test Detonations 1945-1962 Extracted from DASA 1251. Recreated dose rate contours are compared against historic patterns using a Figure of Merit (FOM) developed from the Measure of Effectiveness (MOE) and the Normalized Absolute Difference (NAD) techniques. This research provides a method to estimate the minimum yield required to create a dose rate contour to within a factor of two. This research determined that use of ground zero balloon soundings and reanalysis winds thereafter allowed the most accurate recreation of historic dose rate contours.					
15. SUBJECT TERMS Dose-Rate Contours, Fallout, Radioactive Fallout, Measure of Effectiveness, Normalized Absolute Difference, Areal Comparison, Modeling Atomic Tests, Modeling Nuclear Tests, Modeling Fallout					
16. SECURITY CLASSIFICATION OF:		17. LIMITATION OF ABSTRACT UU	18. NUMBER OF PAGES 138	19a. NAME OF RESPONSIBLE PERSON Lt Col Steven T. Fiorino, AFIT/ENP	
REPORT U	ABSTRACT U			19b. TELEPHONE NUMBER (Include area code) (937) 255-3636, ext 4506	

Standard Form 298 (Rev: 8-98)

Prescribed by ANSI Std. Z39-18